Alma Mater Studiorum - Università degli Studi di Bologna

DOTTORATO DI RICERCA IN GEOFISICA

Ciclo XXIII

GEO/10

Modeling the European crust for seismic wave propagation

Presentata da: Irene Molinari

Coordinatore dottorato:
Prof. Michele Dragoni

Relatore:
Dr. Andrea Morelli

Esame finale anno 2011

Acknowledgments

I would like to thank my advisor Andrea Morelli for his guidance, patience and constant support during the last three years.

Thanks also to the Istituto Nazionale di Geofisica e Vulcanologia and the Universita di Bologna, for the financial support; special thanks to the INGV -Sezione Bologna, where I have developed my research.

Part of this work was developed at Ludwig Maximilian Universitat in Munich under the supervision of Martin Kaeser and Heiner Igel. I would like to thanks Martin and Heiner for opening to me the door of their research groups and the seismic wave simulation world.

Thanks to Peter Danecek for his patient help with SEM simulations and for his critical comments.

Thanks to Victor Raileanu for collected important informations on East Alps that were fundamental to a part of this thesis.

The last three years would never be the same without all the friends and colleagues at INGV and at LMU: Brunella, Antonio Pio, Paola, Piero, Renata, Simone, Rosaria, Christian, Dario, Roberta, Stefan, Andre, Corrado and all the others (a complete list is impossible!).

Special thanks go also to my family and to Alessandro for their unconditional support and love.

Contents

Introduction

Looking into the structure, composition and behaviour of the Earth is one of the main goals of the seismic studies. From recorded signals seismologists try to find robust clues about the constitution of the Earth, using inverse theory to adjust numerical representations of seismic properties to provide the best possible fit to seismograms.

Many geophysical problems — such as surface wave, group velocity (e.g. Schivardi and Morelli, 2011) and full waveform tomography(e.g. Fichtner et al., 2009), determination of mantle flows (Faccenna and Becker, 2010), gravity studies, source inversion (Pondrelli et al., 2002) — need plausible models as starting point for such studies. Crustal structure varies greatly over small scale length and has a strong effects on seismic waves. Focusing our attention to seismic wave propagation at the continental scale, we become aware of the fact that surface waves are very sensitive to the crust but in the frequency range and in the geometry ray used in most of the tomography studies (at continental scale) they are not able to discriminate between the crust and the uppermost part of the mantle. A priori models of the crust are thus often used to model seismic wave propagation at large distance and to account for shallow structure when imaging upper mantle structure.

Focusing on forward earthquakes simulations, plausible crustal and mantle models are the first step to obtain realistic seismograms and results. Recent development in computer facilities and numerical methods — Spectral Element Method (e.g. Komatitsch and Tromp, 2002), ADER-DG method (e.g. Dumbser and Kaeser, 2006), Finite Difference method (e.g. Igel and Weber, 1996) — enable to solve the wave equation in 3D complex media with high accuracy. These methods require a discrete representation of the investigation domain (mesh) through which we propagate wave.

To model seismic wave propagation at the scale of a continent — i.e. signals travelling to stations a few hundred or thousand kilometers from the earthquake source — we have therefore to face two orders of problems connected to the characters of the Earth's crust. One is connected to the detail and reliability of current models, that are sufficiently accurate when we look at long periods and large distances, at the global scale, but often miss significant features at the scale of sedimentary basins and mountain ranges, that become very important as we zoom closer. A lot of reliable and detailed information on these structures exist, for instance deriving from active-source studies, but are often not integrated in wide-area compilations such as desirable.

At the European scale, it becomes clear that current crustal models are not adequate for modeling regional datasets with enough detail. The global model CRUST2.0 (Bassin et al., 2000) is frequently used for crustal correction and wave propagation, but its resolution is too low for continental-scale studies. Many other detailed information are available, but at different scales, with different information

contents, and following different formats: this information needs to be merged into a larger-scale, coherent representation.

The other important issue is that connected to the faithful implementation of a known structure in computational meshes used in forward simulations of wave propagation. The shallow crustal discontinuities indeed are difficult to represent, because of the small size of the shallower elements of the mesh that lead to a very short time step. Capdeville and Marigo (2008) points out the importance of the representation of crustal structure: a completely neglectfulness of the crust in the mesh, or designing a too coarse mesh, will lead to a lack in the solution accuracy.

In this study, I am mostly interested in addressing these two fundamental issues, i.e. how to retrieve a 'good' crustal model for Europe, on the basis of existing knowledge, and how to best represent it for efficient, but accurate, numerical simulation of seismic wave propagation.

In the first part (Chapter 1), we analyse the surface wave sensitivity to the crustal structure presenting an exercise, based on surface wave dispersion matching, to reparameterize CRUST2.0 global model in a simpler grid that can be considered equivalent to CRUST2.0 in modeling surface waves. The models is tested from a wave propagating point of view with SPECFEM-3D code (Komatitsch and Tromp, 2002).

Since European crustal models were not enough satisfactory for our needs, we collect all the informations available on the this region and we create a new comprehensive reference crustal model for the European plate (Chapter 2) that describes the complex structure of the Europe with higher resolution and more plausibility than previous models. However, we can improve the resolution of such large scale compilation: we collect tens of seismic lines in the East Alps region (Chapter 3) building up, applying a geostatistic technique, a complete regional crustal model of that area that was included in EPcrust. This would be an example in which new local models could be developed and integrated in the continental one. The results are available on *www.bo.ingv.it/eurorem/EPcrust*.

Since new models are available, before starting a 3D implementation of the models in numerical methods, in Chapter 4 we quantitatively analyse in 2D the influence of the representation and uncertainties in the knowledge of crustal parameters on simulated wave field. We evaluate different synthetic test cases respect to the reference, analysing the frequency and source-receiver-distance dependence of our approximations. For the simulations, we use an high order ADER-DG scheme implemented in the SeisSol2D code (Dumbser and Kaeser, 2006) able to honour the discontinuities in the crust with high fidelity.

From a seismological point of view the next step after developing a model would be a validation of the model itself. In chapter 5, we go through a validation process of EPcrust. The main goal is to understand if our new model is able to give a better fit of the real data. We use the Spectral Element Method as implemented in SPECFEM3D-Globe (Komatitsch and Tromp, 2002). This choice would be a compromise between accuracy of the representation of the crustal structure and

computational cost. The ADER-DG methods, well suited for an accurate representation of the sharp interface within the crust, is at the moment computationally too expensive for 3D simulations at continental scale.

At the and of this thesis, we give a brief overview on methods and theory applied to obtain our results. In Appendix A we introduce the geostatistical methods applied in Chapter 3. In Appendix B and C ADER-DG and SEM approach are described. A short description of SeisSol and SPECFEM3D codes are provided as well. Finally, in Appendix D the description of the time-frequency misfit criteria, widely used in the misfit calculations in Chapter 4 and 5 is provide.

References

Bassin, C., Laske, G., Masters, G., 2000. The current limits of resolution for surface wave tomography in North America. Eos Trans. AGU 81, 48.

Capdeville, Y., Marigo, J., 2008. Shallow layer correction for Spectral Element like methods. Geophys. J. Int. 172(3), 1135–1150. doi:10.1111/j.1365-246X.2007.03703.x.

Dumbser, M., Kaeser, M., 2006. An arbitrary high-order discontinuous galerkin method for elastic waves on unstructured meshes II. the three-dimensional isotropic case. Geophysical Journal International 167(1), 319–336.

Faccenna, C., Becker, T.W., 2010. Shaping mobile belts by small-scale convection. Nature 465(7298), 602–605. doi:10.1038/nature09064.

Fichtner, A., Kennett, B.L.N., Igel, H., Bunge, H., 2009. Full seismic waveform tomography for upper-mantle structure in the australasian region using adjoint methods. Geophysical Journal International 179(3), 1703–1725.

Igel, H., Weber, M., 1996. P-sv wave propagation in the whole mantle using high-order finite differences:application to lowermost mantle structure. Geophys. Res. Lett. 23, 415Ð418.

Komatitsch, D., Tromp, J., 2002. Spectral-element simulations of global seismic wave propagation: I. validation. Geophysical Journal International 149(2), 390–412.

Pondrelli, S., Morelli, A., Ekstrom, G., Mazza, S., Boschi, E., Dziewonski, A.M., 2002. European-Mediterranean regional centroid-moment tensors: 1997-2000. Phys. Earth Planet. Inter. 130(1-2), 71–101. doi:10.1016/S0031-9201(01)00312-0.

Schivardi, R., Morelli, A., 2011. EPmantle: a three-dimensional transversely isotropic model of the upper mantle under the European Plate. In press Geophys. J. Int. .

Chapter 1

Representation of crustal structure and surface wave modeling

Contents

1.1 Introduction

Knowledge of crustal structure is a crucial point for high-frequency seismic surface wave propagation and as a prerequisite for the determination of the upper mantle structure in surface and teleseismic wave tomography and a good crustal correction (Bozdag and Trampert, 2008) is needed when upper mantle structure is studied (and in particular anisotropy properties). Crustal structure varies greatly over small length scales and has a first order effect on shear wave velocity and surface waves In large scale surface wave studies, it is common to model the Earth structure with flat and parallel layers. Representing the structure of the crust with a blocky parameterization in the horizontal direction and, in each block, with a vertical layered 1D structure, result efficient and appropriate in a wide range of studies (Bassin et al., 2000; Tesauro et al., 2008).
The widely used global crustal model is CRUST2.0 (Bassin et al., 2000) where the Earth crust is divided into $2^\circ \times 2^\circ$ cells horizontally and into up to 7 layers vertically: ice, water, soft sediment, hard sediment, upper, middle and lower crust. Apart from its limited lateral resolution CRUST2.0 has a complex vertical layering and discontinuous lateral steps (Figure 1.1) that make it difficult to represent the model with fidelity in numerical code and in regular grids.

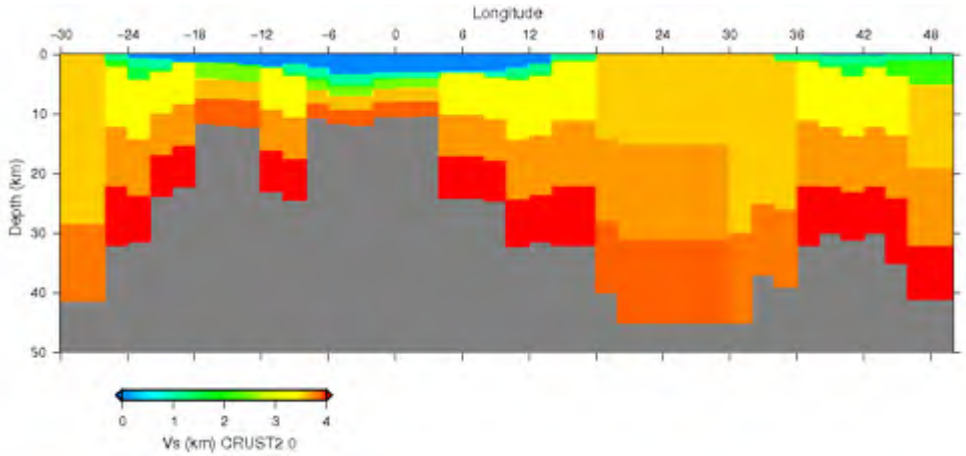

Figure 1.1: Vertical section of CRUST2.0 model. It's along the 70°N parallel and from −30°W to 50°E longitude.

It's well known that a not reliable representation of the shallowest Earth structure can lead to errors in the simulated seismograms: in particular the SEM code —based on hexahedral meshes— have difficulty to represents the shallow crustal discontinuities because of the small size of the shallower elements that lead to a very short time step. Capdeville and Marigo (2008) points out the importance of the representation of crustal structure: a completely neglectfulness of the crust in the mesh, or designing a mesh that does not honour the crust model discontinuity interfaces (especially the Moho), will lead to a lack in the solution accuracy, difficult to predict. CRUST2.0 model is currently implemented in the wave propagation code SPECFEM3D-Globe (Komatitsch and Tromp, 2002) where the discontinuities of the model are not honoured and the model implemented is a smoothed version of the original one. Possible solutions were suggested by, i.e.Capdeville and Marigo (2008) and Fichtner and Igel (2008). In the first work, by resorting to a second order matching asymptotic approximation, the thin layer are replaced by a vertically smooth effective medium without discontinuities together with a specific surface boundary condition, and in the second, the authors came up with equivalent long wavelength crustal model using a non-linear dispersion curve matching.

Here we present an exercise to riparameterize CRUST2.0 global model in a simpler grid that can be considered equivalent to CRUST2.0 in modeling surface waves in the period range from 6 s to 200 s. Our simple, 4-km layered model, within acceptable accuracy, is equivalent to CRUST2.0 and can be easily smoothed laterally. We follow, somehow, the approach of surface waves dispersion curve matching, since these phases are the most sensitive to the shallowest Earth structure. During this exercise, we also draw some considerations on the real sensitivity of the surface waves to details of parameterization of the Earth crust.

1.2 Equivalent models

Surface wave speed at short and intermediate period have a strong sensitivity to shallow Earth structure and any change in Moho depth and in the elastic parameters leads to changes in the dispersion curve. In this period range, it is well know that surface waves are strongly sensitive to any change in anisotropic medium velocity (Vp and Vs), but also in density structure in the shallowest layers.
If one have to represent a crustal model as a regular matrix some approximations will be done, as, for example, in the Moho depth or assigning elastic parameters in the new grid (Figure 1.2). In each layer you could make an average of the parameter read in the original model but this could not be a fair description of the original model. In fact, these approximations have a strong influence on the surface wave dispersion curves in particular on periods shorter then 50 seconds, and if the differences in phase velocity are comparable to the experimental errors we can not neglect this kind of errors.

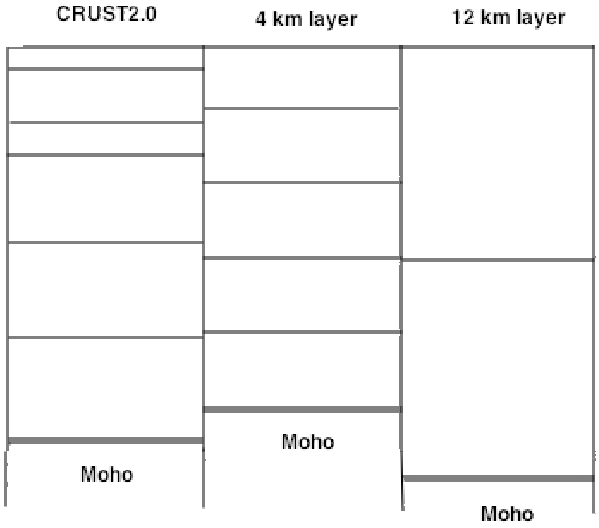

Figure 1.2: Different depth parameterizations for CRUST2.0

Taking in mind this error due to approximations of the model, in order to create a simpler layered model than CRUST2.0 but with the same surface wave dispersion, we calculated the phase dispersion for Love and Rayleigh waves in the model CRUST2.0+PREM for the whole Earth and we iteratively invert these data for a model with uniform layer thickness. We invert for isotropic Vp, Vs and ρ since the surface dispersion curve is strongly sensitive to change of this parameter in the shallow part of the model (crust). For the calculation of the dispersion curves we used the algorithm explained by Takeuchi and Saito (1972).
In each $2^\circ \times 2^\circ$, we start from an a-priori model that has the same layer thickness of the final model and an average of the seismic elastic parameters. We note that

such an approximation is not enough to get the same dispersion curve for period less than 40 seconds. This is the mainly reason that lead us to perform a non linear inversion.
In this way, we derive simple layered models, that generate the same Love and Rayleigh phase speed as CRUST2.0. Our final model is composed by layers with uniform thickness, and, as two instances, we create two different equivalent models: the first with a layer thickness of 4 km (*CR-4KM*) and second one with 12 km layer thickness (*CR-12KM*). It's important to point out that this different parameterization of the CRUST2.0, not add information to the model: the resolution and information content will not be improve.
In this work, we change the original Moho depth assigning it the nearest value multiple of choosen layer thickness: for example, if CRUST2.0 has a Moho depth of 33.5 km we approximated it to 32 km in the *CR-4KM* model. An other important problem is related to the water layer thickness that have a strong influence on Rayleigh wave dispersion curves. In order to prevent further errors in our representation, we keep the water layer fixed as in CRUST2.0. This choice do not have a remarkable impact when, for example, we want to use our equivalent models for wave propagation: in codes, such as SPECFEM3D-Globe, oceans are represented as an external force and not as explicit layer in the computational mesh of the Earth.
Our technique can be easily applied to create equivalent model with different layer thickness and it is also possible to keep the Moho depth fixed and get out a desired layered model.
More details about parameterization and the inversion method are described in the next section.

1.3 Parameterization and inversion method

The crust is often considered an isotropic structure. Looking at short periods surface waves it's clear that these waves are strongly influenced by all the elastic parameters and the density structure in the shallower part of the model (Aki and Richard, 2002). To determine elastic parameters from surface waves is a non unique problem, and changes in crustal parameters in a single layer may not be resolved. In this case, we can overcome this problem: we are looking for an equivalent model not the true model. We are able to calculate a measure a sensitivity for some measurable parameters such as the phase and group velocity of surface waves. Figure 1.3 and 1.4 show the 1D sensitivity kernels for the phase velocity for Rayleigh and Loves wave with respect to the elastic parameters, calculated in a model with an oceanic crustal structure on top taken by CRUST2.0 (the mantel structure is PREM (Dziewonski and Anderson, 1981)). We decide to take all these parameters into account during the ri-parameterization exercise ,and let they able to change during the inversion procedure.

The physic relation between the phase velocity and the model parameters is

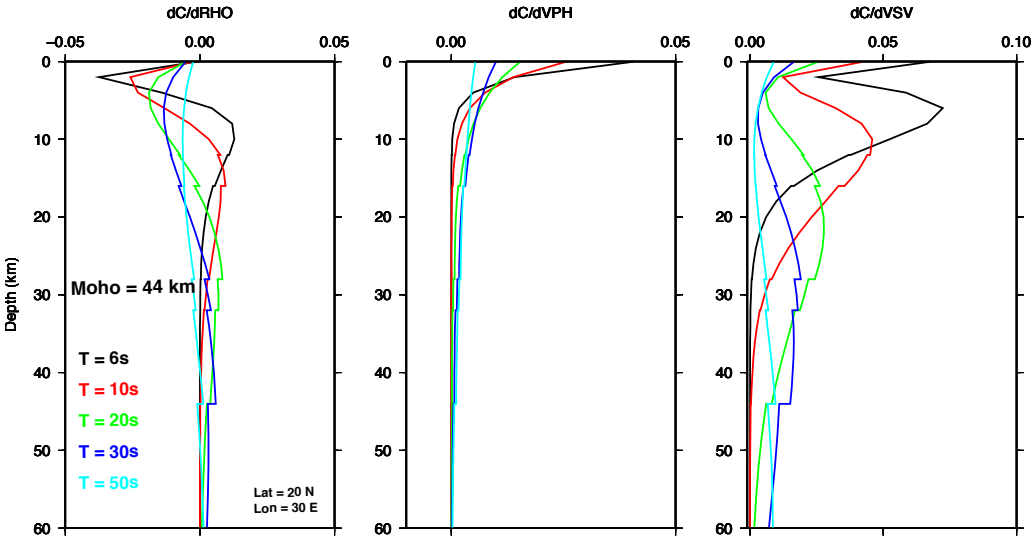

Figure 1.3: Rayeigh wave isotropic sensitivity kernel for a crustal structure of 44 km thickness.

not linear and the relation, that link the model vector $\mathbf{m}$ to the data vector $\mathbf{d}$, $\mathbf{d} = \mathbf{g}(\mathbf{m})$, should be inverted using an iterative scheme since the non-linearity in not too strong. We proceed to fond the minimum of a coast function, built considering both data misfit and distance from an a priori model $\mathbf{m}_0$, by an iterative Newton type minimization, that in our case taken from Tarantola (2005).

$$\mathbf{m}_{n+1} = \mathbf{m}_0 - (\mathbf{G}_n^T \mathbf{C}_D^{-1} \mathbf{G}_n + \mathbf{C}_M^{-1})^{-1} \mathbf{G}_n^T \mathbf{C}_D^{-1} ((\mathbf{A}(\mathbf{m}_n) - \mathbf{d}^{oss}) - \mathbf{G}_n(\mathbf{m}_n - \mathbf{m}_0)) \tag{1.1}$$

$$\mathbf{m}_{n+1} = \mathbf{m}_0 - \mathbf{C}_M \mathbf{G}_n^T (\mathbf{G}_n \mathbf{C}_M \mathbf{G}_n^T + \mathbf{C}_D)^{-1} ((\mathbf{A}(\mathbf{m}_n) - \mathbf{d}^{oss}) - \mathbf{G}_n(\mathbf{m}_n - \mathbf{m}_0)) \tag{1.2}$$

where $\mathbf{A}(\mathbf{m}) = c(\mathbf{m}_n) = c_n$ are the phase velocity calculated for model $\mathbf{m}_n$ and

$$\mathbf{G}_n = \left(\frac{\partial \mathbf{g}}{\partial \mathbf{m}}\right)\Big|_{m_0} = \frac{\partial c_n}{\partial \mathbf{m}_n} \tag{1.3}$$

are the phase velocity kernels respect to model parameters (examples are in Figure 1.3 and 1.4). $\mathbf{C}_M$ is the covariance matrix that give information about the information content of the a-priori model and $\mathbf{C}_D$ is the data covariance matrix.

In our application, we consider Rayleigh and Love phase velocity sampled at $(10, 12, 15, 20, 25, 30, 35, 40, 45, 50, 55, 60, 75, 100, 125, 150, 175, 200)$ seconds for the 4KM model and $(16, 18, 20, 22, 26, 30, 35, 40, 45, 50, 55, 60, 75, 100, 125, 150, 175, 200)$ seconds for the 12KM model. The elastic parameters considered in the inversion are v_P, v_S and ρ. The data vector defined as $\mathbf{d} = (C_{L1}, \ldots, C_{L18}, C_{R1}, \ldots, C_{R18})$ with dimension 32, the kernel matrix $\mathbf{G}$ has dimension $(32) \times (3N)$, with N number of layers in the crust in the considered cell, and the model vector $\mathbf{m}$ (dimension 3N)

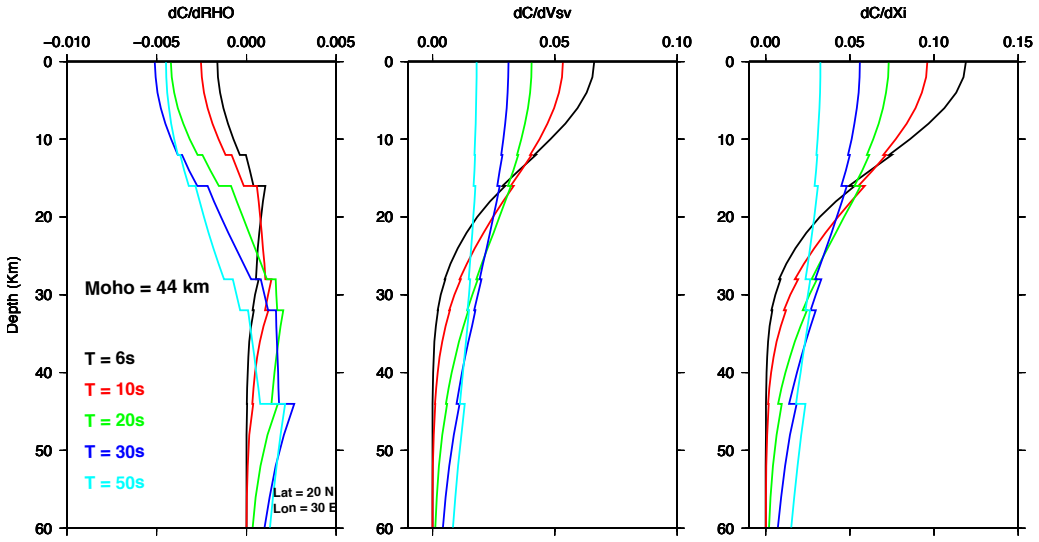

Figure 1.4: Love wave isotropic sensitivity kernel for a crustal structure of 44 km thickness.

is defined as $\mathbf{m} = (v_{S_1}, \ldots, v_{S_N}, v_{P_1}, \ldots, v_{P_N}, \rho_1, \ldots, \rho_N)$. We assumed independent Gaussian uncertainties on the data and we set them as $\sigma^2 = 0.01 km/s$. Analogous assumptions on the a-priori model covariance and the covariance matrix is diagonal (1.3).

$$\mathbf{C_M} = \begin{pmatrix} \sigma_{\rho_1} & \cdots & \cdots & \cdots & \cdots & \cdots \\ \cdots & \cdots & \cdots & \cdots & \cdots & \cdots \\ \cdots & \cdots & \sigma_{\rho_N} & \cdots & \cdots & \cdots \\ \cdots & \cdots & \cdots & \sigma_{V_{P_1}} & \cdots & \cdots \\ \cdots & \cdots & \cdots & \cdots & \cdots & \cdots \\ \cdots & \cdots & \cdots & \cdots & \cdots & \sigma_{V_{s_N}} \end{pmatrix} \tag{1.4}$$

We set $\sigma^2_\rho = 0.05 g/cm^3$, $\sigma^2_{V_P} = 0.1 km/s$ and $\sigma^2_{V_S} = 0.1 km/s$.

At each iteration (1.1) we recalculate the dispersion curves and the partial derivatives for the current model, minimizing the residual between predicted and observed data and maintaining the final model close to the a-priori model. The cycle ends when the deviation (**??**) between the current model and the model at the previous cycle is less than a fixed value (we choose 0.005). Typically our inversion cycle stops after 3 or 4 iterations.

To quantify the goodness of the data fit, during each step of the inversion we calculate the data misfit as root mean square RMS_d of the data vector at $i-1$ and i iterations (1.5):

$$RMS_d = \sqrt{\frac{\sum_{i=1}^{N} (C_i^{oss} - C_i^k)^2}{N-1}} \tag{1.5}$$

We show two examples of the inversion in two cell of the model: one for the *CR-4KM* model, in Figure 1.5, and one for the *CR-12KM* model (Figure 1.6). In the left part of the pictures, we plot the Love (top) and Rayleigh (middle) dispersion curves for CRUST2.0 (red lines), for the a priori model (black) and for the *CR-4KM* model (green dashed lines); in the bottom we report the difference between the a-priori and CRUST2.0 dispersion curves (black line) and the difference between the *CR-4KM* model and CRUST2.0 dispersion curves (green); in the right panel, we compare CRUST2.0, the a-priori model and the final *CR-4KM* layered model in the same cell. In these examples we can note that the inversion works well and the final model can be considered equivalent to the original (CRUST2.0) from surface wave dispersion point of view. Love waves are more influenced by a change in the shallower layer than Rayleigh waves. The final model and the a-priori model are quite the same, but we can see in the difference plot (left-bottom), these small differences in the models lead out a non negligible difference in the dispersion curves (about $2-4\%$).

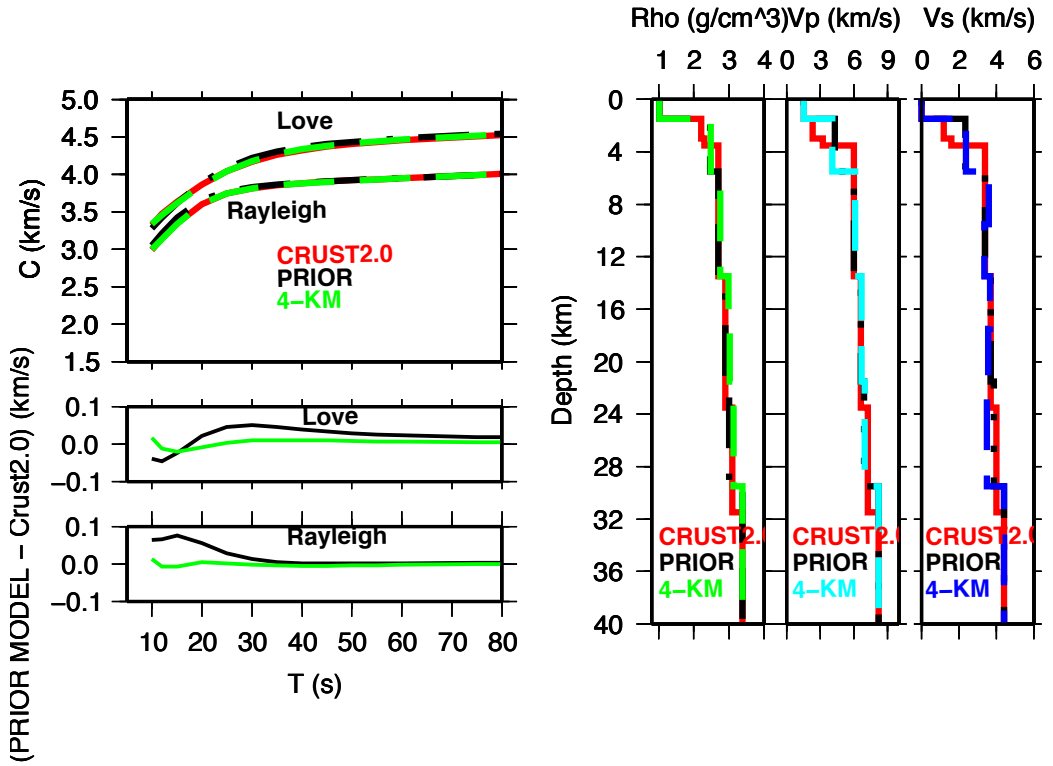

Figure 1.5: Left: Love (top) and Rayleigh (middle) dispersion curves for CRUST2.0 (red lines) and for the *CR-4KM* model (green dashed lines) and (bottom) the difference between the a-priori and CRUST2.0 dispersion curves, black line, and the difference between the *CR-4KM* model and CRUST2.0 dispersion curves (green). (Right) We compare CRUST2.0 model (red), the a priori model (black) and the final *CR-4KM* layered model (colored) in cell with Lat=70 N and Lon=12W.

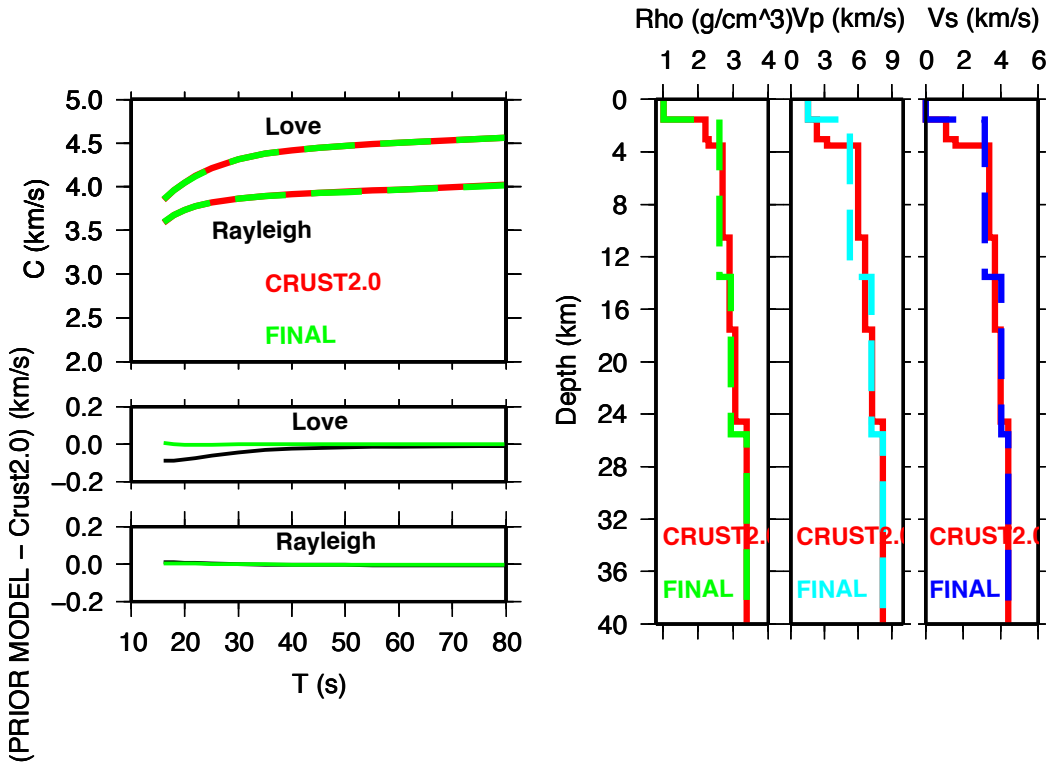

Figure 1.6: The same as in Figure 1.5 but for the *CR-12KM* model in the cell with Lat=70 N and Lon=10E.

1.3.1 Covariance and resolution matrix

Once the sensitivity kernels are calculated, a straight forward way to have a quantitative idea about the resolution of the inversion is to calculate the resolution matrix and the a-posteriori covariance matrix. Following Tarantola (2005) , the covariance matrix is defined as:

$$\mathbf{C}_M^P = \mathbf{C}_M - \mathbf{C}_M\mathbf{G}^T(\mathbf{G}\mathbf{C}_M\mathbf{G}^T + \mathbf{C}_D)^{-1}\mathbf{G}\mathbf{C}_M \tag{1.6}$$

where $\mathbf{C_M}$, $\mathbf{C_D}$ and $\mathbf{G}$ were defined in the previous section. The diagonal elements of $\mathbf{C}_M^P$ give the absolute uncertainty on each parameter of the solution, while off-diagonal terms are the product of variance and correlation of pairs of parameters. A nonzero off-diagonal elements means that the model parameters were determined as a linear combinations of the parameters themselves and a positive value means a correlation and a negative one an anti-correlation. In our case $\mathbf{C}_M$ can be read in terms of spatial correlations.

The resolution matrix (Soldati and Boschi, 2005), $\mathbf{R}$ can be thought as the operator that relates the output and the input model and knowing $\mathbf{R}$ is the same as knowing exactly all the trade-off occur between any couple of model parameters used in the inversion.

For a linear problem (Tarantola, 2005), if we consider an exact model that produce exact data ($\mathbf{d}_{in} = \mathbf{G}\mathbf{m}_{in}$), we can estimate the resolution operator as

$$\mathbf{m} - \mathbf{m}_0 = \mathbf{C}_M \mathbf{G}^T (\mathbf{G}\mathbf{C}_M \mathbf{G}^T + \mathbf{C}_D)^{-1} \mathbf{G}\ (\mathbf{m}_{in} - \mathbf{m}_0) \tag{1.7}$$

where ($\mathbf{m}_0$,$\mathbf{C}_M$) are the a-priori information on the model and

$$\mathbf{R} = \mathbf{C}_M \mathbf{G}^T (\mathbf{G}\mathbf{C}_M \mathbf{G}^T + \mathbf{C}_D)^{-1} \mathbf{G} \tag{1.8}$$

is the resolution matrix. Each row i of matrix $\mathbf{R}$ describes how independently the i-th parameter can be resolved from other parameters in the columns. A perfect resolution lead to $\mathbf{R}_{ii} = 1$ and $\mathbf{R}_{ij} = 0$, and $\mathbf{R}_{ij} \neq 0$ should be read as trade-off or coupling between the parameters i and j. It is not required that the resolution matrix be symmetric (Soldati and Boschi, 2005). Our problem is not linear but it can be linearized around the final solution for this purpose, with sufficient accuracy. In Figure 1.7, we calculated the resolution (1.7) and the covariance matrix (1.6) at

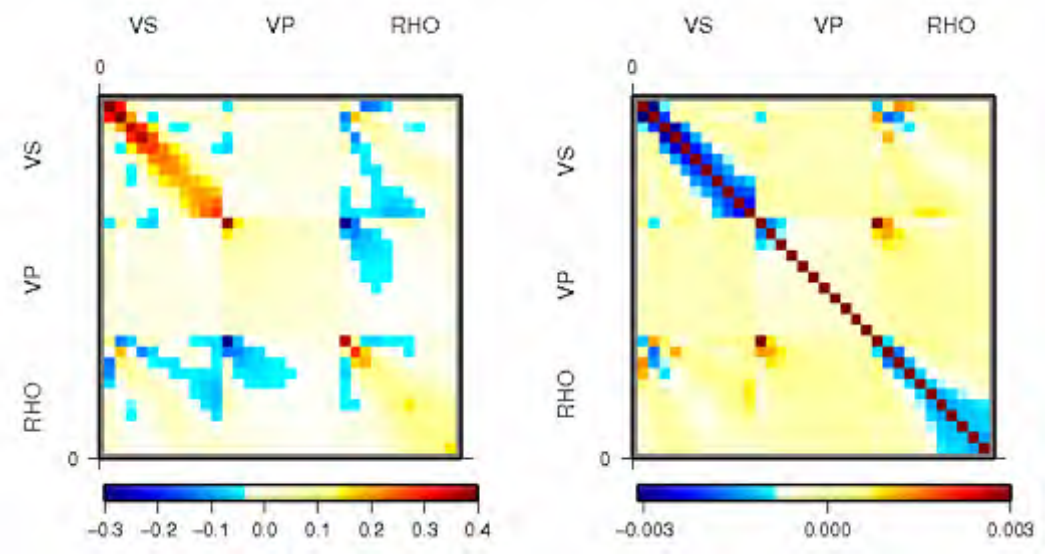

Figure 1.7: Resolution (left) and covariance (right) matrix at the last iteration for the inversion in the cell of 20 Lat N and 30 Lon W and for the 4KM model.

the last step of the inversions in the continental Lat=20 N and Lon= 30W cell (with a moho depth of 44 km) for the 4KM model. The first line of the resolution matrix, for examples, explains the trade-offs between V_s in the first layer of the model (row) with all the V_s parameters in all the layer of the model (in the first part of the row and going deeper while the number of the column is growing), then the same but with V_p and finally, with ρ. The determination of V_s in the first layer is correlated with V_s in the second layer and anti-correlated with ρ in the third, forth and fifth layer. For the parameterization choose, the most resolvable parameter is V_s but it's interesting to notice how large is the anti-correlation between the density in the first layer and the the velocity structures. It means that the information content in the dispersion curves, cannot resolve a increment of Vp or a decrement of rho, at least in the shallow layers. In contrast to what happened in the mantle, surface waves are strong influenced by the density structure of the shallow structure. However,

we decide to invert for all the parameters because we are looking for an equivalent model and it does not matter how parameters will be privileged during the inversion.

1.4 Results and considerations

Following the method explained in the previous section, we derive two different equivalent models fitting the CRUST2.0 dispersion curves performing the inversion for the whole Earth in $2° \times 2°$ cells. It is necessary to point out that to perform the first step of the inversion we need an a-priori model. What we call the 'a priori model' is the mean of CRUST2.0 over each layer in the parameterization of the final model (e.g. 4km or 12 km). The dispersion curves of CRUST2.0 are the data (**d**) we want reproduce.

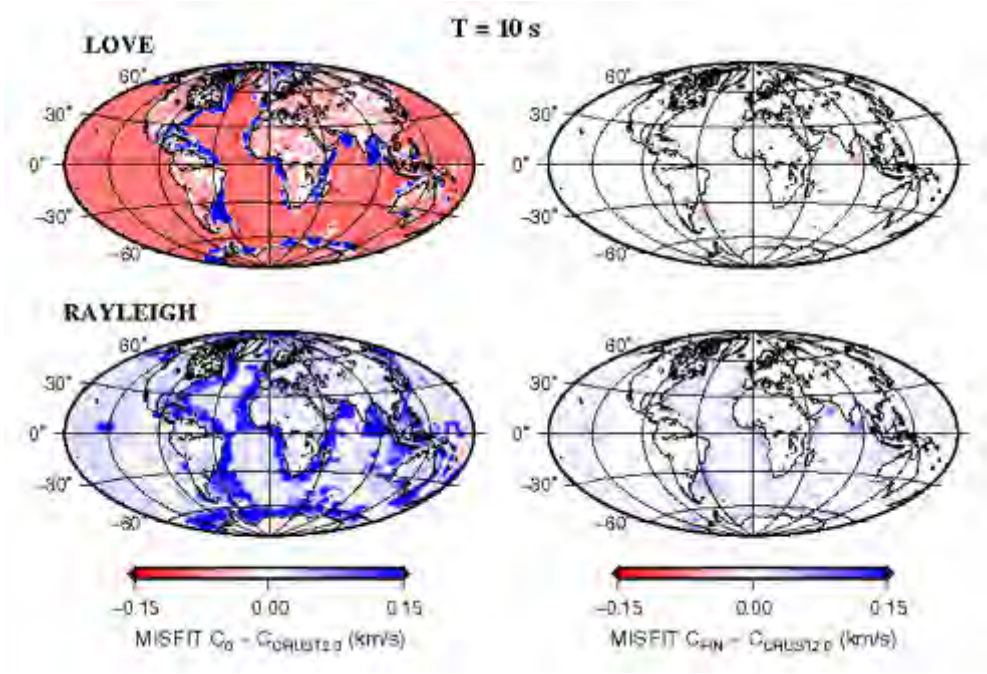

Figure 1.8: (left) Misfit between a-priori model and CRUST2.0 phase velocity at T=10s for Love (top) and Rayleigh wave (bottom). (right) Misfit between *CR-4KM* final model and CRUST2.0 phase velocity at T=10s for Love (top) and Rayleigh wave (bottom) for the whole Earth.

In Figures 1.8 and 1.9 we show the misfit, calculated as a simple difference, between the a-priori model and CRUST2.0, and between *4KM* final model and CRUST2.0 phase velocity at a fixed period (of 10s for *CR-4KM* model and 16s for *CR-12KM* model), for Love and Rayleigh wave in the whole Earth. From the left side of Figures 1.8 and 1.9 to the right, it is possible to appreciate the reduction,due to the inversion procedure, of the misfit on phase velocity. Of course, the amplitude of this reduction depend on the period considered: the shorter is the period, the higher is the reduction. Moreover, we note the higher difference in the dispersion curve in the

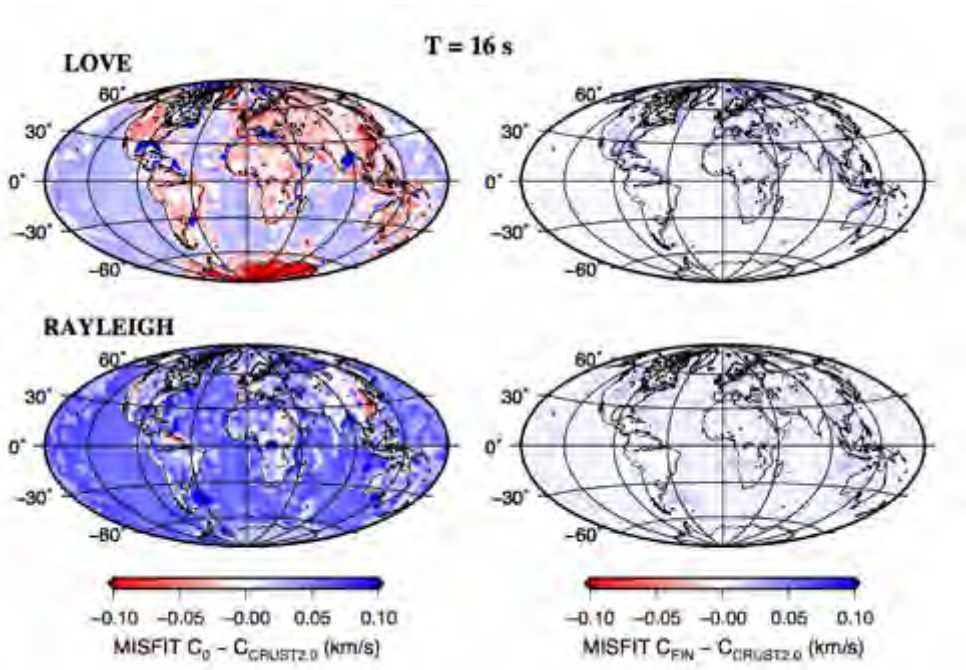

Figure 1.9: The same as in Figure (1.8) but for phase velocity at T=16s and for the *CR-12KM* model.

cells with a complex 1D velocity model in the shallow part. In these cases, we make the stronger approximation, as reducing the shallower layers in few 4km layers or in one 12 km layer. Also approximating the Moho depth at multiples of 4 or 12 play a role in the misfit between the phase velocity (for a fixed period) of the a-priori model and CRUST2.0 but it is less than the shallow simplifications. A surprising effects is that, in general, the shallower approximations have opposite effect on the short period dispersion curves for Love and Rayleigh waves. For example, in a same tile $2^\circ \times 2^\circ$, when we have to ri-parameterize a 1D model with non uniform layer thickness (and different parameters in each layer) into a uniform thickness grid averaging the parameters values, sometimes we get an increment on phase velocity for Rayleigh wave and a decrement for Love wave. In general, the misfit for phase velocity at 10 s before the inversion is more than 4-5 percent, due only to the approximations of the crustal structure. With the inversion we are able to sensibly reduce the error induced by the simplifications. A measure of the goodness of the inversions is the RMS_d (equation 1.5) for the whole data vector. The inversion is able to reduce the RMS to, at least, 80-90 percent for both the models: in Figures 1.10 and 1.11 we plot RMS_d for the whole Earth before (left) and after the inversion (right) for the *CR-4KM* and *CR-12KM* models respectively. The regions where we still have a relatively high misfit (after the inversion) are mainly concentrated in the continent-ocean boundary. In our opinion, this is due to complex crustal structure assigned by CRUST2.0 in that regions. Here, we often find sedimentary basin or relatively low velocity structure that make our approximations stronger and consequentially

increment the non-linearity of the inversion.

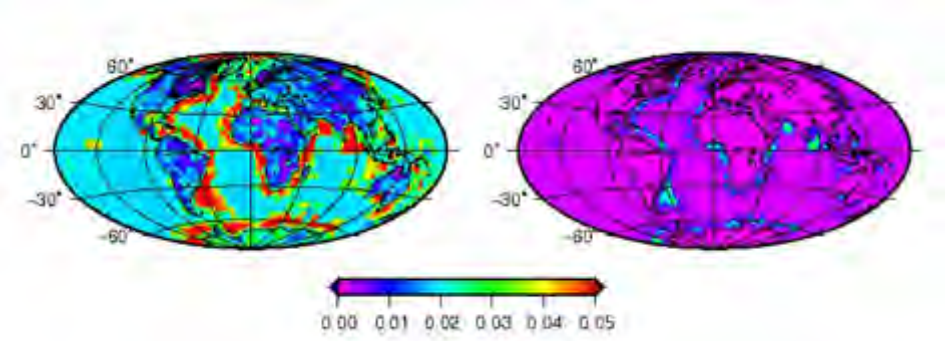

Figure 1.10: (left) RMS_d (1.5) for the a-priori model and CRUST2.0 (right) on whole dispersion curves RMS_d between final 4KM model and CRUST2.0, after the inversion.

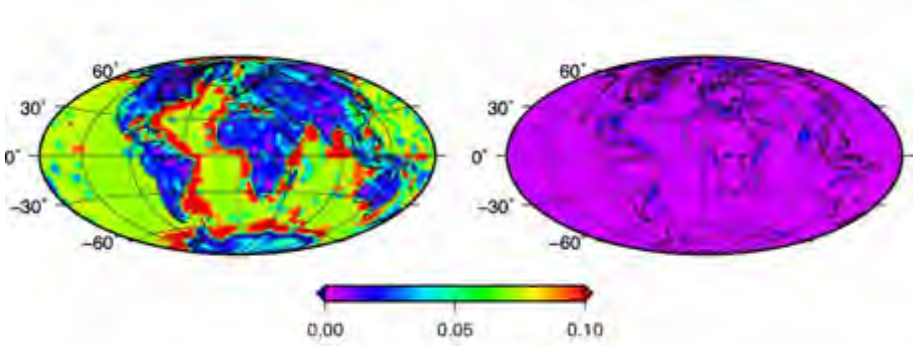

Figure 1.11: (left) RMS_d (1.5) between a-priori model and CRUST2.0 and (right) RMS_d between final 12KM model and CRUST2.0, after the inversion.

Once we are sure that the inversion does a better job than our first approximation (average of parameters used to create the a-priori model), we can have a look of the equivalent models found. Figure 1.12 shows the v_S structure at different depths (rows) for CRUST2.0, *CR-4KM* and *CR-12KM* (columns). The three models mainly differ in the shallower layers (first row Figure 1.12) and, in particular in the oceans, we found that CRUST2.0 is slower than the equivalents models while in the continental area the velocity is comparable. Going deeper, the models are somehow comparable (in the oceanic areas after 16 km depth we are in the mantle) and differences are noticed mainly in the continents. To explain these results, it is important to point out that we inverted also for v_S and ρ and our equivalent models differ from the original also for these two parameters, in particular in the shallower layers (where the sensitivity is remarkable). Our finals models, considering all the elastic parameters, are equivalent to CRUST2.0 respect to dispersion of phase velocity of surface waves in a period range within 10 and 120 seconds, and can be considered

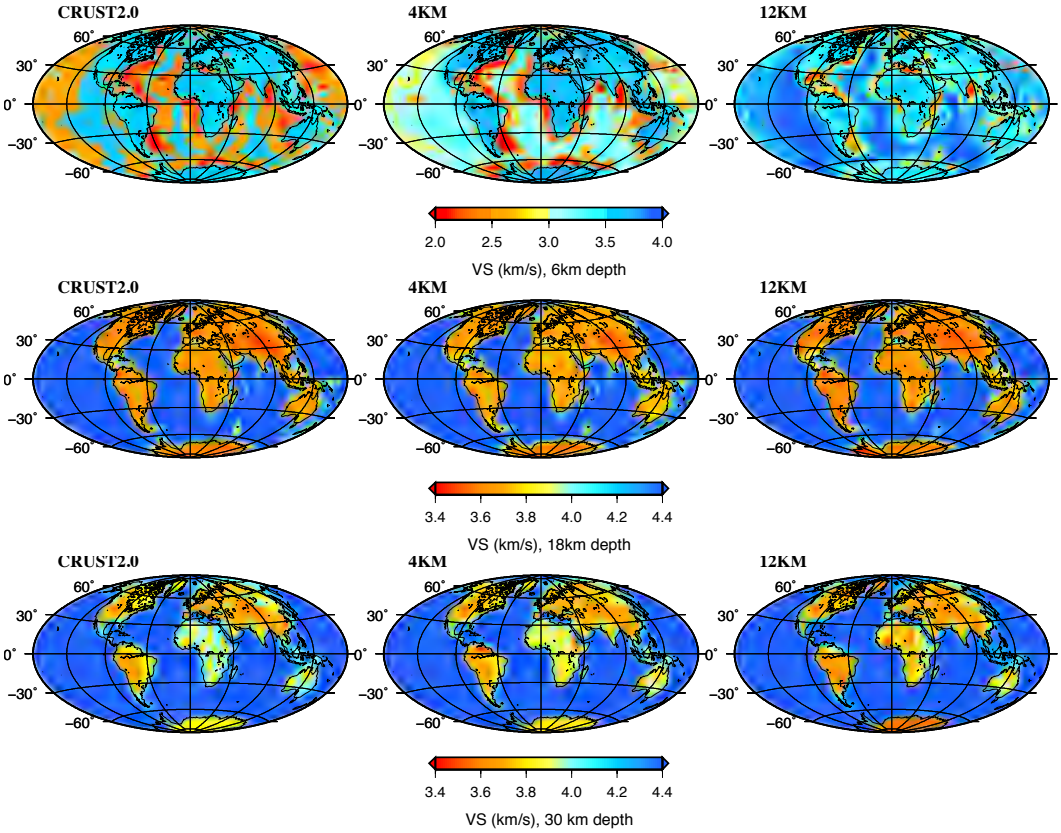

Figure 1.12: Comparison of V_s for CRUST2.0 (left), 4KM model (center), 12KM model (right) at 6 (top), 18 (middle) and 30 (bottom) km depth.

as different representations of the same crustal structure.

1.5 Simulations with SPECFEM3D-Globe

The next step was to demonstrate that our model are equivalent to CRUST2.0 also in a wave propagation sense: the waveforms simulated in the models should be the same at least for the period range used in the inversion.
In order to validate our parametrically simplified models and to investigate the impact on wave propagation, we performed numerical 3D simulations using a spectral element method (SEM) as implemented in the SPECFEM3D-GLOBE code (Komatitsch and Tromp, 2002). Details about the code and the spectral element method are explained in the Appendix C. We modify the SPECFEM-3D code, and in particular the routine *crustal_model.f90*, to implement in the mesh our crustal models. CRUST2.0 was already available in this software.
We used a $90° \times 90°$ mesh centred in the European region and simulate a $M = 6.3$ Peloponnesus earthquake occurred on 8 June 2008 (Figure 1.13). The vertical resolu-

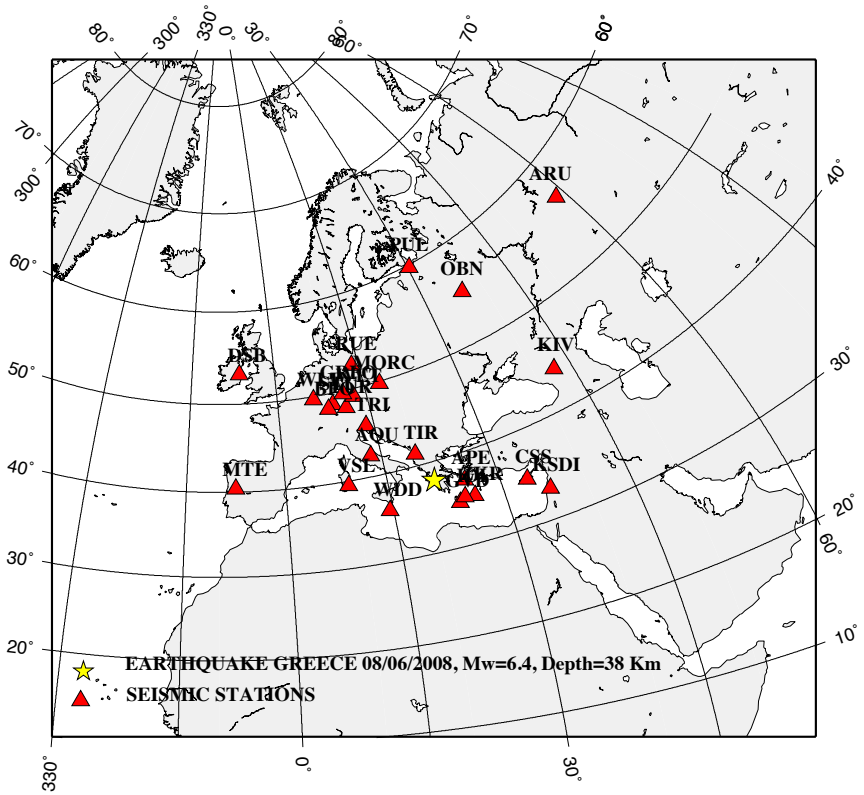

Figure 1.13: Map of the meshed region. We also show the position of the epicenter end some stations used in the simulations.

tion of the uppermost crustal part of the numerical mesh was increased to 4 layers of spectral elements (4th order) to improve the representation of shallow structures. We calculated synthetic seismograms for stations in the European region using different representation of crustal structure: CRUST2.0, as implemented in SPECFEM3D, and both our models *CR-4KM* and *CR-12km*. We visually compare the synthetics, at which we apply a low-pass filter with a corner frequency of 0.05 Hz (20 s), from different models and in general, we note a good match between the waveforms. We cannot expect acceptable fits at periods less than $15 - 20$ s because we obtain the equivalents models matching the surface wave dispersion curves between $10 - 15$ to 120 seconds. Few examples are shown in Figure 1.14 and Figure 1.15. We note some minor, but significant, differences, especially in the later parts and the coda of the seismograms. In general, *CR-4KM* model better reproduce CRUST2.0 seimograms

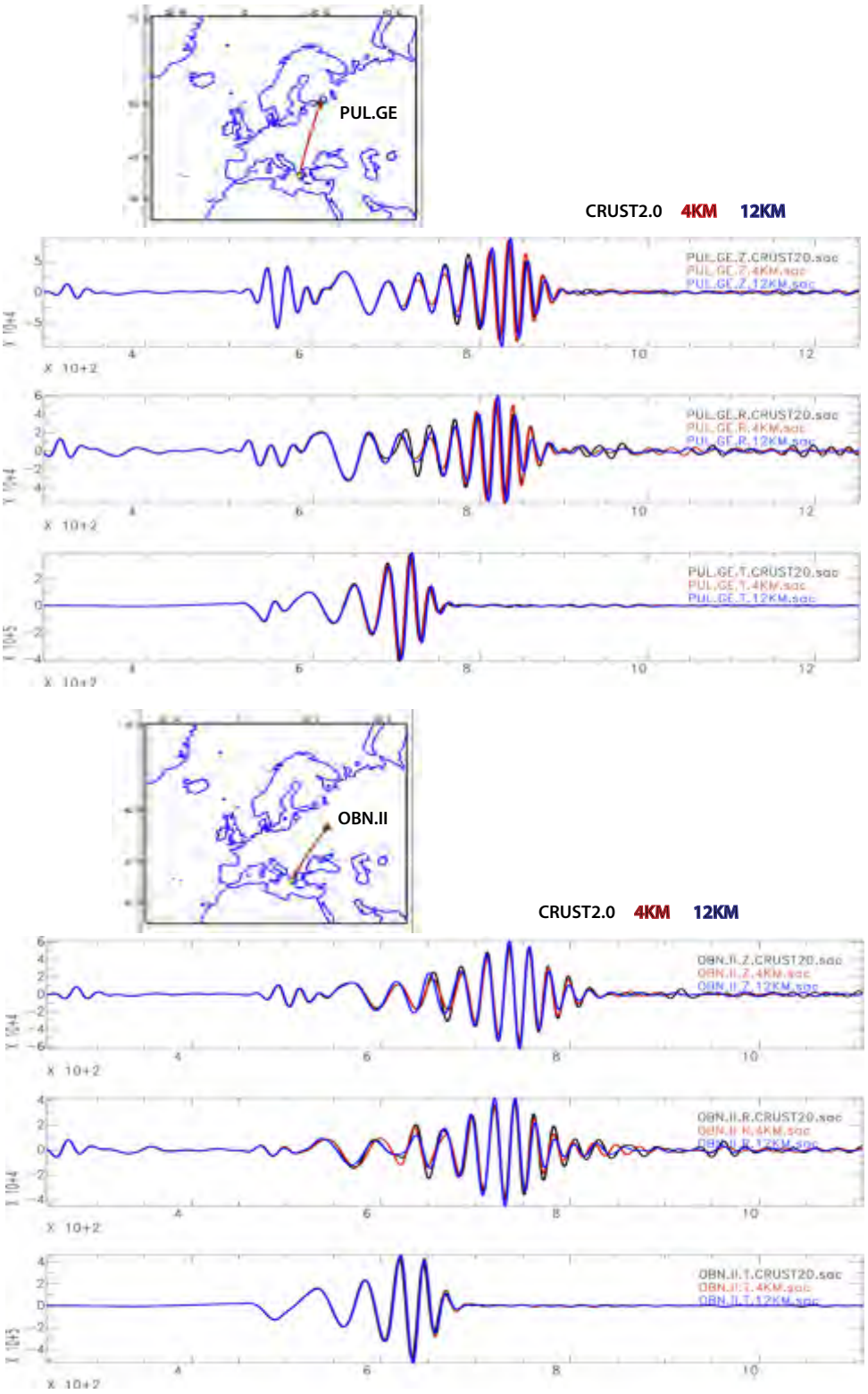

Figure 1.14: Comparison of synthetics recorded at PUL station (top), OBN station (bottom) using CRUST2.0 (black), *CR-4KM* (red), and *CR-12KM* (blue). The signals are low pass filtered with corner frequency of 0.05 Hz.

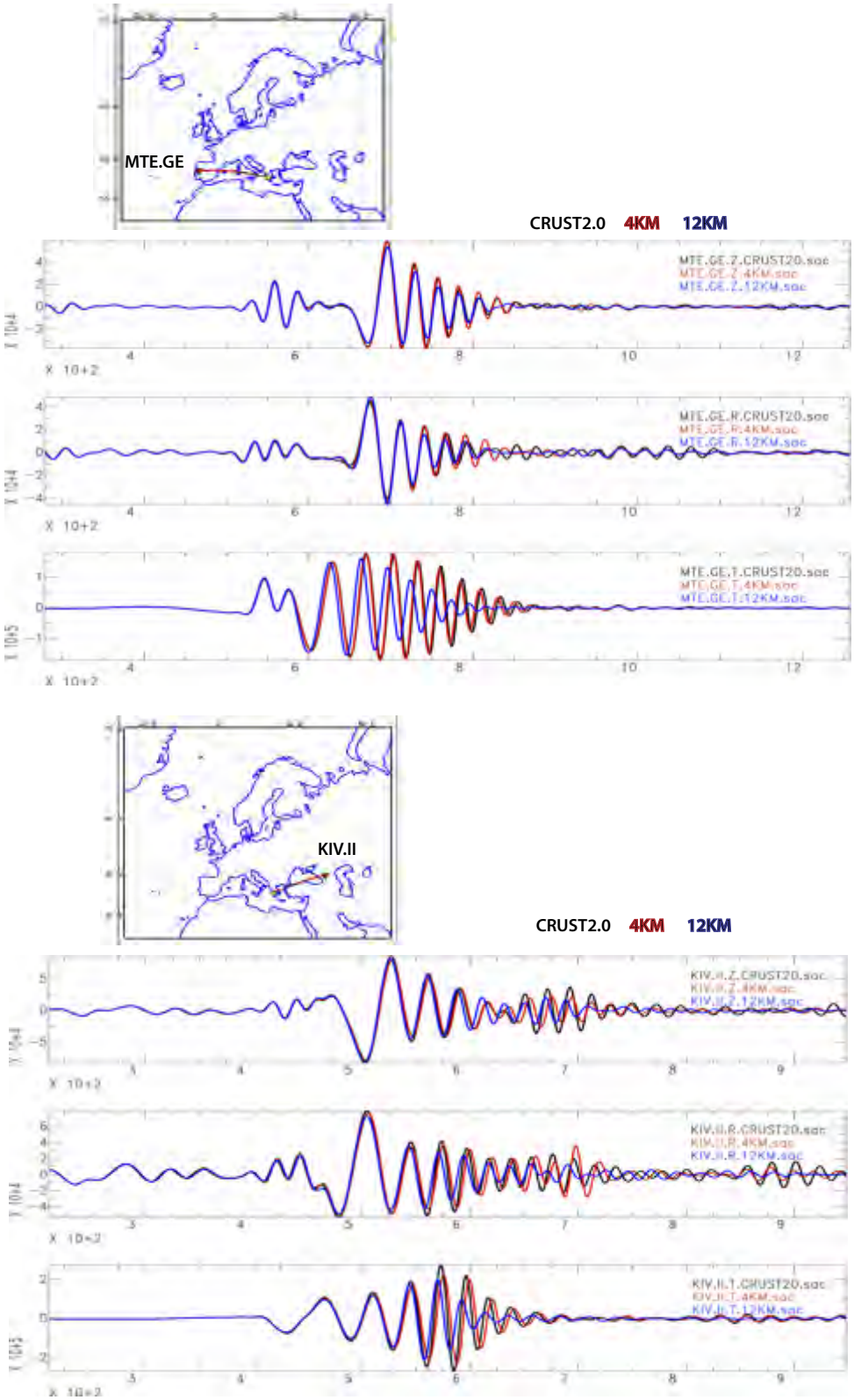

Figure 1.15: Comparison of synthetics recorded at MTE station (top), KIV station (bottom) using CRUST2.0 (black), *CR-4KM* (red), and *CR-12KM* (blue). The signals are low pass filtered with corner frequency of 0.05 Hz.

than *CR-12KM*. This is due to the minor approximations use to construct this representation respect to the ones used in *CR-12KM*. In particular this is true for the transverse component of the seismograms in which the energy is mostly due to the Love wave train because the are very sensitive to the shallowest structure (more than Rayleigh wave). This can be seen, for example, in Figure 1.15 for both the stations displayed: as we expected, the *CR-4KM* models shows better fits. During this part of the work, we do not measure the misfit between the seismograms. For a measure of misfit, applied to other comparisons, see Chapter 4 and 5.

1.6 Conclusion

Applying surface wave dispersion curve matching, we have been able to obtain models with uniform, constant-thickness layers that reproduce the seismological behaviour of CRUST2.0. This allowed a substantial decrease in complexity of the crustal model, with no significant degradation of performance, also tested with SEM synthetics.
We can predictably point out that a better knowledge of crustal structure is needed for accurate simulation of wave propagation at continental scale and we also emphasize that an accurate representation of the crustal structure in meshes used in numerical codes is also very important at this distance range. Moreover, from the differences noted in the seismogram also at 20 second, we point out that the parameterization chosen should match the specific use and needs.

References

Aki, K., Richard, P.G., 2002. Quantitative seismology. University Science Books, Sausalito, California. 2 edition.

Bassin, C., Laske, G., Masters, G., 2000. The current limits of resolution for surface wave tomography in North America. Eos Trans. AGU 81, 48.

Bozdag, E., Trampert, J., 2008. On crustal corrections in surface wave tomography. Geophys. J. Int. 172(3), 1066–1082. doi:10.1111/j.1365-246X.2007.03690.x.

Capdeville, Y., Marigo, J., 2008. Shallow layer correction for Spectral Element like methods. Geophys. J. Int. 172(3), 1135–1150. doi:10.1111/j.1365-246X.2007.03703.x.

Dziewonski, A.M., Anderson, D.L., 1981. Preliminary reference earth model. Phys. Earth Planet Inter. 25, 297Ð356.

Fichtner, A., Igel, H., 2008. Efficient numerical surface wave propagation through the optimization of discrete crustal models-a technique based on non-linear dispersion curve

matching (DCM). Geophys. J. Int. 173(2), 519–533. doi:10.1111/j.1365-246X.2008.03746.x.

Komatitsch, D., Tromp, J., 2002. Spectral-element simulations of global seismic wave propagation: I. validation. Geophysical Journal International 149(2), 390–412.

Soldati, G., Boschi, L., 2005. The resolution of whole earth seismic tomographic models. Geophys. J. Int 161, 143–153.

Takeuchi, H., Saito, M., 1972. Seismic surface waves. Methods. Comput. Phys 11, 217–295.

Tarantola, A., 2005. Inverse problem theory and method for model parameter estimation. SIAM, Philadelphia.

Tesauro, M., Kaban, M.K., Cloetingh, S.A.P.L., 2008. EuCRUST-07: a new reference model for the European crust. Geophys. Res. Lett. 35, L05313. doi:10.1029/2007GL032244.

Chapter 2

EPcrust: A reference crustal model for the European plate

Contents

2.1 Introduction

Knowledge of crustal structure is crucial for many applications, such as upper-mantle tomographic studies (e.g., Bozdag and Trampert, 2008; Ritsema et al., 2009), gravity modeling (Yegorova and Starostenko, 2002), forward seismic wave propagation (e.g., Capdeville and Marigo, 2008), dynamic topography studies (e.g., Faccenna and Becker, 2010) and location of seismic events (e.g., Bisio et al., 2004).

Seismic waves are very sensitive to crustal structure, but, in the frequency range and ray geometries mostly used in seismic tomography, they are not able to discriminate uniquely between the structure of the crust and that of the mantle below. For instance, the propagation of surface waves, both Rayleigh and Love, with period T $>$ 35 s — used, for instance, to calculate seismic moment tensors (e.g., Pondrelli et al., 2007) and to image lithospheric structure (e.g., Schivardi and Morelli, 2009) — is heavily affected by the strong heterogeneities in the Earth's crust. However, their sensitivity to shear-wave speed is spread over both crust and mantle, generating large trade-off between wave speed above and below the Moho. The reduced sensitivity to the velocity jump at the Moho, and to the depth of the discontinuity does not permit the inversion for these parameters in conjunction with seismic wave speed in the mantle.

Focusing the attention on the European continent — where abundant data are available, and the geological structure is quite complex — it becomes clear that current crustal models are not fully adequate for modeling regional datasets with enough detail. The global model CRUST2.0 (Bassin et al., 2000) is frequently

Published as: Molinari I, & Morelli A. – *"EPcrust: A reference crustal model for the European plate,"* Geophys. J. Int. 2011. doi: 10.1111/j.1365-246X.2011.04940.x

used for crustal correction, but its resolution ($2° \times 2°$) is too low for continental-scale studies (Molinari and Morelli, 2009). Some European-scale crustal models are available (Tesauro et al., 2008; Bassin et al., 2000; Ritzmann et al., 2007), but none of them possesses all the desired properties for a complete reference crustal model: either because of a low resolution, a limited geographical extent, or lack of description of some seismic parameter, such as v_S.

Local studies can overcome these limitations. Receiver functions provide point determinations of Moho depth and constraints on the velocity structure in the European crust (e.g., Piana Agostinetti and Amato, 2009; Kumar et al., 2007; Geissler et al., 2008), but such determinations are not dense and extended enough to draw a wide geographical surface. They can however be used to calibrate and improve existing models. Seismic reflection/refraction experiments (e.g., Guterch et al., 2003; Wilde-Piorko et al., 2008; Grad et al., 2003) present the best capability to image crustal structure, and resulting profiles have extensively been used to create local 3D models (e.g., Guterch et al., 2005; Diaz and Gallart, 2009; Stratford et al., 2009). Recent studies have shown that cross correlation functions of seismic noise computed at two receivers contains the Green's function between these two receivers, i.e. the waveform that would be recorded at one of the stations if a point force source was applied at the other station. This provides the possibility of measuring relatively high-frequency surface waves for many short paths. High-frequency surface waves have their sensitivity concentrated in the crust, and their inversion permits the reconstruction the structure (e.g., Stehly et al., 2009). However, such studies are for now limited to sub-regions of the whole European Plate, so by themselves they have not (yet) provided a whole European model.

A lot of detailed information on European crustal structure therefore exists, but at different scales and following different formats. This information needs to be merged into a larger-scale, coherent representation. Our purpose is to sketch the seismological description of the complex crustal structure of the European Plate with a higher resolution and more plausibility than it is offered by existing models. We collected the information currently available from different sources, ranging from active-source seismic profiles, to receiver function studies, to digital maps and models. These large-scale and regional models concur to construct a new comprehensive reference model for the European region: EPcrust. In the next sections we describe the initial models and datasets used, the methodology adopted to create the new model, and we discuss our results in function of the geological setting of the European plate.

2.2 Datasets

As a first step in our effort, we collected available models and information about the European crust. We selected preferentially more recent studies, and evaluated their significance and confidence level. Our goal is to create a model for the whole European plate, from North Africa to the North Pole (20°N - 90°N) and from the

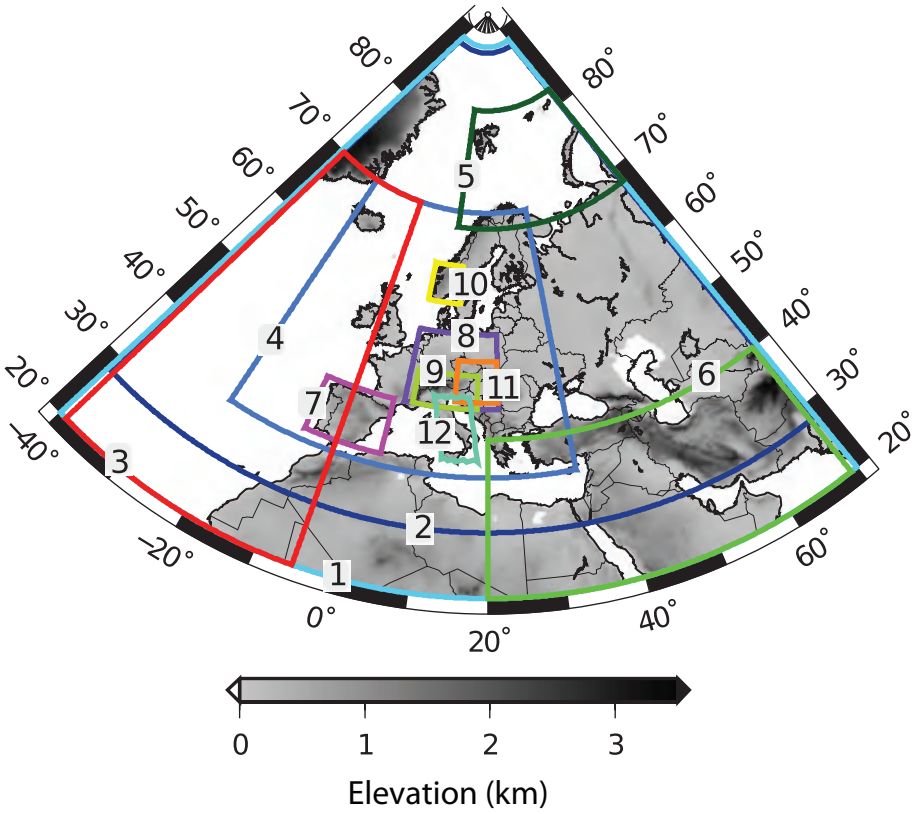

Figure 2.1: Geographical coverage of the models considered: 1) CRUST2.0 (Bassin et al., 2000), sediment map (Laske and Masters, 1997) and Meier crustal model (Meier et al., 2007); 2) ESC Moho (Grad et al., 2009); 3) NOAA sediment thickness; 4) EuCRUST-07 (Tesauro et al., 2008); 5) BARENTS50 (Ritzmann et al., 2007); 6) AsCRUST-08 (Baranov, 2010); 7) Iberian Peninsula Moho (Diaz and Gallart, 2009); 8) Moho depth from RF (Kind, 2009); 9) Alps model (Stehly et al., 2009); 10) Norwegian Moho map (Stratford et al., 2009); 11) Eastern Alps model (Molinari et al., 2010b); 12) Italian Moho depth from receiver functions (Piana Agostinetti and Amato, 2009).

Mid-Atlantic Ridge to the Urals (40°W - 70°E). In the following, we provide an overview of the data used. In Table 2.1 we summarize all the contributions used to assembly EPcrust, and in Table 2.2 we specify the information included in these contributions. The different regions covered by the original models are shown in Figure 2.1.

Perhaps the most commonly used description for the crust at a global scale is CRUST2.0 (Bassin et al., 2000). CRUST2.0 is a good global model, but its resolution is too low for regional or continental scale work: in fact, Moho depth defined on $2° \times 2°$ pixels cannot account for important features (e.g. Moho undulations under Alps and Apennines) that are relevant to seismic wave propagation at this scale. Also, CRUST2.0 has sharp tile edges, and a rather complex vertical layering and discontinuous lateral steps, that make it difficult either to represent the model with

fidelity in numerical codes, or to smooth it laterally (Molinari and Morelli, 2009). Another global model is due to Meier et al. (2007), who derived it by inversion of surface wave data. This model has a simpler parameterization, providing thickness and average S velocity at the same resolution of $2° \times 2°$. We use these global models as a background for our final model, as they provide information where more detailed studies are unavailable.

Moho depth is certainly the single best known parameter of the crust. Significant efforts have recently been devoted to deriving Moho maps of different sub-regions of Europe. We collected several models, limited to the description of Moho depth only, for inclusion in our compilation. As a result of a very substantial effort carried on by a Working Group specifically set by the European Seismological Commission, a digital Moho depth map has recently been compiled by assembling more than 250 data sets of individual seismic profiles, 3D models obtained by body and surface waves, receiver function results, and maps of seismic and/or gravity data compilations (Grad et al., 2009). This study represents the first digital, high resolution map of Moho depth for the whole European plate extending from the Ural Mountains in the east, to mid-Atlantic ridge in the west, and from the Mediterranean Sea in the south, to the Barents Sea and Spitsbergen in Arctic in the north (available online at *http://www.seismo.helsinki.fi/mohomap/*). Because of its recent development, and the broad data compilation that went into it, we consider this study as a reliable reference at a large scale for Moho depth. In a more local framework, Diaz and Gallart (2009) and Stratford et al. (2009) compiled Moho maps, respectively of the Iberian Peninsula and southern Norway. Both maps are derived from interpolation of a collection of seismic profiles published in the past. The Iberian Peninsula map has been derived collecting and revising the most relevant seismic experiments carried on in the area in the last three decades, and then interpolating the geo-referred database, using a kriging algorithm, to come up with a continuous Moho depth model. By using receiver function analysis it is also possible to obtain reliable estimates about the Moho depth and the crustal v_P/v_S ratio under the recording seismic station. Piana Agostinetti and Amato (2009) derive a new dataset of the Moho depth in the Italian peninsula using more than 270 teleseismic event recorded at the 127 stations of the Italian National Seismic Network. In addition, we also collect a Moho depth dataset in the central Europe from receiver functions provided to us by Kind (2009) from which we derive a map in this region interpolating Moho values.

For the areas where they exist, regional models can provide reliable descriptions of crustal geometry, as well as values of seismic parameters inside. Recently, Baranov (2010) improved the knowledge of the Central and Souther Asia and surrounding regions compiling AsCRUST-09, a $1° \times 1°$ model of the crystalline crust, from an interpolation of a collection of seismic refraction and reflection data. The westernmost part of this model, that overlaps our region of interest (Figure 2.1), appears to be well constrained by the presence of many seismic profiles. EuCRUST-07 (Tesauro et al., 2008) is instead a digital model for the crust of Western and Central Europe and surroundings ($35°N - 71°N$, $25°W - 35°E$) based on the assemblage of available results of seismic reflection, refraction and receiver functions studies into an inte-

grated model at a uniform grid ($15' \times 15'$). EuCRUST-07 consists of three layers: sediments and two layers of the crystalline crust. Besides depth to the boundaries, EuCRUST-07 provides average P-wave velocities in the upper and lower parts of the crystalline crust but lacks one of the sedimentary layer. This study shows large differences in the Moho depth compared to previous compilations, more than ± 10 km in some specific areas (e.g. the Baltic Shield). Furthermore, the velocity structure of the crust is much more heterogeneous than in previous maps.

On a more local scale, BARENTS50 (Ritzmann et al., 2007) has been generated by analysis and interpolation of 680 individual seismic profiles in the western Barents Sea to assemble a 3D crustal model of the region with a resolution of 50×50 km. The Authors used a compilation strategy based on the definition of geological provinces to produce a model with a parametrization in sediment layers (soft and hard), upper, middle and lower crust, providing all the seismic parameters.

We also use the $1^\circ \times 1^\circ$ world sediment map by Laske and Masters (1997) –from now on called LM97– , and the $5' \times 5'$ thickness map of the oceanic sediments due to Divins (2003). The Laske and Masters (1997) three-layer sediment model has been obtained, for continental areas, by digitizing the Tectonic Map of the World assembled by the EXXON Production Research Group (1985) and, for oceanic areas, by averaging other published high-resolution maps (e.g. Pacific, Indian and South Atlantic oceans). For regions where digital information was unavailable (e.g. Arctic and North Atlantic ocean), the sediment thickness has been hand-digitized from atlases and maps
(http://igppweb.ucsd.edu/~gabi/sediment.html). Each sediment layer has been assigned a P-wave speed, obtained using regional velocity functions for the oceans, and seismic reflection/refraction profiles, complemented by values given by CRUST5.1 (Mooney et al., 1998) for the continents.

These datasets provide information within a wide range of resolution and expected accuracy. Moho depth and sediment thickness are however the best constrained parameters (Table 2.2, a total of 12 and 7 models, respectively), while the Conrad discontinuity between upper and lower crystalline crust is poorly constrained, and is mostly derived from EuCRUST-07 and global models only (with the exceptions of the Barents Sea model and East Alps model). From a geographical point of view, the regions best covered are the Alps, Central Europe, the Italian peninsula, Spain, and Barents Sea, while in North Africa and in East Europe, we only have global models available (CRUST2.0 and Meier et al. (2007)). Where we have more than one crustal measurement we found differences among the datasets: in particular for Moho depth we found differences at times exceeding 15 km. We see considerable differences also in the shape and thickness of sedimentary basins, in some cases of more than 6-8 km (i.e. the Po plain is more than 12 km thick in EuCRUST-07, while in Laske Sediment Map it is about 4 km). Of course, higher resolution models (such as BARENTS50, EuCRUST-07, Italian and Iberian Moho maps) provide presumably better constrained details on the geological structure.

Table 2.1: All contributions used to assembly EPcrust. For each model is specified: name and reference, covered region, resolution, year of publication, presence of error bar, assigned weight in EPcrust.

Model name	Region	Resolution	Year	Error bars	Weight
CRUST2.0 (Bassin et al., 2000)	globe	$2° \times 2°$	2000	yes	1
EuCRUST-07 (Tesauro et al., 2008)	25°W-35°E/35°N-71°N	$0.25° \times 0.25°$	2007	no	100
ESC Moho (Grad et al., 2009)	40°W-70°E/28°N-86°N	$0.1° \times 0.1°$	2009	yes	100
BARENTS50 (Ritzmann et al., 2007)	20°E-155°E/10°N-55°N	50 km×50 km	2007	no	100
AsCRUST-08 (Baranov, 2010)	10°E-70°E/62°N-82°N	$1° \times 1°$	2010	no	10
LM97 sediment map (Laske and Masters, 1997)	globe	$1° \times 1°$	1999	no	1
Sediment NOAA (Divins, 2003)	ocean	$5' \times 5'$	2003	no	10
Alps model (Stehly et al., 2009)	5°E-13°E/44°N-49°N	25 km×25 km	2009	yes	100
East Alps model (Molinari et al., 2010b)	14°E-22°E/45°N-50°N	$0.1° \times 0.1°$	2010	no	150
Iberian Moho (Diaz and Gallart, 2009)	10°E-5°E/35°N-46°N	$0.5° \times 0.5°$	2009	no	150
Italian Moho (Piana Agostinetti and Amato, 2009)	italian Peninsula	points	2010	yes	150
Norwegian Moho (Stratford et al., 2009)	5°E-13°E/58°N-63°N	points	2010	no	150
RF (Kind, 2009)	Central Europe	points	2009	no	50
Meier model (Meier et al., 2007)	globe	$2° \times 2°$	2007	yes	1
ETOPO1 (Amante and Eakins, 2009)	globe	$1' \times 1'$	2009	no	-

Table 2.2: Information on crustal structure included in the contributions used to assembly EPcrust

Model name	Sediment				Upper crust				Middle crust				Lower crust				Moho	Topo-
	h	Vp	Vs	ρ	h	Vp	Vs	ρ	h	Vp	Vs	ρ	h	Vp	Vs	ρ	depth	graphy
CRUST2.0	X	X	X	X	X	X	X	X	X	X	X	X	X	X	X	X	X	X
EuCRUST-07	X	-	-	-	X	X	-	-	-	-	-	-	X	X	-	-	X	X
ESC Moho	-	-	-	-	-	-	-	-	-	-	-	-	-	-	-	-	X	-
BARENTS50	X	X	X	X	X	X	X	X	X	X	X	X	X	X	X	X	X	X
AsCRUST-08	X	-	-	X	X	X	-	X	X	X	-	X	X	X	-	X	X	X
LM97	X	X	X	X	-	-	-	-	-	-	-	-	-	-	-	-	-	-
Sediment NOAA	X	-	-	-	-	-	-	-	-	-	-	-	-	-	-	-	-	-
Alps model	-	-	X	-	-	-	X	-	-	-	-	-	-	-	X	-	X	-
East Alps model	X	-	-	-	X	X	-	-	-	-	-	-	X	X	-	-	X	-
Iberian Moho	-	-	-	-	-	-	-	-	-	-	-	-	-	-	-	-	X	-
Italian Moho	-	-	-	-	-	-	-	-	-	-	-	-	-	-	-	-	X	-
Norwegian Moho	-	-	-	-	-	-	-	-	-	-	-	-	-	-	-	-	X	-
RF	-	-	-	-	-	-	-	-	-	-	-	-	-	-	-	-	X	-
Meier model	-	-	-	-	-	-	-	-	-	-	-	-	-	-	-	-	X	-
ETOPO1	-	-	-	-	-	-	-	-	-	-	-	-	-	-	-	-	-	X

2.3 Model construction

EPcrust is constructed by joining information from all the global, regional, and local models described in the previous section. The approach of combining a priori information, rather than fitting data solving an inverse problem, has been adopted for a number of crustal models, with different spatial scales, such as CRUST2.0 (Bassin et al., 2000), 3SMAC (Nataf and Ricard, 1996), WENA1.0 (Pasyanos et al., 2004), AsCRUST-08 (Baranov, 2010), EurID (Du et al., 1998). The procedure consists of collecting and amalgamating reliable, although scattered, information about the crust in the region of interest from a variety of studies, done using diverse data and approaches and characterized by different merits and drawbacks. As such, the resulting model should attempt to retain the best from each constituent and render it with a uniform representation.

The region covered by the new model is the whole European plate from North Africa to the North Pole (20°N - 90°N) and from the Mid-Atlantic Ridge to the Urals (40°W - 70°E, Figure 1). We represent the crust with three layers (sediments, upper crust and lower crust) in each specifying P and S velocity and density, with a resolution of $0.5° \times 0.5°$ on a geographical latitude-longitude grid. We actually work with a $0.1° \times 0.1°$ pixel size, but then decimate the grid (after anti-aliasing filtering) to the target $0.5° \times 0.5°$ pixels. The longitude-latitude coordinates are defined as geodetic coordinates in WGS84 reference system, the elevation is referred to the reference ellipsoid, and, between grid points, the model is defined using a bilinear interpolation.

In principle, we could distinguish among soft, intermediate or hard sediments; and upper, middle or lower crystalline crust. However, it is seldom possible to find out information about such interfaces and distinct seismic properties. In fact, just a few of the models we collected (Bassin et al., 2000; Ritzmann et al., 2007; Baranov, 2010) have such high detail in depth, unfortunately coupled to poor resolution horizontally. We thus chose to adopt the simple vertical parameterization, consisting of a sedimentary and two cristalline layers (e.g., (Tesauro et al., 2008)). We did not find any added vertical complexity justified by quality of available information, at the geographical scale of work, or improved ability to model seismic wave propagation. Our goal is a model that can readily be used for the main seismological applications, such as surface wave tomography, P-wave tomography, density inversion from gravity data, dynamic topography calculation and wave-form simulations. Note that fewer crustal layers are easier to honor in a 3-D mesh, necessary for numerical modeling of seismic wave propagation (Molinari et al., 2010a).

We proceed as follows. First of all, global and local models are re-gridded to our own parameterization. We select the portion of original models that lies in our region of interest and then we obtain the information of interest — such as depth (or thickness) of sedimentary basins; depth of upper, middle and lower crust and velocity structure of these layers. Some models considered have a different layer parameterization than EPcrust. For instance, the sedimentary layer may be divided into soft, middle and hard sediments, such as in the sediment map of Laske and

Masters (1997); or the crystalline crust may be divided in more than just an upper and a lower layer, such as in CRUST2.0, AsCRUST-08, BARENTS50. In these cases, the model has to be reduced to our vertical three-layer description. For the crystalline crust, as a general rule, we decide to merge together middle and lower crust into our lower crustal layer. This choice is justified considering that in the models used middle and lower crust have more similar velocity value than upper and middle crust (mean value of P speed: upper crust $= 5 - 6.3$ km/s, middle crust $= 6.5 - 6.8$ km/s and lower crust $= 6.8 - 7.3$ km/s). For simplicity, we take the total thickness of the layers and, in order to assign a value of the elastic properties, we made a mean weighted with the sublayer thickness. It may be possible to apply more sophisticated and expensive approaches (Fichtner and Igel, 2008; Molinari and Morelli, 2009) that ensure strictly equivalent behaviour of a simplified model for instance for surface wave propagation, but such procedures appear specialized for specific seismological applications and do not appear appropriate for the present study. Once the model has the same vertical parameterization, each layer is re-gridded on a finer working mesh of $0.1^\circ \times 0.1^\circ$.

To include point determinations, such as Moho depth from receiver functions, we first need to create a surface (with a grid resolution of $0.1^\circ \times 0.1^\circ$) that honors all the data, and interpolates values between data points. We use the simple *surface* tool of the Generic Mapping Tools (Wessel and Smith, 1998) and the ordinary kriging method as implemented by SGeM software (Remy et al., 2009).

With all the data reported on grids with the same resolution it is possible to assemble the final model. For each parameter (sediment thickness, upper-lower crustal depth, Moho depth, v_P in sedimentary, upper and lower crustal layers) all the maps are then merged into the wide mesh covering the whole European plate. In most regions, for each grid point more than one estimate of the same parameter is available (Figure 2.1). We could then decide and pick for every point the 'best' estimate neglecting the others. However, considering that we have no strict criterion to evaluate the 'goodness' of a model — especially since most of them do not even supply error bars — we proceed differently and average the multiple determinations, with weights chosen to represent a scale of reliability. In principle, this corresponds to the way of combining information with different Gaussian uncertainties multiplying their probability density functions. One could argue that, in the case we have a very detailed result in a region where bad previous knowledge existed, we spoil this high-quality study. However, we note that the weighting scheme can certainly limit this possible pollution to a minimum, and that it would be inappropriate to just hardly cut off pre-existing information that we are not in a position to completely rule out (note that we do not even consider older studies with dubious reliability). Local, recent, high-resolution models overlap with larger scale ones. As we must trust the large scale model for areas outside the local study, it is undesirable to introduce artificial lineaments along local borders. Assignment of weights remain somehow subjective. A weight is assigned to each model (Table 2.1, last column) on the basis of the date of publication, the original resolution, the number of dataset and the method used in the paper to construct the model. Figure 2.2 shows the log-

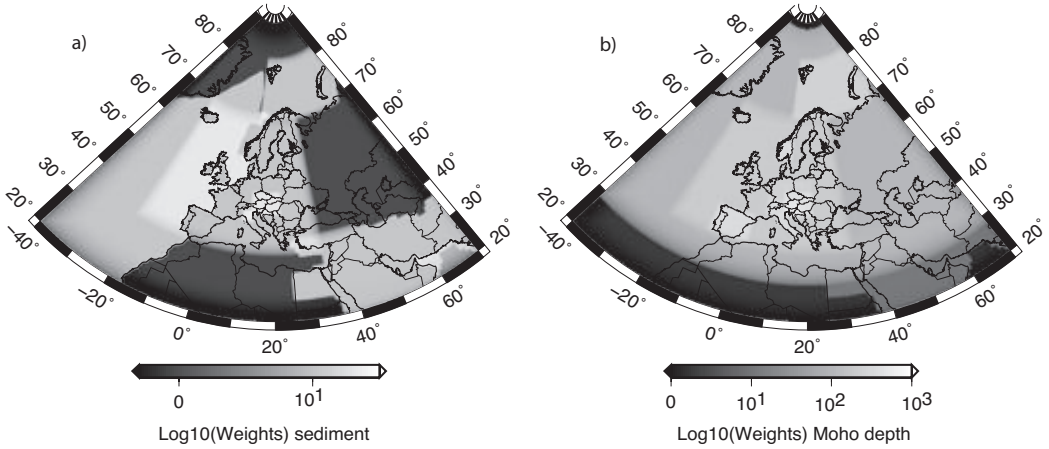

Figure 2.2: Sum of weights assigned to all the models considered for sedimentary layer thickness (a), and Moho depth (b). This parameter may be seen as a proxy for information content, useful to identify relatively better-known *vs.* less-resolved areas (in brighter or darker shades of gray).

arithm of the sum of weights assigned to all models available at each grid point, for sedimentary layer thickness and Moho depth. This quantity may be seen as a proxy for information content, useful to identify relatively better-known and less-resolved areas. For each local model, we also use a cosine taper weight at the borders to flatten out the transition between models. Each data grid is then filtered using a Gaussian filter with 60 km half-width.

Several studies concentrate on modeling the depth of crustal discontinuities (Table 2) but specification of the values of seismic parameters is of course essential to characterize the crust for seismological use. Seismic parameters are not as well constrained as the depth of the interfaces. Information derives from laboratories and field experiments, and from refraction studies. Most original information refers to P-wave speed so, in each layer, we actually merge the different v_P models. We derive S-wave speed and density from scaling relations with respect to v_P (Brocher, 2005) derived from a Nafe-Drake curve regression. The so-called "Brocher's regression fit" is reliable for v_P between 1.5 and 8 km/s, that is the typical crustal velocity range. Below, we report the formulae we used:

$$\rho(g/cm^3) = 1.6612v_P - 0.4721v_P^2 + 0.0671v_P^3 - 0.0043v_P^4 + 0.000106v_P^5 \tag{2.1}$$

$$v_S(km/s) = 0.7858 - 1.2344v_P + 0.7949v_P^2 - 0.1238v_P^3 + 0.0064v_P^4 \tag{2.2}$$

In the upper and lower crust, most of the original information about v_P derives from CRUST2.0, EuCRUST-07, AsCRUST-08 and BARENTS50 (Table 2.2)

whereas in the sedimentary layer we follow a different approach described next. Sediments are characterized by low values of velocity and density, and especially when the thickness of basins becomes large, reliable information about seismic parameters becomes critical. For instance, the sedimentary layer has a strong influence on seismic wave propagation, such as recorded by surface wave dispersion curves. So, a reliable velocity structure of the sedimentary layer is crucial to characterize the seismic behaviour of the final model. Mooney et al. (1998), Ritzmann et al. (2007) and other authors divide the sedimentary coverage in "soft" and "hard" sediments to distinguish between unconsolidated (average v_P of 2.0-3.0 km/s) and consolidated sediments (average v_P of 4.0-5.3 km/s). In Europe, the total sediment thickness vary between 0 and 20 km and, looking at Table 2.2, it may appear that, while basin thickness is rather well constrained, the velocity structure is not. In our dataset, information about basin velocity structure can be found in the LM97 sediment maps and in the BARENTS50 model, but in the first, spatial resolution is low and, in the second, the covered region is small. We cannot just use the v_P value of the LM97 sediment map in each grid point of our sedimentary layer since we modified the thickness of the layer using other models. Improved information of the sediment properties can be derived from borehole data, seismic profiles (where the determination of v_P still presents difficulties), or laboratory experiments, but retrieving detailed information to locally calibrate the model is beyond the scope of the present study. To overcome this difficulty, that we face in the regions outside BARENTS50 (Figure 1), we derive an empirical relation between thickness (h) and v_P, based on the data found in the LM97 sediment map. With a polynomial regression fit of all the data points (Figure 2.3), we find the relation $v_P(h)$ that could be used to assign a velocity structure in the sedimentary layer. The v_P structure then should be scaled to v_S and ρ using the "Brocher regression fit" (Brocher, 2005).

Our final sediment elastic parameters could be function of the sediment thickness (in km) using the 3^{rd} degree polynomial relation:

$$v_P(km/s) = 2.2 + 0.23h - 0.006h^2 + 0.000059h^3 \tag{2.3}$$

This empirical relation between thickness and v_P however oversimplifies the assessment of sediment properties. Laske and Masters (1997) and Bassin et al. (2000) derived their models using an approach based on geological provinces, consisting of dividing the world crust in crustal types and assigning a 1D structure to each type. From Figure 2.3 it is clear that, for each value of thickness, there is a large variability in velocity due to local geology. In other words, for each geological setting, there is a curve describing average velocity as a function of thickness. As velocity increases with depth in a sedimentary layer, because of pressure and lithogenetic processes, depth-averaged velocity depends on total thickness. We want to keep, in our model, the geological information contained in LM97. We proceed as follows. We analyze v_P as a function of sediment thickness in LM97, and derive the range of v_P values reported in connection to each value of thickness. Then, for each grid point, we find the relative position, within this range, of its v_P as listed by LM97. For the same grid point, we finally associate to our new thickness the v_P value corresponding to

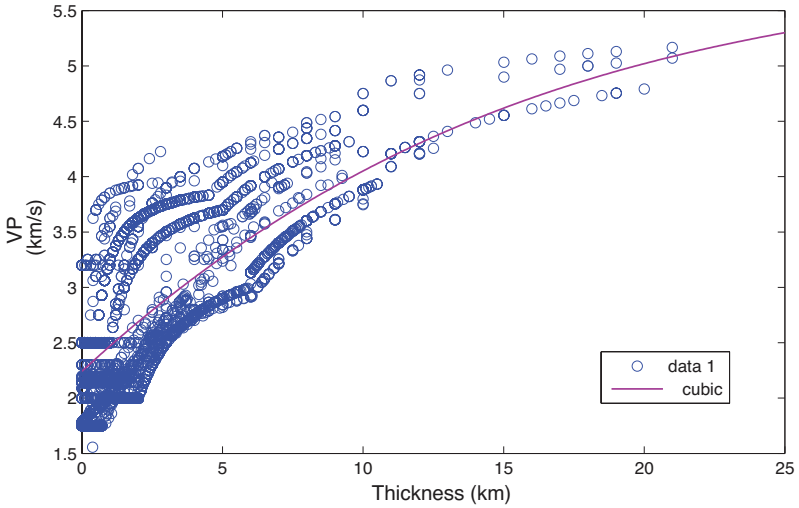

Figure 2.3: Average P-wave velocity in the sedimentary layer as a function of thickness from the LM97 sediment map (Laske and Masters, 1997) in the European area. The red line represents the cubic polinomial fit of all the data ($v_P = 2.2 + 0.23h - 0.006h^2 + 0.000059h^3$, v_P in km/s and h in km).

the same relative position, but within the range related to the new thickness. This transforms the thickness to a new value at some geographical location, but retaining its relative fast/slow nature — presumably connected to geological properties — of LM97. This method is illustrated by Figure 2.4, where for each point we plot an arrow starting from the original $v_P^{LM97}(h)$ and ending in the new $v_P^{EPcrust}(h_{EPcrust})$ (only 200 randomly selected points are shown on the graph for clarity).

P-wave velocity at the top of the mantle, representing the velocity of Pn waves, is useful for practical purposes, and often associated to crustal models. Only few of the models we collected actually contain such specification (CRUST2.0, BARENTS50). To associate Pn velocity to EPcrust, we deem thus more appropriate to include the results of a continental-wide inversion. EPmantle (Schivardi and Morelli, 2010) is a tomographic model of the upper mantle obtained by inversion of surface waves, using EPcrust as a priori contraint. EPcrust and EPmantle have been conceived as a coherent reference model for European earth structure. Since EPmantle is a v_S model, we calculate v_P from v_S using the scaling relation from Ritsema and Van Heijst (2002).

2.4 Results and discussion

The new Moho depth, sediment thickness and Conrad depth of the new EPcrust crustal reference model are shown in Figures 2.5a, 2.6a, 2.7a respectively. We re-

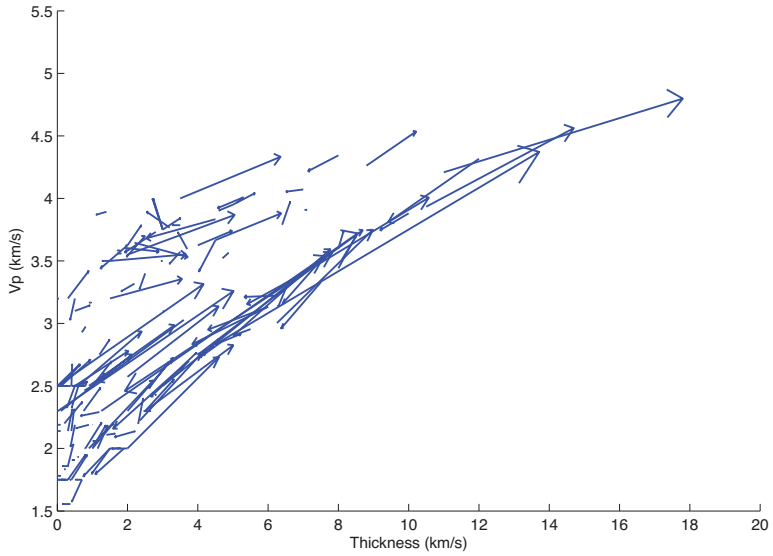

Figure 2.4: Comparison of average P-wave velocities in the sedimentary layer, as a function of thickness, from LM97 (open end of segments) to new values (arrow heads). Only 200 randomly selected points are shown on the graph for clarity. Each arrow represent how we adjust v_P to new layer thickness: start from the original $v_P^{LM97}(h)$ and end up with the new $v_P^{EPcrust}(h_{EPcrust})$.

call that parameterization is based on three layers, representing in turn sediments, upper crust and lower crust. Each layer has laterally-varying thickness and seismic parameters (P- and S-wave speed, density) and is uniform with depth. The working representation is gridline-based on a $0.1° \times 0.1°$ grid, but the distribution format is based on $0.5° \times 0.5°$ grid. Computed P-wave velocity for each layer is shown in Figure 2.8; v_S and ρ values are derived from the v_P structure using the Brocher relations (Brocher, 2005) as explained in the previous section. In the oceanic crust we found P-wave speed in the sedimentary layer within the range $1.5 < v_P < 2$ km/s, with the exception of the deep ocean basin (Barents basin, Cadiz, etc.) that have higher v_P $(4.5 - 5$ km/s). In the oceanic upper crust the velocity is between 5 and 6.5 km/s while in the lower crust we have $6.6 < v_P < 7.3$. In the continental crust we find v_P in the sediments between 2 and 5.3 km/s; in the upper crust we have $5.6 < v_P < 6.5$ and in the lower crust it is $6.6 < v_P < 7.3$. In the upper mantle, Pn velocity determined from Schivardi and Morelli (2010) is in the range from 7.8 to 8.2 km/s (Figure 2.8), typical values for this parameter. These values are in overall agreement with the well known crustal velocities found in the literature (Christensen and Mooney, 1995). The lateral resolution of the seismic parameters is limited by the resolution of the original dataset.

Our final model is a seismological description of the complex geological structure

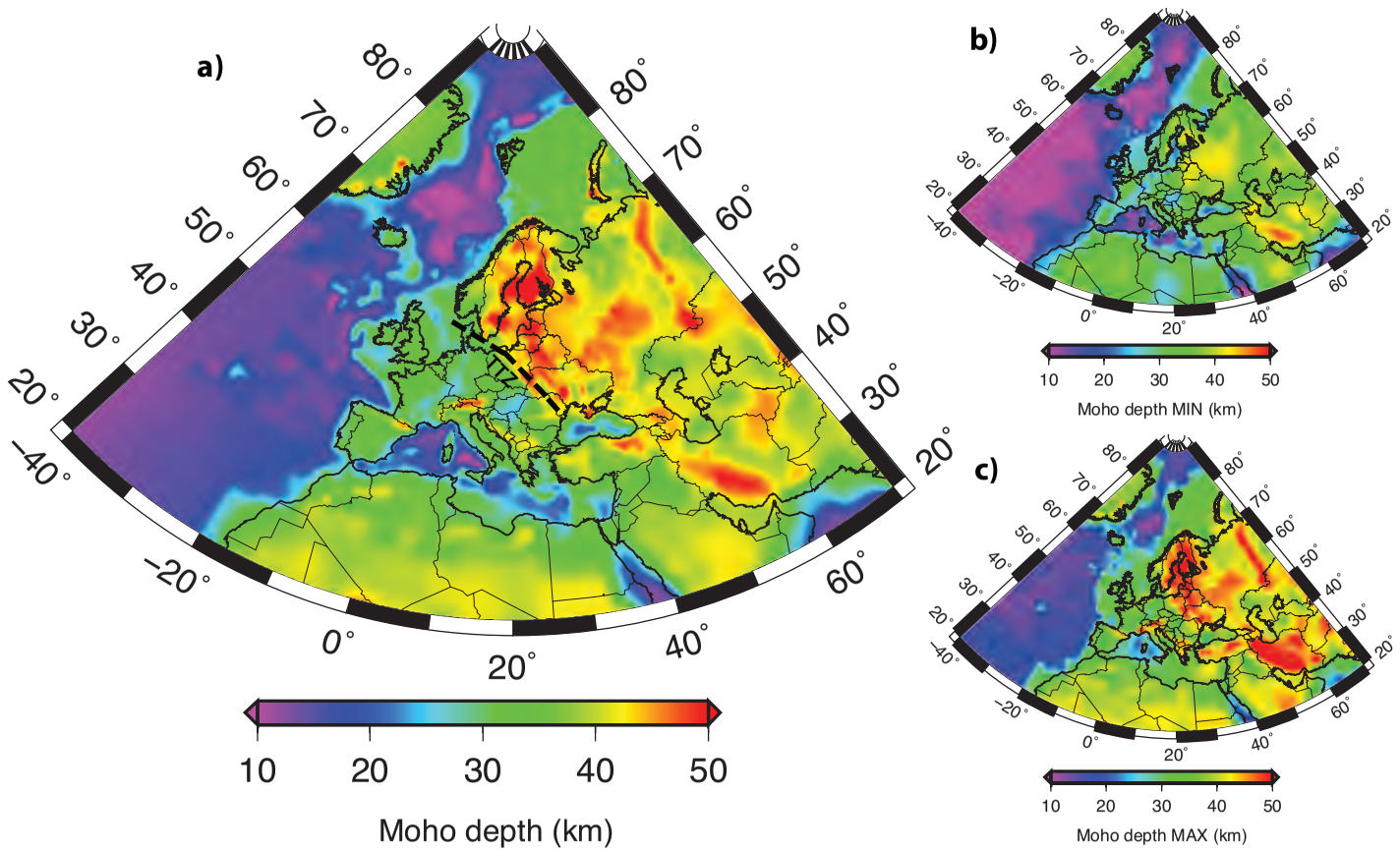

Figure 2.5: Moho depth (km) in EPcrust (a), compared to absolute minimum (b) and maximum (c) Moho depth in our dataset. The dashed black line in (a) represents the Tornquist-Teisseyre Zone (TTZ).

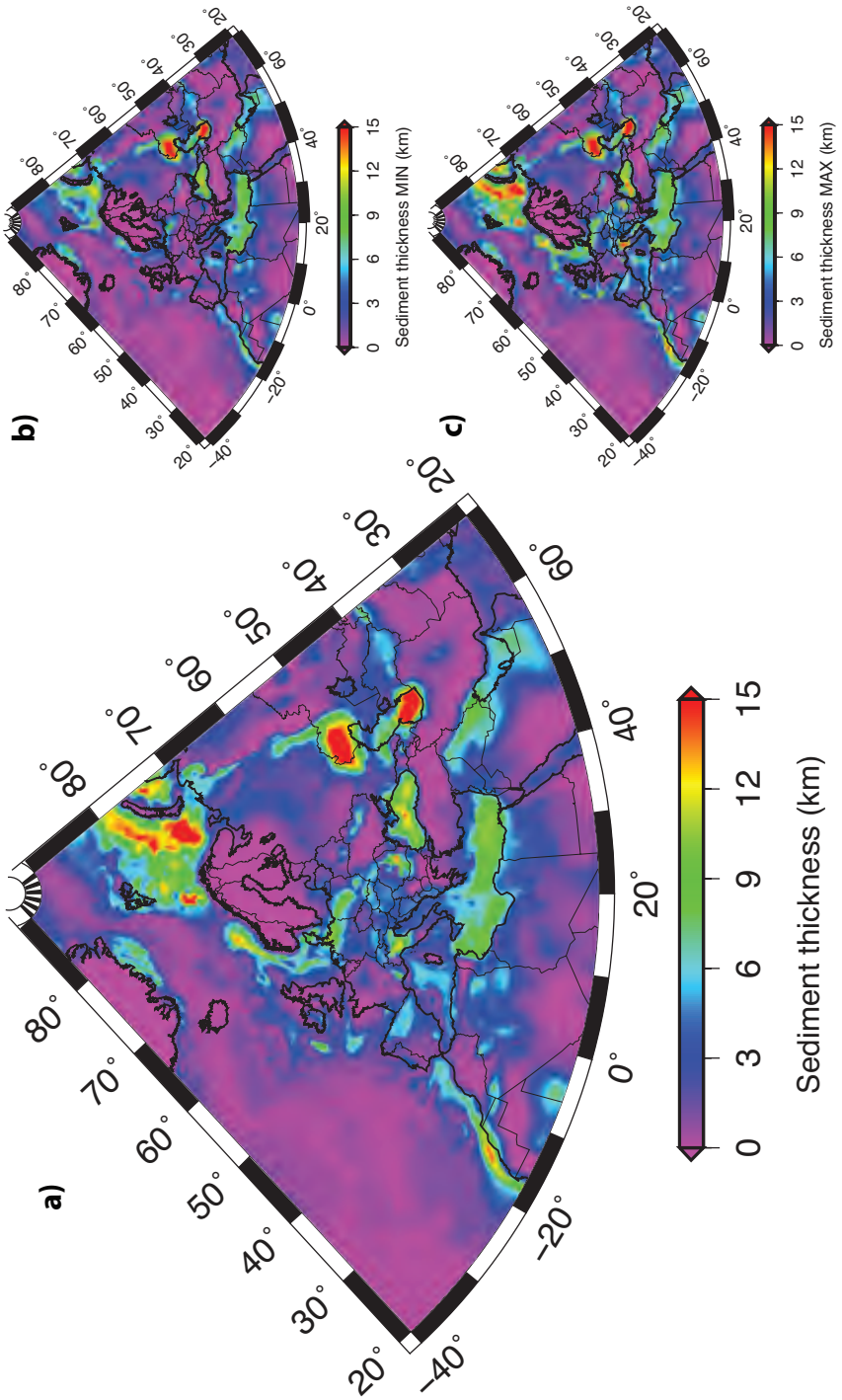

Figure 2.6: Sediment thickness (km) in EPcrust (a), compared to minimum (b) and maximum (c) sediment thickness in our dataset.

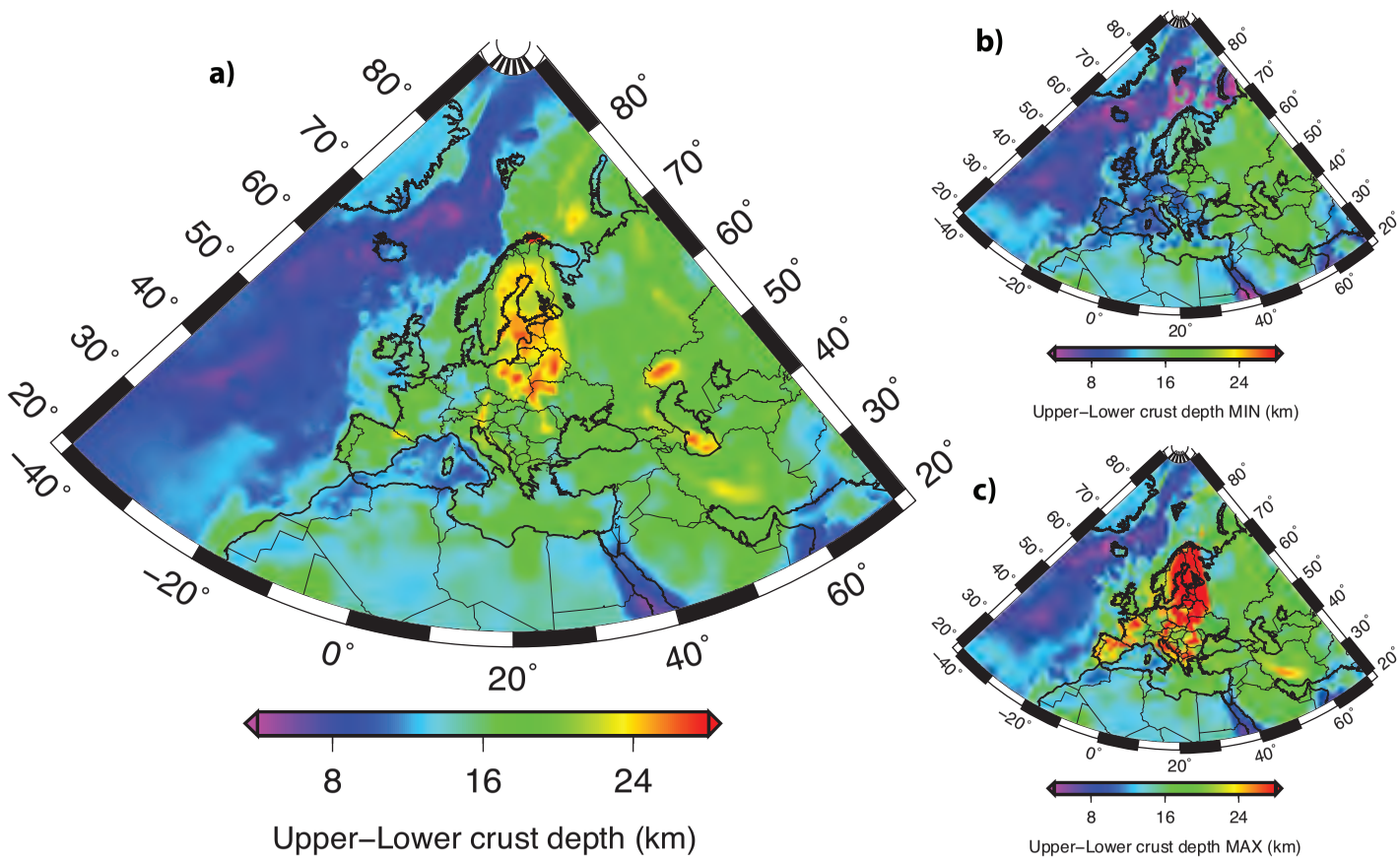

Figure 2.7: Depth of upper-lower crust discontinuity (km) in EPcrust (a), compared to minimum (b) and maximum (c) discontinuity depth in our dataset.

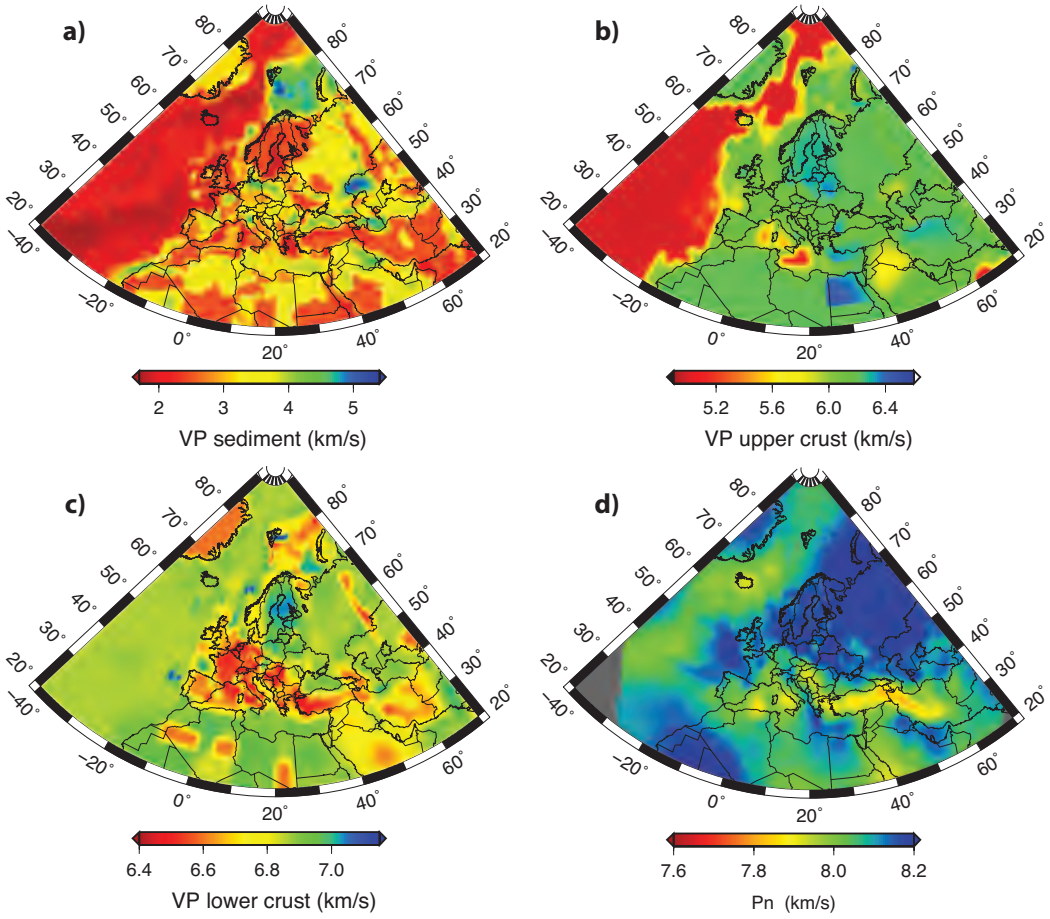

Figure 2.8: P-wave velocity in sediments (a), upper crust (b), lower crust (c) and uppermost mantle (Pn velocity, d).

of the European plate. Europe is composed by a large variety of tectonic structures ranging from Archean to Cenozoic. The Precambrian part (Artemieva et al., 2006) is formed by the East European craton (EEC) ranging from the Urals to the Carpathians, with the unique feature of the presence of a thick sedimentary cover over most of the platform, mainly of 2 to 4 km, but locally up to 20 km thick. The EEC has in general a flat surface topography (from 0 to 200 m) due to surface erosion since Precambrian (Artemieva, 2007) but it shows large undulations of the amplitude of the Moho topography (up to 30 km in variation, from 30 km to more than 60 km) and of the basement thickness (more than 20 km in variation) reflecting its complex tectonic history. The average Moho depth is about 45-50 km. In this region we find the deepest sedimentary basins, that share the common characteristics of a large thickness of the sedimentary cover, uplift of the Moho boundary (up to 36 km), and strong increase of the average velocity in the crystalline crust up to 6.5 km/s. They are the Dnieper-Donets Basin (a linear rift basin with a thickness of more than 10 km); the Peri-Caspian Basin, with thickness of more than 18 km (a cross-section is shown in Figure 2.9); the South Caspian Basin (thickness of 10-16 km) and the

Black Sea basin, 18 km thickness (Figure 2.10). In Figure 2.10b we compare a cross-section of EPcrust along the same profile as in Neprochnov and Ross (1978) (Figure 2.10a), where the authors review the information about crustal structure in the Black Sea. They found a 25-30 thick crust with a sediment layer of 20 km thickness, consisting of unconsolidated and consolidated sediments with velocity ranging from 3 to 5.5 km/s. Underneath this layer they put a lower crustal layer with high velocity (6.6-7 km/s), in good agreement with what we find in EPcrust both for depth and P velocity.
In Figure2.10-c we make a similar comparison, but in a section across the South Caspian Sea (Figure 2.10a) taken from Mangino and Priestley (1998). This study was obtained using results from receiver function studies and seismic reflection profiles and, for the consolidated and unconsolidated 16 km-thick sediments, they found $v_P < 4.8$ km/s; for the granitic crust v_P varies between 4.8 and 6 km/s, while for the basaltic (lower) crust v_P is between 6.4 and 7.4 km/s. These values are in good agreement with our final model, while Moho depth under the Caspian Sea is instead 10 km deeper in EPcrust.

In central-southern Europe, between the Tornquist-Teisseyre Zone (TTZ) — Figure 2.5 — and the Atlantic Ocean, we find a Paleozoic crust where crustal thickness changes very clearly with respect to the deeper East European craton. Moho depth averages at 30 km, with a maximum of 50 km beneath the Alps and the Pyrenees (two of the best constrained zones in our model), and a minimum of 8-10 km under the Tyrrhenian Sea. Some deep basins are also present in this region: the Po Plain basin, the Pannonian basin (see Figure 2.9) and the North-German Basin (4-6 km thickness).

In the Atlantic region Moho depth ranges from 8 km depth, near the Mid-Atlantic ridge, to 20 km in the ocean-continent transition zones. In the Barents Sea and along the continental margin near North Africa and the Norwegian coast, we find deep sedimentary basins with high velocity, in particular in the Barents basin where the local model BARENTS50 predicts $4.3 < V_P < 5.5$.
If we compare our model with CRUST2.0, we find variations in Moho depth up to ± 15 km. The main differences are in the North Atlantic region, along the continental margin and under the Alps, largely due to improved resolution of our model's Moho boundary. These features are all present in the original models, and their mapping is due to the use of more reliable and detailed datasets.

It is indeed difficult to estimate the uncertainties associated to the parameters of such a model, obtained form an assemblage of different kinds of informations, but it is nonetheless important to make an effort to evaluate them. Few of our constituent models provide an error estimate (Table 2.1), and a statistical evaluation of the variance of each parameters of the resulting model is impossible. However, considering that, our scheme allows for calculation of minimum and maximum values at each geographical point for each model parameter, we can define a range of variability of the different estimates at a specific location. For each grid point we generally have more than one value and, with our weighting scheme, we calculate

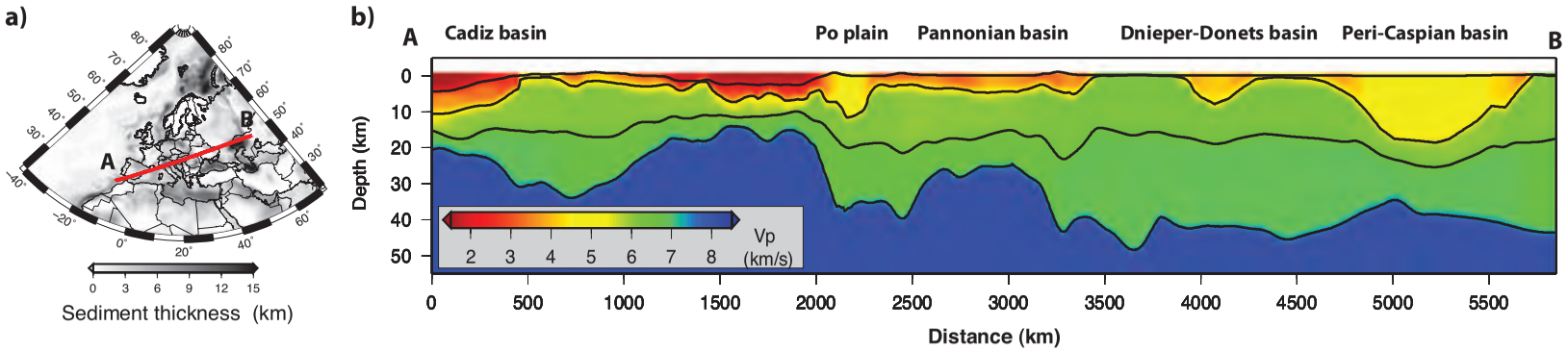

Figure 2.9: Cross-section of EPcrust (b) along the A-B profile (a). It is possible to recognize deep sedimentary basins, such as the Cadiz basin in the gulf of Cadiz (Spain), the Po plain in Northern Italy, the Pannonian and the Dnieper-Donets basins in Central-Eastern Europe, and the Peri-Caspian basin at the North of the Caspian Sea.

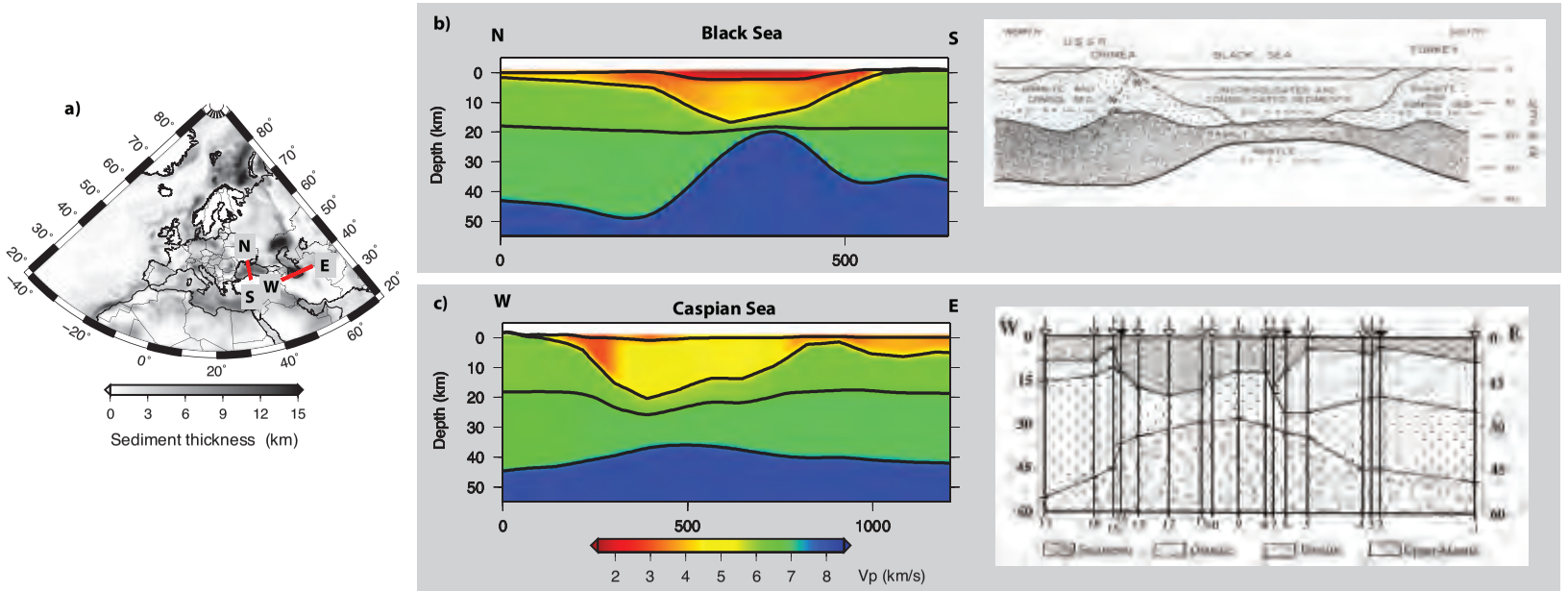

Figure 2.10: Comparison of two cross-sections of EPcrust along the N-S profile across the Black Sea (b) and W-E across the Caspian Sea (c) with corresponding profiles taken from Neprochnov and Ross (1978) and Mangino and Priestley (1998).

our best value that will lie between the minimum and the maximum values of the original dataset. In Figure 2.11b we plot the available data for the Moho depth and the final EPcrust Moho (dashed red line) along cross-section C-D (Figure 2.11a). In some locations the agreement between the different models is good, while in other regions we can have differences up to 10 km. This cross-section also reveals which are the regions with tighter constraints, and how large the variability could be in the estimations done in different models based on diverse data and approaches. Figure 2.5b,c, 2.6b,c, 2.7b,c, show maps with minimum and maximum values for each grid point. This is a way to represent the variability of the original information of each parameter, and to estimate the maximum variability of the resulting value. Unfortunately, where we have only one source of information, a zero range does not mean certainty.

2.5 Conclusions

We present a new crustal model of the European plate, EPcrust, based on critical assemblage of information and previous models of European crustal structure. EPcrust has some important advantages with respect to earlier models: *i)* it covers the whole European plate, *ii)* it is a complete and consistent model, with all the parameters provided, including for the sedimentary layer, *iii)* it incorporates most of the recent result concerning the European crust, *iv)* it is easy to update by adding new contribution, *v)* it is available in a digital format and *vi)* it is reproducible.

EPcrust is most suited for use at the broad European scale for a variety of research topics, including: wave propagation modeling at continental scale, crustal correction in tomography, gravity studies, dynamic topography inference and so on. It includes recent studies and it improves the knowledge of crustal properties at regional and continental scale. Recently, our model has been used as crustal correction in a surface wave tomography study to image the European upper mantel Schivardi and Morelli (2010). EPcrust, with respect to CRUST2.0, seems to improve the recovery of upper mantle structure at least in the area where it has a high resolution, such as in the Alps region. However, EPcrust also has some limits. In local studies (shake maps, seismic site response simulations), where a detailed knowledge of the crustal structure is required, this model will not be appropriate because of its low spatial resolution for such applications. Note however that, in the best constrained regions (Alps, Central Europe), EPcrust could be a good candidate for the representation of the crust, also at a smaller scale.

The sedimentary cover is a very important parameter to characterize the seismic response of a crustal model. Unfortunately, information on sedimentary thickness and v_P is not as detailed as one could desire, even at the scale we are working at. We made an effort to always use the most detailed information available about the thickness of the sedimentary cover, and had to make a plausible extrapolation to adjust v_P to the new depths where it was only available from global studies with lower detail.

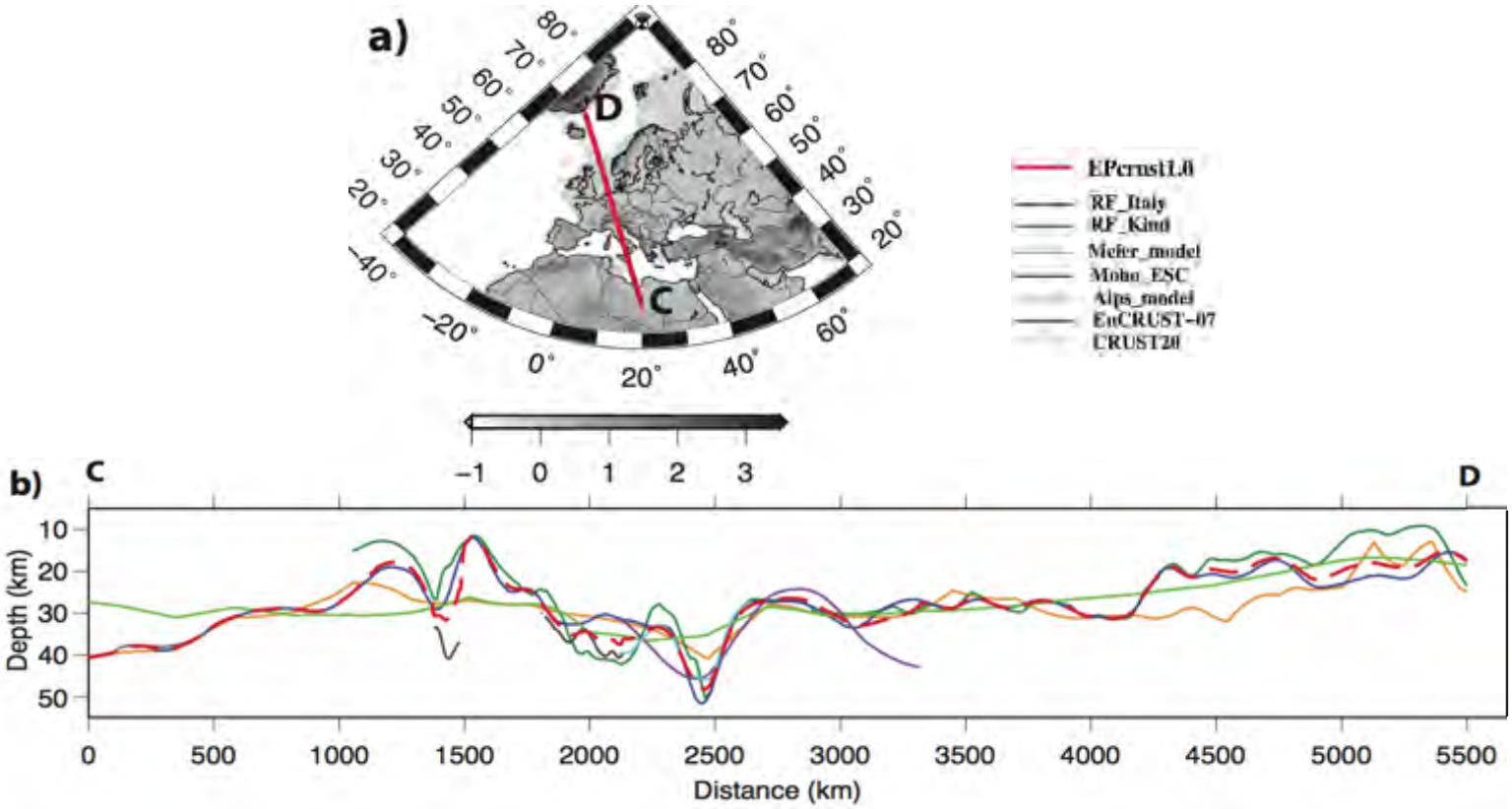

Figure 2.11: Moho variability along the cross-section C-D. The red dashed line shows Moho depth in EPcrust. The CRUST2.0 and Meier Moho depths are plotted interpolating values between adjacent grid points to avoid steps (a faithful visualization should be a staircase).

The interface between upper and lower crust is often considered quite a controversial boundary: it is difficult to find reliable information about it, even from active source studies, as the velocity gap is smaller than the one at the Moho. We nonetheless include such a differentiation within the crystalline crust, following, for instance, EuCRUST-07 (Tesauro et al., 2008). This choice enables comparisons, and makes up for a simplified but still realistic representation. In EPcrust, upper and lower crust always have non-zero layer thickness, and their interface is always smoother than other boundaries.

A further improvement of EPcrust could be addressed including new, more refined and higher resolution models resulting from, e.g., seismic noise studies, new refraction-reflection seismic experiments or receiver function results. We plan to do this in the future, as new high-quality descriptions of the European crust become available. Although it is not realistic to aim at an improvement in the whole, broad, region, at least the best instrumented areas will presumably see improvements in the near future.

EPcrust is available on *http://www.bo.ingv.it/eurorem/EPcrust*. The distribution format is based on the TomoJSON data exchange format described by Postpischl et al. (2010). In order to make the final model reproducible we also provide, on the website, all the individual contributions used to assembly EPcrust, to create a database for crustal structure in Europe. We plan to update this resource in the future as new local models and datasets will become available.

References

Amante, C., Eakins, B.W., 2009. ETOPO1 1 Arc-Minute Global Relief Model: Procedures, Data Sources and Analysis. NOAA Technical Memorandum NESDIS NGDC-24 p. 19.

Artemieva, I.M., 2007. Dynamic topography of the East European craton: Shedding light upon lithospheric structure, composition and mantle dynamics. Global Planet. Change 58(1), 411–434.

Artemieva, I.M., Thybo, H., Kaban, M.K., 2006. Deep Europe today; geophysical synthesis of the upper mantle structure and lithospheric processes over 3.5 Ga. Memoirs of the Geological Society of London 32, 11–41.

Baranov, A., 2010. A new crustal model for central and southern Asia. Izv-Phys. Solid Earth 46(1), 34–46. doi:10.1134/S1069351310010039.

Bassin, C., Laske, G., Masters, G., 2000. The current limits of resolution for surface wave tomography in North America. Eos Trans. AGU 81, 48.

Bisio, L., Giovambattista, R.D., Milano, G., Chiarabba, C., 2004. Three-dimensional earthquake locations and upper crustal structure of the Sannio-Matese region; Southern Italy. Tectonophysics 385(1-4), 121–136.

Bozdag, E., Trampert, J., 2008. On crustal corrections in surface wave tomography. Geophys. J. Int. 172(3), 1066–1082. doi:10.1111/j.1365-246X.2007.03690.x.

Brocher, T.M., 2005. Empirical relations between elastic wavespeeds and density in the Earth's crust. Bull. Seis. Soc. Am. 95(6), 2081–2092.

Capdeville, Y., Marigo, J., 2008. Shallow layer correction for Spectral Element like methods. Geophys. J. Int. 172(3), 1135–1150. doi:10.1111/j.1365-246X.2007.03703.x.

Christensen, N.I., Mooney, W.D., 1995. Seismic velocity structure and composition of the continental crust; a global view. J. Geophys. Res. 100(B6), 9761–9788.

Diaz, J., Gallart, J., 2009. Crustal structure beneath the Iberian peninsula and surrounding waters; a new compilation of deep seismic sounding results. Phys. Earth Planet. Inter. 173(1-2), 181–190.

Divins, D.L., 2003. NGDC Total Sediment Thickness of the World's Oceans and Marginal Seas. Retrieved date goes here, http://www.ngdc.noaa.gov/mgg/sedthick/sedthick.html .

Du, Z.J., Michelini, A., Panza, G.F., 1998. EurID: a regionalized 3-D seismological model of Europe. Phys. Earth Planet. Inter. 106(1-2), 31–62. doi:10.1016/S0031-9201(97)00107-6.

Faccenna, C., Becker, T.W., 2010. Shaping mobile belts by small-scale convection. Nature 465(7298), 602–605. doi:10.1038/nature09064.

Fichtner, A., Igel, H., 2008. Efficient numerical surface wave propagation through the optimization of discrete crustal models-a technique based on non-linear dispersion curve matching (DCM). Geophys. J. Int. 173(2), 519–533. doi:10.1111/j.1365-246X.2008.03746.x.

Geissler, W.H., Kind, R., Yuan, X., 2008. Upper mantle and lithospheric heterogeneities in Central and Eastern Europe as observed by teleseismic receiver functions. Geophys. J. Int. 174(1), 351–376.

Grad, M., Spicak, A., Keller, G.R., Guterch, A., Broz, M., Hegedus, E., Behm, M., Bodoky, T., Brinkmann, R., Brueckl, E., Czuba, W., Fancsik, T., Forkmann, B., Fort, M., Gaczynski, E., Geissler, W.H., Greschke, R., Harder, S.H., Hemmann, A., Hrubcova, P., Janik, T., Jentzsch, G., Kaip, G., Komminaho, K., Korn, M., Karousova, O., Majdanski, M., Malek, J., Malinowski, M., Miller, K.C., Rumpfhuber, E.M., Sroda, P., Takacs, E., Tiira, T., Vozar, J., Wilde-Piorko, M., Yliniemi, J., Zelazniewicz, A., 2003. SUDETES 2003 seismic experiment. Studia Geophysica et Geodetica 47(3), 681–689.

Grad, M., Tiira, T., Group, E.W., 2009. The moho depth map of the European Plate. Geophys. J. Int. 176(1), 279–292. doi:10.1111/j.1365-246X.2008.03919.x.

Guterch, A., Grad, M., Keller, G.R., Anonymous, 2005. Lithospheric structure beneath Central Europe from the POLONAISE'97, CELEBRATION 2000, ALP 2002, and SUDETES 2003 seismic refraction experiments. Eos Trans. AGU 86(52, Suppl.), Abstract S22A–01.

Guterch, A., Grad, M., Keller, G.R., Posgay, K., Vozar, J., Spicak, A., Brueckl, E., Hajnal, Z., Thybo, H., Selvi, O., Acevedo, S., Aric, K., Asudeh, I., Belinsky, A.A., Bodoky, T., Chwatal, W., Clowes, R., Czuba, W., Fancsik, T., Gaczynski, E., Harder, S.H., Hegedus, E., Hrubcova, P., Janik, T., Jentzsch, G., Joergensen, P., Kaip, G., Keller, G.R., Komminaho, K., Kostiuchenko, S.L., Kracke, D., Kohlbeck, F., Miller, K.C., Morozov,

A.F., Snelson, C.M., Sroda, P., Takacs, E., Tiira, T., Wilde-Piorko, M., Yliniemi, J., 2003. CELEBRATION 2000 seismic experiment. Studia Geophysica et Geodetica 47(3), 659–669.

Kind, R., 2009. Moho depth in central europe from receiver functions studies. Personal communications .

Kumar, P., Kind, R., Priestley, K., Dahl-Jensen, T., 2007. Crustal structure of Iceland and Greenland from receiver function studies. J. Geophys. Res. 112(B3), B03301.

Laske, G., Masters, G., 1997. A Global Digital Map of Sediment Thickness. Eos Trans. AGU 78, F483.

Mangino, S., Priestley, K., 1998. The crustal structure of the southern caspian region. Geophys. J. Int. 133(3), 630–648. doi:10.1046/j.1365-246X.1998.00520.x.

Meier, U., Curtis, A., Trampert, J., 2007. Global crustal thickness from neural network inversion of surface wave data. Geophys. J. Int. 169(2), 706–722.

Molinari, I., Kaeser, M., Morelli, A., 2010a. Analysis of different discrete representations of European crust for numerical wave propagation simulations. Geophysical Research Abstracts 12, EGU2010–4082.

Molinari, I., Morelli, A., 2009. Representation of crustal structures and surface-wave modeling. Geophysical Research Abstracts 11, EGU2009–10091.

Molinari, I., Morelli, A., Raileanu, V., Tataru, D., 2010b. The crustal structure of South-Eastern Europe in the new European Plate reference model. Geophysical Research Abstracts 12, EGU2010–8366.

Mooney, W.D., Laske, G., Masters, T.G., 1998. CRUST5.1: a global crustal model at 5 degrees x 5 degrees. J. Geophys. Res. Solid Earth 103(B1), 727–747.

Nataf, H., Ricard, Y., 1996. 3SMAC: an a priori tomographic model of the upper mantle based on geophysical modeling. Phys. Earth Planet. Inter. 95(1-2), 101–122. doi:10.1016/0031-9201(95)03105-7.

Neprochnov, Y.P., Ross, D.A., 1978. Black Sea geophysical framework. Initial Reports of the Deep Sea Drilling Project 42, Part 2, 1043–1055.

Pasyanos, M.E., Walter, W.R., Flanagan, M.P., Goldstein, P., Bhattacharyya, J., 2004. Building and testing an a prioriGeophysical model for western Eurasia and north Africa. Pure Appl. Geophys. 161(2), 235–281. doi:10.1007/s00024-003-2438-5.

Piana Agostinetti, N., Amato, A., 2009. Moho depth and Vp/Vs ratio in peninsular italy from teleseismic receiver functions. J. Geophys. Res. 114, 17 PP.. doi:200910.1029/2008JB005899.

Pondrelli, S., Salimbeni, S., Morelli, A., EkstrÃ¶m, G., Boschi, E., 2007. European-Mediterranean regional centroid moment tensor catalog: Solutions for years 2003 and 2004. Phys. Earth Planet. Inter. 164(1-2), 90–112. doi:10.1016/j.pepi.2007.05.004.

Postpischl, L., Danecek, P., Morelli, A., Pondrelli, S., 2010. Standardization of seismic tomographic models and earthquake focal mechanisms data sets based on web technologies, visualization with keyhole markup language. Computers & Geosciences In Press, Corrected Proof, –. doi:DOI:10.1016/j.cageo.2010.05.006.

Remy, N., Bouchera, A., Wu, J., 2009. Applied Geostatistics with SGeMS: A User's Guide. Cambridge University Press.

Ritsema, J., van Heijst, H.J., Woodhouse, J.H., Deuss, A., 2009. Long-period body wave traveltimes through the crust: implication for crustal corrections and seismic tomography. Geophys. J. Int. 179(2), 1255–1261. doi:10.1111/j.1365-246X.2009.04365.x.

Ritsema, J., Van Heijst, H., 2002. Constraints on the correlation of p- and s-wave velocity heterogeneity in the mantle from p, PP, PPP and PKPab traveltimes. Geophys. J. Int. 149(2), 482–489.

Ritzmann, O., Maercklin, N., Faleide, J.I., Bungum, H., Mooney, W.D., Detweiler, S.T., 2007. A three-dimensional geophysical model of the crust in the Barents Sea region; model construction and basement characterization. Geophys. J. Int. 170(1), 417–435.

Schivardi, R., Morelli, A., 2009. Surface wave tomography in the European and Mediterranean region. Geophys. J. Int. 177(3), 1050–1066. doi:10.1111/j.1365-246X.2009.04100.x.

Schivardi, R., Morelli, A., 2010. EPmantle: a three-dimensional transversely isotropic model of the upper mantle under the European Plate. Submitted to Geophys. J. Int. .

Stehly, L., Fry, B., Campillo, M., Shapiro, N.M., Guilbert, J., Boschi, L., Giardini, D., 2009. Tomography of the Alpine region from observations of seismic ambient noise. Geophys. J. Int. 178(1), 338–350. doi:10.1111/j.1365-246X.2009.04132.x.

Stratford, W., Thybo, H., Faleide, J.I., Olesen, O., Tryggvason, A., 2009. New moho map for onshore southern norway. Geophys. J. Int. 178(3), 1755–1765. doi:10.1111/j.1365-246X.2009.04240.x.

Tesauro, M., Kaban, M.K., Cloetingh, S.A.P.L., 2008. EuCRUST-07: a new reference model for the European crust. Geophys. Res. Lett. 35, L05313. doi:10.1029/2007GL032244.

Wessel, P., Smith, W.H.F., 1998. New, improved version of the Generic Mapping Tools released. Eos Trans. AGU 79, 579.

Wilde-Piorko, M., Geissler, W.H., Plomerova, J., Grad, M., Babuska, V., Brueckl, E., Cyziene, J., Czuba, W., England, R., Gaczyski*, E., Gazdova*, R., Gregersen*, S., Guterch*, A., Hanka*, W., Hegeds*, E., Heuer*, B., Jedlicka*, P., Lazauskiene*, J., Keller*, G., Kind, R., Klinge, K., Kolinsky, P., Komminaho, K., Kozlovskaya, E., Krueger, F., Larsen, T., Majdaski, M., Malek, J., Motuza, G., Novotny, O., Pietrasiak, R., Plenefisch, T., Rzek, B., Sliaupa, S., roda, P., wieczak, M., Tiira, T., Voss, P., Wiejacz, P., 2008. PASSEQ 2006-2008: Passive seismic experiment in Trans-European suture zone. Stud. Geophys. Geod. 52(3), 439–448.

Yegorova, T.P., Starostenko, V.I., 2002. Lithosphere structure of european sedimentary basins from regional three-dimensional gravity modelling. Tectonophysics 346(1-2), 5–21.

Chapter 3

A crustal model of South Central and Eastern Europe

Contents

3.1 Introduction

An accurate knowledge of the structure of the crust of the earth — besides being of course necessary to know the geological structure of any specific region — is also indispensable for geophysical modeling, in fields ranging from geodynamics (Kaban et al., 2010; Faccenna and Becker, 2010) to seismology (Levshin and Ritzwoller, 2002; Somerville and Moriwaki, 2003; Kawase, 2003). Regional, or continental, scale models of the crust are thus used to simulate, e.g., seismic wave propagation at large distances, and to account for shallow structure when imaging upper mantle structure (e.g. Schivardi and Morelli, 2011).

At global and continental scale, many models are available, such as CRUST2.0 (Bassin et al., 2000), EuCRUST-07 (Tesauro et al., 2008), European Moho depth published by Grad et al. (2009b) and the most recent EPcrust (Molinari and Morelli, 2011). These models were previously described and for any comments and descriptions see Chapter 2 of this thesis.

New, or improved, local models are a requisite for improving such large-scale compilations of data about the structure of the European crust, especially from areas where less-detailed information has been contributed. In fact, three-dimensional representations of a geographical district constitute the intermediate step needed to go from specific, 'ground-truth', information — along profiles, relatively to active-source experiments, or point-wise, such as receiver-function determinations — to

Submitted at Pure and Applied Geophysics as: Molinari I, V. Raileanu and Morelli A. – *"A crustal model of South Central and Eastern Europe"*. 2011.

a continental-scale model. For this reason, we thought important to focus our attention specifically on the region covering the Eastern Alps sector, Carpathian-Pannonian province — comprising orogene, platform and basin structures in Hungary and Romania — Black Sea, Balkan area (Bulgaria, Greece and Turkey) and the western margin of the East European Platform (Ukraine).

In this work, we primarily focus our attention on a section with a relatively high density of information — the broad Eastern Alps province, an important area from a tectonic point of view since it covers the collision zone between European, Adriatic and Pannonian plates (around 47° N and 14° E). This region has been the target of many seismic experiments — e.g., POLONAISE'97 (Guterch et al., 1999), CELEBRATION2000 (Guterch et al., 2003; Sroda et al., 2006), ALP 2002 (Brueckl et al., 2003), SUDETES 2003 (Grad et al., 2003b). Despite its geophysical importance, we did not find any comprehensive three-dimensional crustal model for this province. To fill this gap, we wish to create a continuous local crustal model (EA1.0) by applying geostatistical interpolation methods (outlined in Section 3.3) to 15 profiles criss-crossing this area. Other similar studies had been done in this target region (Grad et al., 2009a) but they do not provide a complete seismic crustal model. The new model will be parameterized in three layers, and include depth of interfaces, v_P, v_S and density in each layer. The resulting model should be directly usable, for instance, for more accurate numerical simulation of seismic wave propagation, or crustal correction in mantle tomography. With a number of profiles located outside the East Alps region, in addition to data from receiver functions by Sodoudi et al. (2006) and using EPcrust Moho maps as a background, we also aim to create a new Moho map for the South-Central and Eastern Europe (from 11°E to 42°E and from 34°N to 52°N). Due to the location of available data, the new map will be better defined in the Eastern Alps and the Aegean sectors, to be considered as an improvement with respect to previous models. The paper is structured as follows. We first describe the dataset used, then we outline the method followed to build the maps, and finally present and discuss the complete crustal model for the East Alps region (EA1.0) followed by the new Moho maps of the South Central and Eastern Europe as an update to the EPcrust model.

3.2 Seismic lines in the study area

A quick look across Europe shows unequal distribution of crustal seismic investigations carried on in the last 4 or 5 decades. While Central Europe benefited from many active-source seismic experiments, resulting in a dense network of prospection lines, we may note a small number of seismic lines, reaching quite low density — or even absence — in districts on the periphery of the continent. We set our study perimeter between 12°E and 43°E, and from 34°N to 52°N, as shown in Figure 1. In such a region we encounter a wide diversity of types of tectonic units, ranging from platform (e.g. East European and Moesian) to orogen(e.g. from Alps and Carpathians to Dinarides and Hellenides) and basin (e.g. Pannonian), with variable

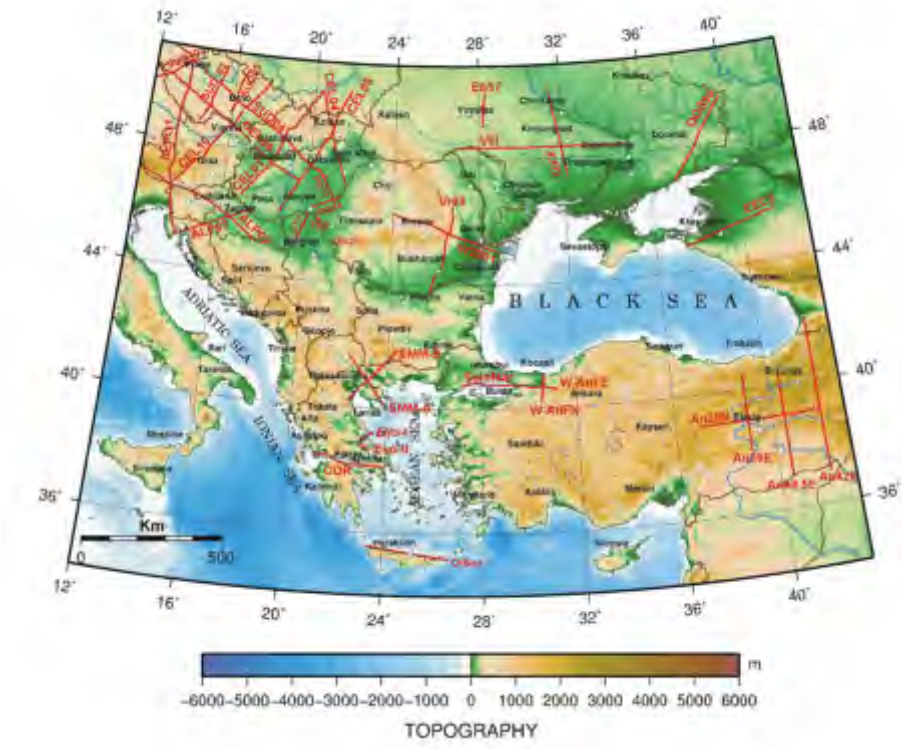

Figure 3.1: Location of the crustal seismic lines (red) used for testing of the EPCrust model on the background of the Geographic map of the Central and South East Europe.

crustal features. This is conceivably a rather complex and heterogeneous zone, but its knowledge has not been pursued with great detail. The area is only partially included in EuCRUST-07 (Tesauro et al., 2008) for its north-westernmost portion. The southern and eastern margins are included in the Moho map by Grad et al. (2009b) and in Baranov (2010). This is not one of the best-constrained portions of continental reference EPcrust, especially for the description of seismic parameters and the sedimentary layer. It is sensible, then, to search and extract all possible information from the literature, considering the seismic refraction/reflection profiles that have been shot, and whose results are published in the literature.

An inventory of the crustal seismic lines across the studied region resulted in a list of tens of lines. We selected crustal lines, by taking into account both data quality (well defined crustal interfaces and P-wave velocity information across the whole section) and availability of geographic coordinates. In areas with older and newer seismic lines only data collected in the last decades were selected. Altogether, 37 crustal seismic sections were finally selected from the Anatolian Plate and Cretan Sea in South to the Ukrainian Shield in NE and the Bohemian Massif and Alps in NW, Figure 3.1. The location of these seismic lines has been the first step in preparing data for model assembling. The geo-referencing has been based either on the geographic coordinates of the shot points published in the papers (as it has

been the case for most of the seismic lines from Central Europe) or on coordinates inferred from the maps or sketches published along with the seismic lines. Many of the selected seismic lines had no explicit mention to geographic coordinates in the articles, a circumstance that sometimes imposed recovery of coordinates by graphic methods, using different ad-hoc techniques ranging from digital on-line Google maps and map software, to the direct graphical measurements on the maps or sketches published by authors. The coordinate-recovery techniques involved quite a time-consuming and tedious work in the process to locate the seismic lines.

The following step consisted of a quality analysis of seismic sections and identification of main interfaces — base of sediments/top of crystalline basement (B), base of upper crust/top of lower crust (C) and base of crust or Moho (M). Then the crustal sections have been sampled to 1D models spaced every 50 km or so, starting from each shot-point from the northern or western end to the opposite end. Suites of 1D models at 0, 50, 100, 150, ... km distance from one end of each line have thus been extracted. Whenever the shot points have an average spacing less than about 50 km, they have been used as reference points for the 1D sections. Each 1D model consist of the same kind of interfaces as EPcrust: ground surface, B, C and M interfaces. The accuracy of depth readings on the crustal sections has been better than 0.5 km for all interfaces. For each of the upper and lower crustal layer, a mean seismic velocity has been assigned as a weighted average of seismic velocities of the sub-layers which compounded each major layer. The accuracy of the computed mean seismic velocities has been less than 0.05 km/s. For the upper crustal stack (upper crystalline crust and middle crust) a range of P-wave seismic velocities ranging from 5.8 km/s to 6.8 km/s has been allocated, while for the lower crustal stack the range from 6.7 km/s to 7.5 km/s has been used (Pavlenkova, 1988; Christensen and Mooney, 1995; Avendonk et al., 2006).

For each seismic line a table with data on interface depths and P-wave velocities has been constructed. Each row of the table defines a 1D model, showing the relevant parameters: distance in km from the reference end of seismic line or the shot number, longitude and latitude of the point, elevation of ground (minus sign above sea level), depth from sea level to the top of the crystalline basement, top of the lower crust and Moho, mean P-wave seismic velocities in the sedimentary cover, upper and lower crust and top of upper mantle as well as the crossing points where the seismic line is cutting other seismic lines used in study. In addition, the table displays the region where each line is located and pertinent references. This kind of data has been assembled for each seismic line in at least 4 points for shorter lines ($<$ 150-200 km) and 10 or more points for longer lines. In the crossing points of two seismic lines not always the depths at interfaces and velocities were coincident. Whenever a difference larger than 0.5 km for depths and larger than 0.1 km/s for velocities has been encountered, an average of the pair values has been assigned to the both seismic lines.

Figure 3.2 shows the sample Vrancea 2001 seismic section, with the shot points where 1D models were sampled. In the Table 3.1 the main crustal parameters, as described above, are listed.

Table 3.1: Seismic parameters extracted from SUD03 seismic lines

Shot point	Lon	Lat	Topography	sediment depth (km)	v_P sedi (km/s)	Conrad depth (km)	v_P UC (km/s)	Moho (km)	v_P LC (km/s)	P_n (km/s)	crossing line
42010	14,48	48,73	-0,550	-0,45	4	19	6,05	36	6,65	7,93	
42020	14,92	49,25	-0,44	-0,34	4	19	6,05	36	6,7	7,93	CEL09
42030	14,95	49,5	-0,550	-0,46	4	19,5	6,05	33	6,7	7,93	
44080	15,08	50	-0,23	0,18	3,9	19,5	6,05	30,5	6,7	7,93	SUD04
42050	15,56	50,54	-0,41	0,95	3,8	21	6,05	30,5	6,7	7,93	

Table 3.2: Seismic lines selected in this work

Profile name	Reference
ALP01	Behm et al. (2007)
ALP02	Brueckl et al. (2003)
ALP07	Sumanovac et al. (2009), Sumanovac (2010)
SUD01	Grad et al. (2008), Ruzek et al. (2007)
SUD02	Majdanski et al. (2006)
SUD03	Grad et al. (2003b), Ruzek et al. (2007)
SUD04	Grad et al. (2003b), Hrubcova et al. (2010)
CEL01	Sroda et al. (2005)
CEL04	Guterch and Grad (2006), Guterch et al. (2003)
CEL05	Grad et al. (2006a)
CEL09	Ruzek et al. (2007), Hrubcova et al. (2005)
CEL10/ALP04	Hrubcová and Sroda (2008), Grad et al. (2009a)
PGT1 & PGT4	Posgay et al., 1995, 1996, Meszaros and Zilahi-Sebess (2001)
GTII	Posgay et al, 1988, Marcovic et al., 2002
TER & MOR	Raileanu et al. (1994), Meszaros and Zilahi-Sebess (2001)

Table 3.3: Seismic lines selected in this work

Profile name	Reference
Eb97	Thybo et al. (2003)
VIII & XXIV	Grad et al. (2006b) and Grad and Tripolsky (1995)
DOB99	Grad et al. (2003a)
EEC3	Kostyucenco et al.(2004)
VR99	Hauser et al. (2001)
VR2001	Hauser et al. (2007)
SMM-A	Papazachos (1998)
SMM-B	Papazachos (1998)
Evo-I & Evo-II	Makris et al. (2001)
COR	Zelt et al. (2005)
CrSea	Makris and Yegorova (2006)
SeisMar	Bécel et al. (2009)
W-AnFN- & W-AnFE	Karahan et al. (2001)
An42E, An39E	Angus et al. (2006)
An40.5E, An39N	Angus et al. (2006)

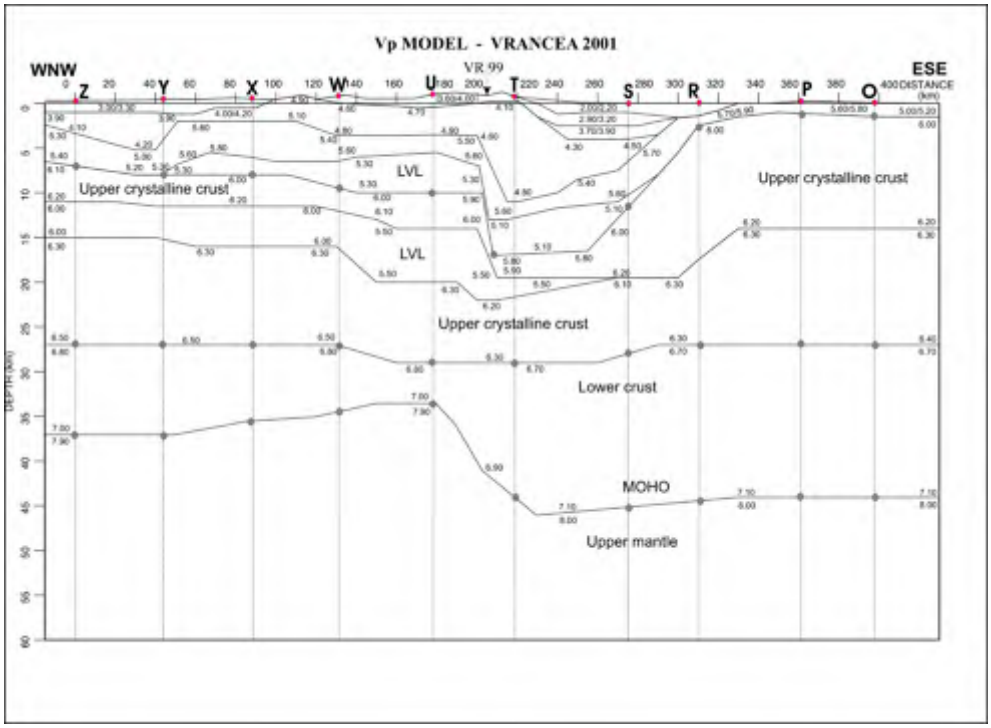

Figure 3.2: An example of sampling of 1D crustal models from the crustal section of Vrancea 2001 seismic line. Letters from O-Z in the upper part of section are the shot points; numbers with 2 digits are P-wave velocities in km/s. Grey points mark the depths where shot points projections cross the basement, top of lower crust and Moho. Vr99 is the crossing point with the Vrancea 99 seismic line. LVL- Low Velocity Level

Altogether we selected and processed 38 seismic lines (Tables 3.2, 3.3) located in Greece, Turkey, Romania, Ukraine, Russia, Poland, Hungary, Slovakia, Austria, Czech Republic, Slovenia, Croatia and Serbia. Looking at the geographical distribution (Figure 3.1), we can divide the lines into 2 groups, based on a line-density criterion. The first group — Table 3.2 — comprises the lines (15 in all) from the most important seismic experiments (such as ALP2000, CELEBRATION2000, SUDETES2003). In particular we selected: the ALP01, ALP02, ALP04, and ALP07 sections that cover the Bohemian Massif, Molasse basin, Southern and Central Alps and Dinarides; the southern segments of SUD01, SUD02 and SUD03, and SUD04 crossing the Bohemian massif, Sudetes Mountains, Western Carpathians and Pannonian basin; the southern segment of CELEBRATION seismic lines crossing from North to South the Western Carpathians (CEL01, CEL04 and CEL05) and the Eastern Alps (CEL10/ALP04), and from West to East the Bohemian massif to the Pannonian Basin (CEL09); some seismic refraction/reflection lines located in the Pannonian basin —such as PGT1 and PGT4, TER, MOR and GTII. See Table 3.2 for references. Using this set of about 140 1D models resulting from sampling 15 seismic lines, we can build a local crustal model with the parameters listed above: depth to top of basement, top of lower crust and Moho, and P-wave velocities in sed-

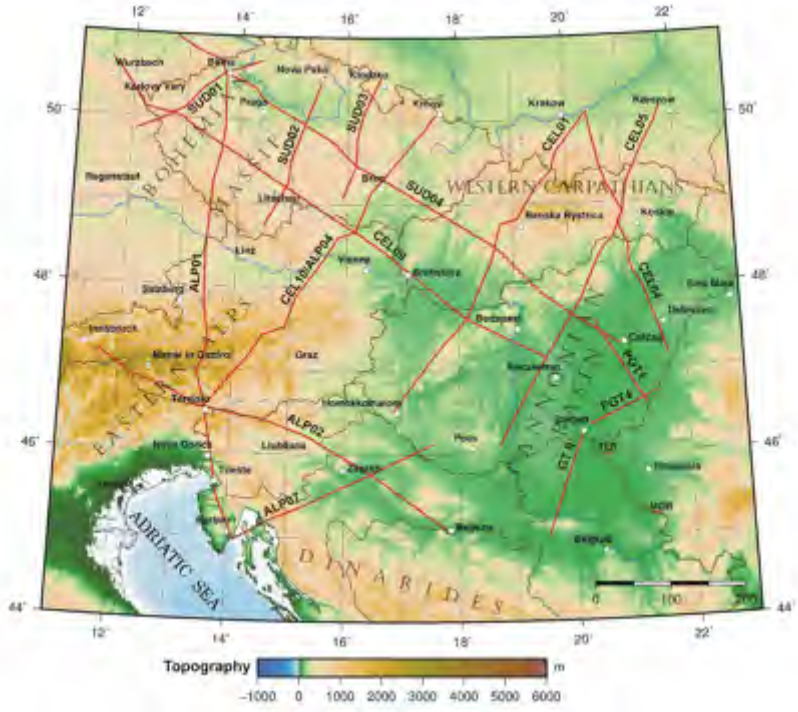

Figure 3.3: The seismic line network used for a more detailed testing of the EPCrust in the the South-Central Europe. On the background of Geographic map the main tectonic units are outlined: Easter Alps, Western Carpathians, Pannonian basin and Dinarides.

iments, upper crystalline and lower crust (Section 3.3). S-wave velocity and density — also relevant for geophysical modeling — can be derived following some scaling relation.

The second group — see Table 3.3 — consists of lines with a large spatial separation. This condition makes it impractical to extend information away from each single point and create a laterally-continuous model, as structure is expected to vary considerably over a length scale smaller than the average point spacing. In this group, consisting of 20 seismic lines, we collected refraction and reflection profiles located in the eastern- and southern-most part of our study region, shown in Figure 3.1. We should however be able to handle the crustal thickness data set, and combine it with other available information to create an updated Moho map. In the Aegean region, in addition to the reflection and refraction data (COR, EVO-I, EVO-II, SMM-A, SMM-B, CrSea, SeisMar, W-AnFE) we also collect values from the receiver functions study by Sodoudi et al. (2006). This should enable us to create a reliable estimate of Moho depth in that region.

3.3 Construction of a 3D model under the Eastern Alps

We wish to use all the information on the seismic structure of the crust, extracted from the literature following the procedures described below, to create a laterally-continuous model for the eastern Alpine region. In all, we have 1D models in 140 geographical points, that we need to interpolate laterally. We adopt the same vertical parametrization as in EPcrust: sediments, upper and lower cristalline layers. Thus, the inclusion of this regional model for an improved version of EPcrust will be straightforward. We consider the region within 11°E to 22°E, and from 45°N to 51°N with a nominal resolution of $0.2° \times 0.2°$. In principle, we could have a more detailed description of the local structure, with more than 3 layer in depth, but, as described in Molinari and Morelli (2011) we prefer to keep the parametrization as simple as possible.

3.3.1 Method

The model construction proceeds as follows. We first gather the dataset relative to each parameter (depth of each interface, and v_P in each layer). We then create a regular latitude-longitude grid, and assign values to such pixels from scattered data points, using a geo-statistical method — the ordinary kriging estimation procedure — as an interpolation scheme. With ordinary kriging it is possible to characterize an unknown regionalized variable, $Z(\mathbf{x})$ — a spatially-continue, random function with some geographical distribution — using the locations of its samples, or measurements (Olea, 2009). For the assessment of the spatial attributes, it is necessary to define a measure of spatial autocorrelation. It is customary to use the *semivariance* as a measure of the degree of spatial dependence between observations along a specific direction (Davis, 2002). Once the autocorrelation, in the form of the semivariogram, is computed and modelled, it is possible to estimate the value at any unsampled location, $Z(x_0)$, from the samples in a neighbourhood $\{Z(x_i), i = 1, n\}$, by solving a set of n equations (where n is the number of neighbourhood data used in the estimation) to find the n unknown weights:

$$Z^*(x_0) = \sum_{i=1}^{n} \lambda_i Z(x_i) \tag{3.1}$$

Here, $\{\lambda_i,\ i = 1, n\}$ are the kriging weights (Davis, 2002). This procedure ensures an optimal weighting function for non-uniform data distributions. Kriging provides the error variance of the estimation, σ_K^2, as a measure of precision, available in each point K where the kriging estimation is made:

$$\sigma_K^2 = \sum_{i=1}^{n} \lambda_i \gamma(x_i - x_0) - \mu \tag{3.2}$$

where $\gamma(x_i - x_0)$ is the semivariogram value for a distance between the x_0 and x_i sampled locations and μ is the Lagrange multiplier resulting from the solution of

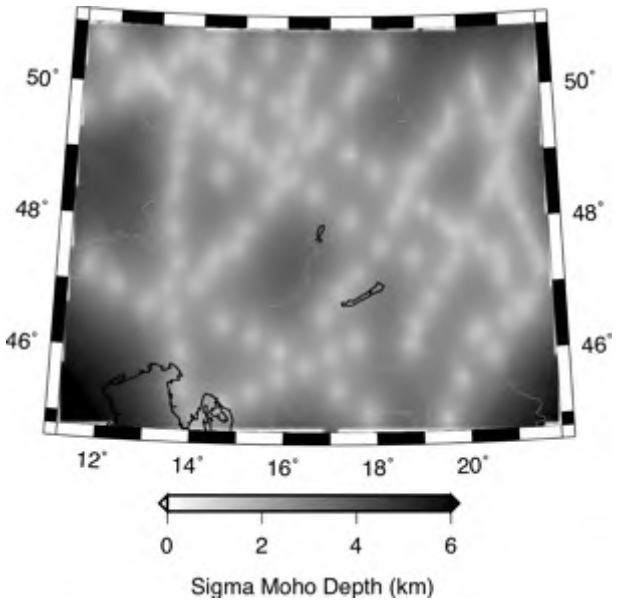

Figure 3.4: σ_K as resulting from Moho kriging interpolation.

the ordinary kriging system (Monteiro da Rocha and Yamamoto, 2000). However, this measure relies on the correctness of the modelled semivariogram (i.e. it only depends on the variogram, and not on data values) and it is not a usual expression of uncertainty (Yamamoto, 2000). To have an idea of the goodness of our kriging solution, in Fig 3.4 we plot the σ_K as resulting from Moho depth interpolation. We used the SGeMS software (Remy et al., 2009), that implements bivariate statistics and kriging techniques. The semivariogram for each parameter has been modelled with a spherical model. In most cases, semivariograms were drift free, and no spatial anisotropy has been detected. As an example, for Moho depth we find the sill region located beyond a range of about 3° (this means that within this range Moho depth values are correlated). The resulting grids have then been spatially filtered using a 50 km wide Gaussian filter (Wessel and Smith, 1998). More information about geostatistical methods ang kriging technique con be found in Appendix A.

To complete the model, we derive S-wave speed and density from scaling relation with respect to v_P (Brocher, 2005) derived from a Nafe-Drake curve regression. The so called *Brocher regression fit* is well suited for v_P values between 1.5 and 8 km/s and were used also in the EPcrust model. The relations can be found in equations2.1 and 2.2 (Chapter 2). Following this procedure, from the points identified in Figure 3.4, we obtain our final complete model explained in the next section.

3.3.2 Results

The new basement depth, Conrad discontinuities and Moho depth of the EA1.0 model are shown in Figure3.5-a,b,c. The P-wave velocity for each layer is shown in Figure 3.5-d,e,f.

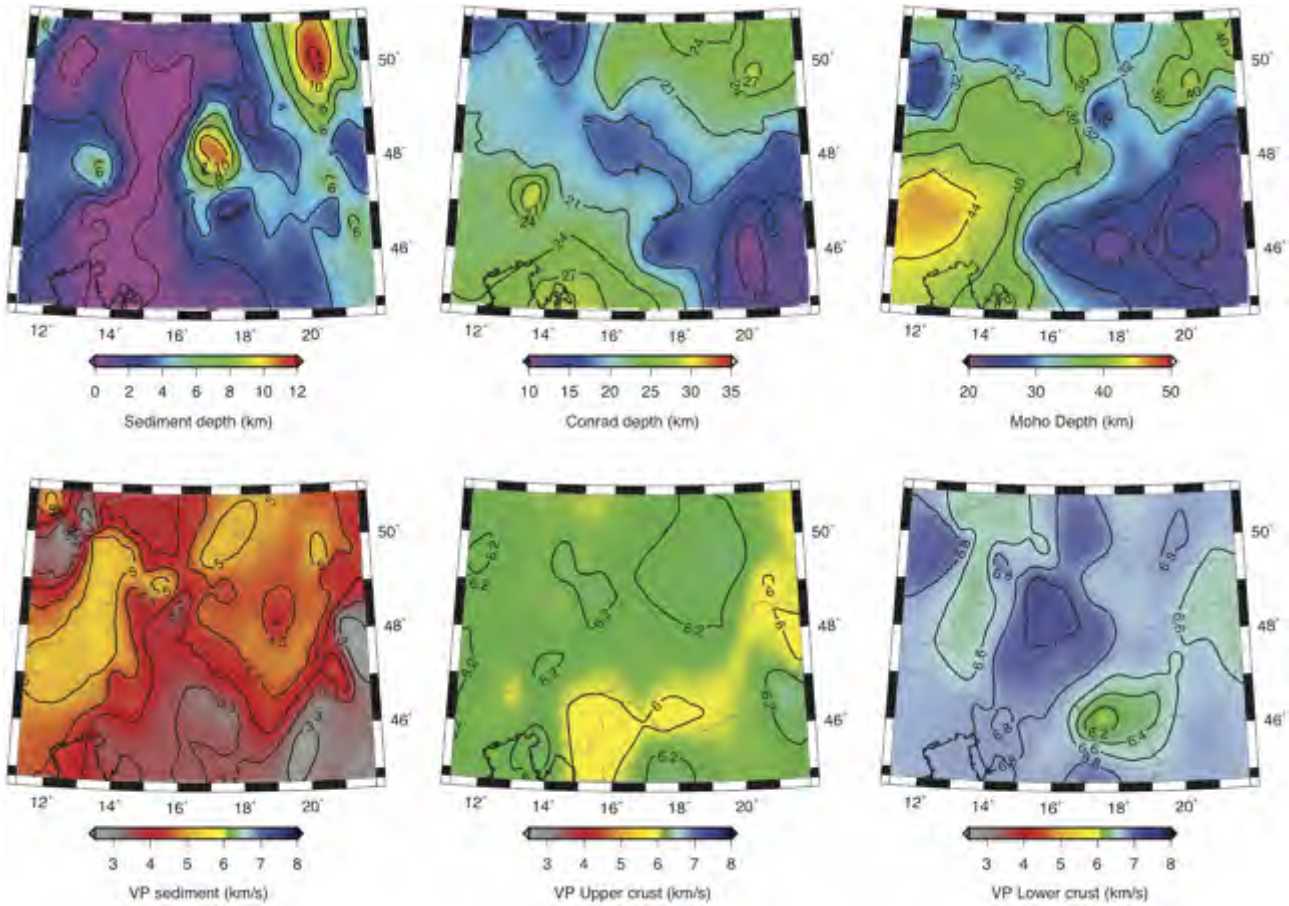

Figure 3.5: Maps of the parameters specified in East Alps local model. Sediment depth (a), Conrad depth (b) and Moho depth (c) (km), P-wave speed (km/s) in the sediment (d), upper (e) and lower (f) crustal layer.

Each of the three layers (sediments, upper and lower crust) has a laterally-varying thickness and P-wave speed, but is uniform with depth. The working representation is gridline-based on a $0.1° \times 0.1°$ grid, but the distribution format is based on $0.2° \times 0.2°$ grid due to the sampling resolution of the seismic lines. The region covered by the model is within $45° \times 51°$ N and $11° \times 22°$ E. Many features, present in the original 2D models, can also be found in the resulting 3D model, and generally reflect the main tectonic characters of the region. From a tectonic point of view, the area investigated is bordered by Dinarides to the South, Eastern and Southern Alps to the West, Bohemian Massif and Western Carpathians to the North and Pannonian basins to SE. In this area we find the collision area between three lithospheric plates: European, Adriatic and Pannonian (around 47° N and 14° E). The Eastern Alps represent the complex kinematic link between the Alps and the Alpine Belt of Eastern Europe, namely the Carpathians and the Dinarides. The Pannonian Basin adds further complexity to the general picture (Haas et al., 2000; Vannucci et al., 2004). The area is within the Phanerozoic part of Europe and includes Cenozoic collisional orogens associated with subducting lithospheric slabs (e.g. the Alps and the Carpathians) and basins such as the Pannonian basin, partially explained as a result of down-pull by cold subducting slab that lead to fast subsidence (Artemieva et al., 2006).

The Moho depth map (Figure 3.5c) reflects all these important features in the region. The Pannonian basin is characterized by a thin crust (20-30 km) that contrasts with crustal thickness under the Carpathians, up to 40 km, and Alpine structures (around 47 km). The crust became thicker in the Alps and in the West Carpathians: it is well known that the tectonics of the Alpine-Carpathians system was controlled by the convergence of the Adriatic and European plates during the Tertiary, that caused thrusting and crustal thickening. The jump (from Pannonian to Alpine structures) is well described along the ALP02 seismic line displayed in Fig.3.6b (thin rectangle in the front) with a section of our final model as background. The colour represents v_P within each layer along the section.

The Bohemian massif, that is part of the Variscan orogeny, has a Moho depth of 30 to 35 km. This terrane is well sampled by the SUDETS2003 seismic lines (Hrubcova et al., 2010). As an example, we cut the model as in Figure 3.6c, where it is possible to see that the Moho depth has no strong undulations in this area. Majdanski et al. (2007) model the 3D crustal structure of the Bohemian Massif, and they also found a Moho depth ranging from 28 to 35 km in the southern part of their domain. Seismic modelling studies have been performed in this key area by Behm et al. (2007), Grad et al. (2009a) and Behm (2009). Comparing our Moho map (Figure 3.5c) with the map by Behm et al. (2007) (Figure 11) we still find good agreement. In the Pannonian plate the Moho depth is between 25 and 32 km in both maps while in the European plate it became deeper, from 30 km under the Bohoemian Massif, to 45-50 km below the Alps. The Adriatic plate is not so well illuminated in the map by Behm et al. (2007) but we can still find the same Moho depth under the Istria peninsula and surronding areas, with values around 37-42 km.

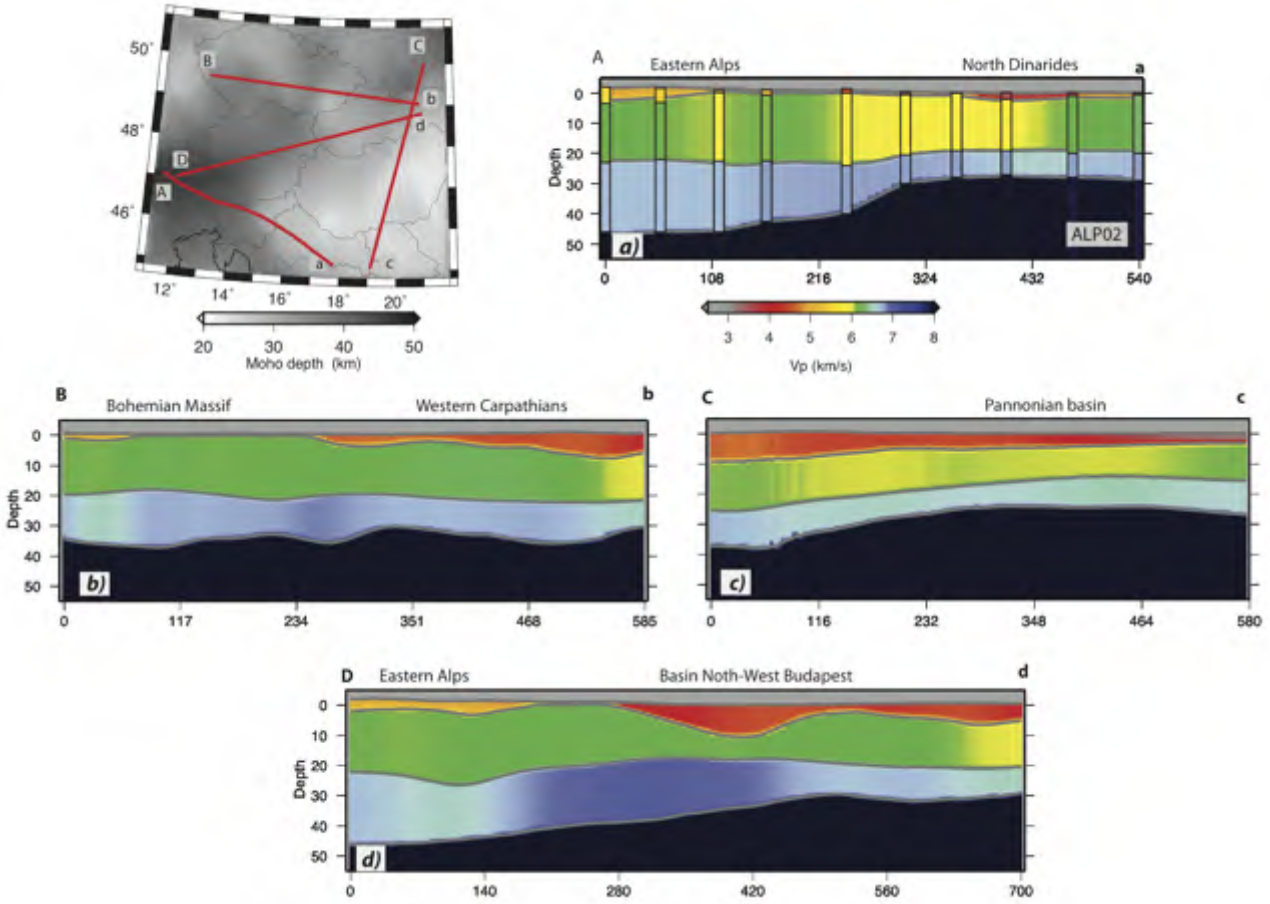

Figure 3.6: Synthetic cross-sections derived from EA01 crustal model. Each cross-section displays the basement, Conrad and Moho interfaces and P-wave speed in sediments, upper and lower crust. Horizontal length is in km. (top-left) layout of cross-sections; a) A-a cross-section running from the Eastern Alps to North Dinarides with 1D models (vertical columns) sampled from ALP02 crustal section; b) B-b cross-section from the Bohemian Massif to western Carpathians; c) C-c cross-section from the Western Carpathians to Pannonian basin; d) D-d cross-section from the Eastern Alps to basin NW Budapest.

The Conrad discontinuity lies within a depth between 12 and 30 km (Fig.3.5b), and crystalline crustal velocities are found to be around 6-6.4 km/s in the upper crust and from 6.3 to 7 km/s in the lower crust (respectively Figure 3.5e and 3.5f). These values are in overall agreement with crustal velocities found in the literature (Christensen and Mooney, 1995). Also, Grad et al. (2009a) found P-wave velocity of 6.15 km/s in the crystalline upper crust, and 7.0 km/s in the lower crust, under the Bohemian Massif, whereas Alpine upper and lower crust revealed, respectively, 6.0 km/s and 6.9 km/s. These value are also in agreement with the estimation by Majdanski et al. (2007), who found the upper and lower crust in the Bohemian Massif to have v_P speed between 6.0 to 6.3 and 6.7 to 7.2 km/s, respectively.

The depth to the basement (Fig. 3.5a) should be considered a lower limit of the basement; for a more detailed description it should in fact be divided into more than one layer. However, we can identify the most important sedimentary features of the region: a thin sedimentary layer in the western part, and an average sediment thickness of 5-6 km in the eastern area, were the Pannonian basin is located. The P-wave velocity range in the sediment layer (Figure 3.5d) is between 3 km/s (in the Pannonian basin, Figure 3.6d) to about 5 km/s in the western part of the region. Two deep basins (with a maximum of about 10-12 km depth) appear in our map: the first, at SE of Bratislava, with P-wave speed in accord with the v_P maps by Behm et al. (2007) at 7 km depth (Figure 3.6c); and the second in south-western Poland having high P-wave speed (more than 5 km/s). This region has been interpreted by Janik et al. (2009) as a strong anisotropic zone in the crust, that we partially included in the sedimentary layer. The sedimentary layer is very thin under the Bohemian Massif (Fig.3.5a and Fig.3.6b) while it becomes thicker going eastward (2-5 km). These features can also be found in Figure 8 by Majdanski et al. (2007).

3.4 Moho maps of the South Central and Eastern Europe

The seismic lines listed in Table 3.3 are not dense enough to safely interpolate structure among them. Additionally, for some of the lines we have not been able to collect information on all the parameters of interest. Consequently, we are not in the position here to create a complete local model such as EA1.0, described in the previous section. However, we are still able to extend and update the knowledge of the Moho interface, with respect to previous models, in the region within 35°N–51°N, and 12°W–45°E. To do this, from the collection of the depth values in the seismic profiles listed in Table 3.3, but also adding other published data — and using EPcrust as a background — we are able to assemble a new Moho map, Figure 3.7.

The Aegean is a tectonically active region with tens of strong earthquakes every year (Pondrelli et al., 2002) and a reliable Moho depth map is a requisite for many further studies. Here, we also gathered Moho depths from Sodoudi et al. (2006), whose estimates derive from P and S receiver functions. They make a distinction

from the Aegean (shallower) and African Moho (deeper). For our purpose, we consider only the Aegean. As shown in Figure 3.8, the two datasets together reach a rather good coverage on the region. We are thus able to apply the geostatistical techniques described in Section 3.1, to create a better estimate of the Moho depth in the Aegean region. Moreover, we also include the remaining profiles in the final grid ($35° \times 51°$ N, $12° \times 45°$) with a resolution of $0.2° \times 0.2°$ using EPcrust as a background. For the integration of different models and maps, we applied the same procedure as described in Molinari and Morelli (2011). In this way we came up with an update Moho map of the South-Central Eastern Europe with respect to previous models. The updated Moho map, Figure 3.7, displays three regions with different crustal thickness: $20 - 30$ km (the SE corner of map including the Aegean, Ionian and Tirrenian seas, Black Sea and Pannonian basin), $30 - 45$ km (most of continental plate) and more than 45 km (a few areas located into the North and North-East corner of map and belonging the the East European Platform or Carpathians orogen). In the Aegean region we found a mean Moho depth at about 25 km that becomes shallower (about 20 km) in the Aegean sea and deeper (40 km) in the Peloponnesus area and in the East of Marmara Sea. Our Moho depth map is in agreement with other studies in these regions, such as for example Karagianni et al. (2005) Sodoudi et al. (2006) and Tesauro et al. (2008). However, respect with Sodoudi et al. (2006), it map some differences within the range of ± 5 km as for example in the West of Cretan island, in the Sea of Marmara, where the new map show a shallower Moho around 30 km. Nevertheless we should not forget in the two local areas our model is based on refraction/reflection (Bohnhoff et al., 2001; Makris and Yegorova, 2006; Bécel et al., 2009) while the other model is rely on receiver function data where accuracy is lower. The Moho depth in Cretan area is also supported by Karagianni et al. (2005) with values of 29 ± 2.3 km in Eastern end of isle and as much as 36 km in the Western end.

3.5 Conclusion

The Eastern Alps region has been sampled by a large number of seismic experiments during the last two decades. We collected 37 2D seismic profiles from the literature, creating a geo-referenced dataset of the crustal parameters (thickness of sediments, depths to Conrad and Moho interfaces, P-/ S-wave speed and density profiles) along these lines. We incorporate all these data into a complete and continuous crustal model of the Eastern Alpine crust applying a geostatistical kriging algorithm. The new model covers a region within 11°E to 22°E and from 45°N to 51°N with a resolution of $0.2° \times 0.2°$ degrees. The model describe the main tectonic and structural features of the area. It is well suited for geophysical modeling, such as numerical wave propagation simulations, and as a reference for full seismic waveform inversion or classical mantle tomography. Due to its parameterization, its inclusion in continental-scale models, such as EPcrust (Molinari and Morelli, 2011), is straightforward.

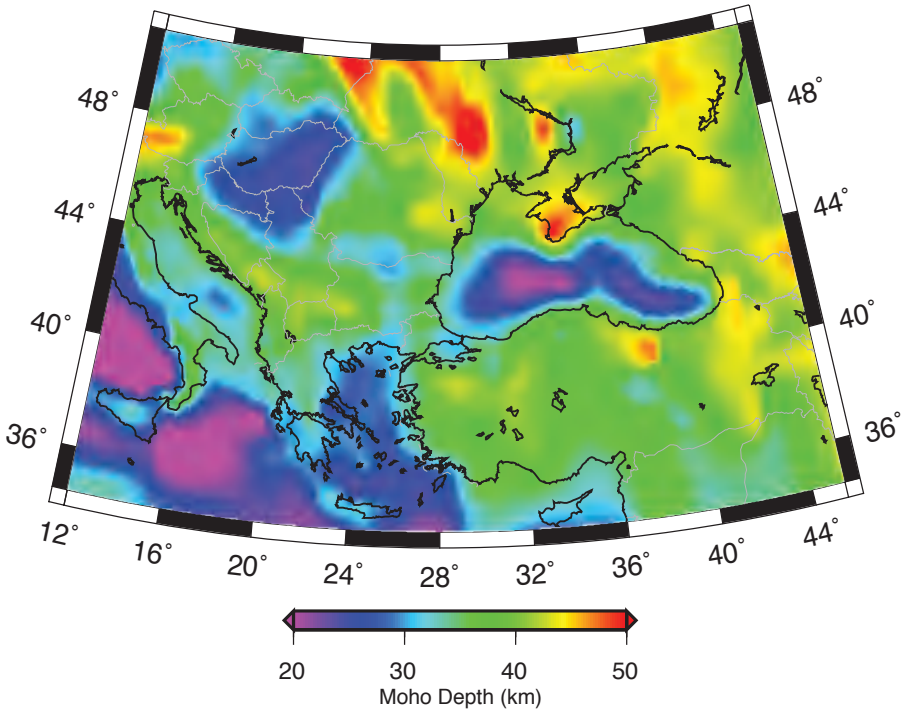

Figure 3.7: New Moho depth map of South Central East Europe obtained from seismic lines, Sodoudi et al. (2006) dataset, using EPcrust as background model.

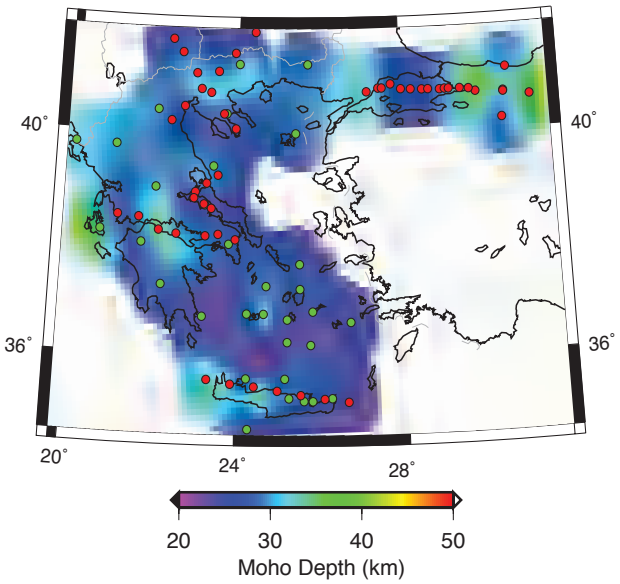

Figure 3.8: New Moho maps in Aegean Area. The red points are from our dataset from seismic lines and the green ones are from Sodoudi et al. (2006).

Additionally, we came up with an update Moho map of the South Central East Europe as an improvement to previous models, using seismic lines data, receiver function studies and EPcrust as background model.

The EA1.0 model, the Moho map and the collected seismic lines are all available as supplementary material or downloadable at *www.bo.ingv.it/eurorem/EPcrust* in order to make our results reproducible. Our results can be easily updated and extended as more detailed information will become available.

References

Angus, D.A., Wilson, D.C., Sandvol, E., Ni, J.F., 2006. Lithospheric structure of the Arabian and Eurasian collision zone in eastern Turkey from S-wave receiver functions. Geophysical Journal International 166(3), 1335–1346.

Artemieva, I.M., Thybo, H., Kaban, M.K., 2006. Deep Europe today; geophysical synthesis of the upper mantle structure and lithospheric processes over 3.5 Ga. Memoirs of the Geological Society of London 32, 11–41.

Avendonk, H.J.A.V., Holbrook, W.S., Nunes, G.T., Shillington, D.J., Tucholke, B.E., Louden, K.E., Larsen, H.C., Hopper, J.R., 2006. Seismic velocity structure of the rifted margin of the eastern Grand Banks of Newfoundland, Canada. J. Geophys. Res. 111, B11404. doi:10.1029/2005JB004156.

Baranov, A., 2010. A new crustal model for central and southern Asia. Izv-Phys. Solid Earth 46(1), 34–46. doi:10.1134/S1069351310010039.

Bassin, C., Laske, G., Masters, G., 2000. The current limits of resolution for surface wave tomography in North America. Eos Trans. AGU 81, 48.

Bécel, A., Laigle, M., de Voogd, B., Hirn, A., Taymaz, T., Galva, A., Shimamura, H., Murai, Y., Lépine, J., Sapin, M., Özalaybey, S., 2009. Moho, crustal architecture and deep deformation under the North Marmara Trough, from the SEISMARMARA leg 1 offshore-onshore reflection-refraction survey. Tectonophysics 467(1-4), 1–21. doi:10.1016/j.tecto.2008.10.022.

Behm, M., 2009. 3-D modelling of the crustal s-wave velocity structure from active source data: application to the Eastern Alps and the Bohemian Massif. Geophysical Journal International 179(1), 265–278.

Behm, M., BrÃ$\frac{1}{4}$ckl, E., Chwatal, W., Thybo, H., 2007. Application of stacking and inversion techniques to three-dimensional wide-angle reflection and refraction seismic data of the Eastern Alps. Geophysical Journal International 170(1), 275–298.

Bohnhoff, M., Makris, J., Papanikolaou, D., Stavrakakis, G., 2001. Crustal investigation of the hellenic subduction zone using wide aperture seismic data. Tectonophysics 343(3-4), 239–262. doi:10.1016/S0040-1951(01)00264-5.

Brocher, T.M., 2005. Empirical relations between elastic wavespeeds and density in the Earth's crust. Bull. Seis. Soc. Am. 95(6), 2081–2092.

Brueckl, E., Bodoky, T., Hegedas, E., Hrubcova, P., Gosar, A., Grad, M., Guterch, A., Hajnal, Z., Keller, G.R., Spicak, A., Sumanovac, F., Thybo, H., Weber, F., 2003. ALP 2002 seismic experiment. Studia Geophysica et Geodaetica 47, 671–679. 10.1023/A:1024780022139.

Christensen, N.I., Mooney, W.D., 1995. Seismic velocity structure and composition of the continental crust; a global view. J. Geophys. Res. 100(B6), 9761–9788.

Davis, J., 2002. Statistics and Data Analysis in Geology. John Wiley & Sons. third edition.

Faccenna, C., Becker, T.W., 2010. Shaping mobile belts by small-scale convection. Nature 465(7298), 602–605. doi:10.1038/nature09064.

Grad, M., Brueckl, E., Majdanski, M., Behm, M., Guterch, A., CELEBRATION 2000 and ALP 2002 Working Groups, 2009a. Crustal structure of the eastern alps and their foreland: seismic model beneath the CEL10/Alp04 profile and tectonic implications. Geophysical Journal International [Geophys. J. Int.]. Vol. 177 (1), 279–295.

Grad, M., Gryn, D., Guterch, A., Janik, T., Keller, R., Lang, R., Lyngsie, S.B., Omelchenko, V.D., Starostenko, V.I., Stephenson, R.A., Stovba, S.M., Thybo, H., Tolkunov, A., 2003a. "DOBREfraction'99"; velocity model of the crust and upper mantle beneath the Donbas Foldbelt (east Ukraine). Tectonophysics 371(1-4), 81–110.

Grad, M., Guterch, A., Keller, G.R., Janik, T., Hegedűs, E., Vozar, J., Slaczka, A., Tiira, T., Yliniemi, J., 2006a. Lithospheric structure beneath trans-Carpathian transect from precambrian platform to pannonian basin: CELEBRATION 2000 seismic profile CEL05. J. Geophys. Res. 111(B3), B03301.

Grad, M., Guterch, A., Mazur, S., Keller, G.R., Spicak, A., Hrubcova, P., Geissler, W.H., 2008. Lithospheric structure of the Bohemian Massif and adjacent Variscan Belt in Central Europe based on profile s01 from the SUDETES 2003 experiment. Journal of Geophysical Research 113(B10), Citation B10304.

Grad, M., Janik, T., Guterch, A., Sroda, P., Czuba, W., 2006b. Lithospheric structure of the western part of the East European Craton investigated by deep seismic profiles. Geological Quarterly 50(1), 9–22. accessed on April 15, 2010.

Grad, M., Spicak, A., Keller, G.R., Guterch, A., Broz, M., Hegedus, E., Behm, M., Bodoky, T., Brinkmann, R., Brueckl, E., Czuba, W., Fancsik, T., Forkmann, B., Fort, M., Gaczynski, E., Geissler, W.H., Greschke, R., Harder, S.H., Hemmann, A., Hrubcova, P., Janik, T., Jentzsch, G., Kaip, G., Komminaho, K., Korn, M., Karousova, O., Majdanski, M., Malek, J., Malinowski, M., Miller, K.C., Rumpfhuber, E.M., Sroda, P., Takacs, E., Tiira, T., Vozar, J., Wilde-Piorko, M., Yliniemi, J., Zelazniewicz, A., 2003b. SUDETES 2003 seismic experiment. Studia Geophysica et Geodetica 47(3), 681–689.

Grad, M., Tiira, T., Group, E.W., 2009b. The moho depth map of the European Plate. Geophys. J. Int. 176(1), 279–292. doi:10.1111/j.1365-246X.2008.03919.x.

Grad, M., Tripolsky, A.A., 1995. Crustal structure from p and s seismic waves and petrological models of the ukrainian shield. Tectonophysics 250(1-3), 89–112. doi:10.1016/0040-1951(95)00045-X.

Guterch, A., Grad, M., 2006. Lithospheric structure of the TESZ in poland based on modern seismic experiments. Geological Quarterly 50(1), 23–32. accessed on April 15, 2010.

Guterch, A., Grad, M., Keller, G.R., Posgay, K., Vozar, J., Spicak, A., Brueckl, E., Hajnal, Z., Thybo, H., Selvi, O., Acevedo, S., Aric, K., Asudeh, I., Belinsky, A.A., Bodoky, T., Chwatal, W., Clowes, R., Czuba, W., Fancsik, T., Gaczynski, E., Harder, S.H., Hegedus, E., Hrubcova, P., Janik, T., Jentzsch, G., Joergensen, P., Kaip, G., Keller, G.R., Komminaho, K., Kostiuchenko, S.L., Kracke, D., Kohlbeck, F., Miller, K.C., Morozov, A.F., Snelson, C.M., Sroda, P., Takacs, E., Tiira, T., Wilde-Piorko, M., Yliniemi, J., 2003. CELEBRATION 2000 seismic experiment. Studia Geophysica et Geodetica 47(3), 659–669.

Guterch, A., Grad, M., Thybo, H., Keller, G.R., 1999. POLONAISE '97 – an international seismic experiment between Precambrian and Variscan Europe in Poland. Tectonophysics 314(1-3), 101–121. doi:10.1016/S0040-1951(99)00239-5.

Haas, J., Mioc, P., Pamic, J., Tomljenovic, B., Arkai, P., Berczi-Makk, A., Koroknai, B., Kovacs, S., Felgenhauer, E., 2000. Complex structural pattern of the Alpine-Dinaridic-Pannonian. Int. J. Earth Sci. 89, 377–389.

Hauser, F., Raileanu, V., Fielitz, W., Bala, A., Prodehl, C., Polonic, G., Schulze, A., 2001. VRANCEA99–the crustal structure beneath the southeastern carpathians and the moesian platform from a seismic refraction profile in romania. Tectonophysics 340(3-4), 233–256. doi:10.1016/S0040-1951(01)00195-0.

Hauser, F., Raileanu, V., Fielitz, W., Dinu, C., Landes, M., Bala, A., Prodehl, C., 2007. Seismic crustal structure between the transylvanian basin and the black sea, romania. Tectonophysics 430(1-4), 1–25. doi:10.1016/j.tecto.2006.10.005.

Hrubcová, P., Sroda, P., 2008. Crustal structure at the easternmost termination of the variscan belt based on CELEBRATION 2000 and ALP 2002 data. Tectonophysics 460(1-4), 55–75. doi:10.1016/j.tecto.2008.07.009.

Hrubcova, P., Sroda, P., Grad, M., Geissler, W.H., Guterch, A., Vozar, J., Hegedus, E., Group, S..W., 2010. From the variscan to the alpine orogeny: crustal structure of the bohemian massif and the western carpathians in the light of the SUDETES 2003 seismic data. Geophysical Journal International 183(2), 611–633.

Hrubcova, P., Sroda, P., Spicak, A., Guterch, A., Grad, M., Keller, G.R., Brueckl, E., Thybo, H., 2005. Crustal and uppermost mantle structure of the Bohemian Massif based on CELEBRATION 2000 data. J. Geophys. Res. 110(B11), 21.

Janik, T., Grad, M., Guterch, A., 2009. Seismic structure of the lithosphere between the East European Craton and the Carpathians from the net of CELEBRATION 2000 profiles in SE poland. Geol. Q. 53(1), 141–158.

Kaban, M., Tesauro, M., Cloetingh, S., 2010. An integrated gravity model for europe's crust and upper mantle. Earth and Planetary Science Letters 296(3-4), 195–209. doi:10.1016/j.epsl.2010.04.041.

Karagianni, E.E., Papazachos, C.B., Panagiotopoulos, D.G., Suhadolc, P., Vuan, A., Panza, G.F., 2005. Shear velocity structure in the aegean area obtained by inversion of rayleigh waves. Geophysical Journal International 160(1), 127–143.

Karahan, A.E., Berckhemer, H., Baier, B., 2001. Crustal structure at the western end of the North Anatolian Fault Zone from deep seismic sounding. Annals of Geophysics 44(1).

Kawase, H., 2003. Site effects on strong ground motions, In: International handbook of earthquake & engineering seismology. Academic Press-Elsevier.

Levshin, A.L., Ritzwoller, M.H., 2002. Application of a global 3d model to improve regional event location. Stud. Geophys. Geod. 46, 283–292.

Majdanski, M., Grad, M., Guterch, A., 2006. 2-D seismic tomographic and ray tracing modelling of the crustal structure across the sudetes mountains basing on SUDETES 2003 experiment data. Tectonophysics 413(3-4), 249–269. doi:10.1016/j.tecto.2005.10.042.

Majdanski, M., Kozlovskaya, E., Grad, M., 2007. 3d structure of the earth's crust beneath the northern part of the bohemian massif. Tectonophysics 437(1-4), 17 – 36. doi:DOI: 10.1016/j.tecto.2007.02.015.

Makris, J., Papoulia, J., Papanikolaou, D., Stavrakakis, G., 2001. Thinned continental crust below northern evoikos gulf, central greece, detected from deep seismic soundings. Tectonophysics 341(1-4), 225–236. doi:10.1016/S0040-1951(01)00186-X.

Makris, J., Yegorova, T., 2006. A 3-D density-velocity model between the cretan sea and libya. Tectonophysics 417(3-4), 201–220. doi:10.1016/j.tecto.2005.11.003.

Meszaros, F., Zilahi-Sebess, L., 2001. Compaction of sediments with great thickness in Pannonian Bassin. Geophysical Transactions 44(1), 195–209.

Molinari, I., Morelli, A., 2011. EPcrust: A reference crustal model for the european plate. Geophys. J. Int. under review.

Olea, R.A., 2009. A practical primer on geostatistics. U.S. Geological Survey Open-File Report 2009-1103 p. 346.

Papazachos, C.B., 1998. Crustal p- and s-velocity structure of the serbomacedonian massif (Northern greece) obtained by non-linear inversion of traveltimes. Geophysical Journal International 134(1), 25–39.

Pavlenkova, N., 1988. The nature of seismic boundaries in the continental lithosphere. Tectonophysics 154(3-4), 211–225. doi:10.1016/0040-1951(88)90104-7.

Pondrelli, S., Morelli, A., Ekström, G., Mazza, S., Boschi, E., Dziewonski, A.M., 2002. European-Mediterranean regional centroid-moment tensors: 1997-2000. Phys. Earth Planet. Inter. 130(1-2), 71–101. doi:10.1016/S0031-9201(01)00312-0.

Raileanu, V., Diaconescu, C., Radulescu, F., 1994. Characteristics of romanian lithosphere from deep seismic reflection profiling. Tectonophysics 239(1-4), 165 – 185. doi:DOI: 10.1016/0040-1951(94)90113-9.

Remy, N., Bouchera, A., Wu, J., 2009. Applied Geostatistics with SGeMS: A User's Guide. Cambridge University Press.

Monteiro da Rocha, M., Yamamoto, J.K., 2000. Comparison between kriging variance and interpolation variance as uncertainty measurements in the Capanema Iron Mine, State of Minas GeraisÑBrazil. Natural Resources Research 9, 223–235. 10.1023/A:1010195701968.

Ruzek, B., Hrubcova, P., Novotny, M., Spicak, A., Karousova, O., 2007. Inversion of travel times obtained during active seismic refraction experiments CELEBRATION 2000, ALP 2002 and SUDETES 2003. Studia Geophysica et Geodaetica 51, 141–164. 10.1007/s11200-007-0007-6.

Schivardi, R., Morelli, A., 2011. EPmantle: a three-dimensional transversely isotropic model of the upper mantle under the European Plate. Geophys. J. Int. .

Sodoudi, F., Kind, R., Hatzfeld, D., Priestley, K., Hanka, W., Wylegalla, K., Stavrakakis, G., Vafidis, A., Harjes, H.P., Bohnhoff, M., 2006. Lithospheric structure of the Aegean obtained from P and S receiver functions. J. Geophys. Res. 111(B12).

Somerville, P., Moriwaki, Y., 2003. Seismic hazard and risk assessment in engineering practice. In: International handbook of earthquake & engineering seismology. Academic Press-Elsevier.

Sroda, Czuba, W., Grad, M., Guterch, A., Tokarski, A.K., Janik, T., Rauch, M., Keller, G.R., HegedÃ$\frac{1}{4}$s, E., VozÃ¡r, J., Group, C..W., 2006. Crustal and upper mantle structure of the western carpathians from CELEBRATION 2000 profiles CEL01 and CEL04: seismic models and geological implications. Geophysical Journal International 167(2), 737–760.

Sroda, P., Czuba, W., Grad, M., Guterch, A., Tokarski, A.K., Janik, T., Rauch, M., Keller, G.R., Hegedus, E., Vozar, J., Anonymous, 2005. Crustal structure of the Western Carpathians from CELEBRATION 2000 data. Geolines (Prague) 19, 109.

Sumanovac, F., 2010. Lithosphere structure at the contact of the adriatic microplate and the pannonian segment based on the gravity modelling. Tectonophysics 485(1-4), 94–106. doi:10.1016/j.tecto.2009.12.005.

Sumanovac, F., Oresokoviska, J., Grad, M., Group, A..W., 2009. Crustal structure at the contact of the dinarides and pannonian basin based on 2-D seismic and gravity interpretation of the alp07 profile in the ALP 2002 experiment. Geophysical Journal International 179(1), 615–633.

Tesauro, M., Kaban, M.K., Cloetingh, S.A.P.L., 2008. EuCRUST-07: a new reference model for the European crust. Geophys. Res. Lett. 35, L05313. doi:10.1029/2007GL032244.

Vannucci, G., Pondrelli, S., Argnani, A., A Morelli, P Gasperini, E.B., 2004. An atlas of mediterranean seismicity. Annals of Geophysics 47(1), 247–306.

Wessel, P., Smith, W.H.F., 1998. New, improved version of the Generic Mapping Tools released. Eos Trans. AGU 79, 579.

Yamamoto, J.K., 2000. An alternative measure of the reliability of ordinary kriging estimates. Math. Geology. 32, 489–509.

Zelt, B.C., Taylor, B., Sachpazi, M., Hirn, A., 2005. Crustal velocity and moho structure beneath the Gulf of Corinth, Greece. Geophysical Journal International 162(1), 257–268.

Chapter 4

Numerical representation of crustal structure for realistic seismograms

Contents

4.1 Introduction

In the last decade, a lot of efforts were done in the development of numerical methods and codes for seismic wave propagation in realistic Earth models (e.g. Igel and Weber, 1996; Komatitsch and Tromp, 2002; Dumbser and Kaeser, 2006). It is well known that knowledge of the crustal structure is a key issue in realistic seismic wave propagation simulation: sedimentary basin and low velocity zones can strongly affect wave propagation. In order to obtain realistic seismograms, it is important to understand how the knowledge and the geometry discretization of the crustal model impacts synthetic waveforms. A correct implementation of the crustal structure, respecting all the discontinuity boundaries, seem to be a crucial point for the accuracy of numerical solutions of the elastic wave equation in continental or global scale scenarios. Lacks of knowledge in the shallower structure of the Earth in addition with the extremely variable thickness of the sedimentary layer and the undulating depth of the Moho discontinuity lead to challenging problems in the representation of these structure in numerical meshes.
Focusing on European scale, all the available crustal models (Molinari and Morelli, 2011; Tesauro et al., 2008; Bassin et al., 2000) have a layered vertical format, as they are divided into sediment, upper and lower crust. In most of the cases, the

In preparation as: Molinari I., Kaeser M. and Morelli A. – *"Numerical representation of crustal structure for realistic seismograms"*. 2011.

parameters such as the interfaces depth are known only with significant uncertainties –EPcrust, at least, provides a variability range on the crustal parameters— and the error on the determination of each parameter is not clear. Focusing on realistic earthquake simulations in the European region at relatively high frequency ($0.02 - 0.1$ Hz), the goodness of the knowledge and implementation of the crustal structure became a non trivial problem, especially when surface waves are considered since they are mostly influenced by crustal structure.
Creation of a mesh for the whole European crust honouring all discontinuities would probably be the best option but it will be cumbersome with actual meshing software (e.g. Cubit, ICEM CFD, Gambit). The resulting mesh will be computationally expensive when the layer thickness becomes extremely thin (only hundreds of meters), as in such cases a very fine mesh spacing in necessary in order to respect the interfaces, which reduces the time step for explicit numerical schemes due to stability reasons. In some global simulation codes – e.g. SPECFEM3D, (Komatitsch and Tromp, 2002) –, the crustal structure is not completely honoured by the meshes through the alignment of element edges, even though the new version of the code seems to honour the Moho depth in most of the region; other layers are not explicitly represented in the mesh. The material values are interpolated internally within each element at GLL points and the sedimentary layer is neglected when it becomes thinner than 2 km. This could be a good compromise between computational costs and accuracy in the simulation, but no quantitative studies on the possible errors due to these approximations were performed.
Pelties et al. (2010) quantitatively analysed the numerical errors associated with approximations of material discontinuities using the DG method (Kaeser and Dumbser, 2006). In particular, the authors focus the attention on local scale (hundreds of meters) and very high frequency (5 - 0.1 Hz) finding that, in this set-up, the acceptableness of synthetics due to different interface representations strongly depends on the material contrast between elements.

Following this kind of studies, the aim of this work is to quantitatively investigate the effects in the simulated wave field of lacks of knowledge in the crustal models and of sharpness discontinuities representation. We perform our test in thousands kilometer-long 2D sections of the recent EPcrust model (Chapter 2) within a frequency range between 0.1 and 0.02 Hz (periods of 10-50 s). These results can be easily transferred to 3D to help to construct meshes for this computationally much more demanding case. In particular our aim is to answer the following questions:

1. At continental distance (hundreds and thousands of kilometers), is it really important to respect all the discontinuities of the crust (e.g. Moho, upper-lower crust, sedimentary basins) by mesh alignment?

2. How important is the discrete model resolution with respect to the targeted scale, global, continental, regional, local?

3. If we neglect to respect the discontinuities in the crust by the mesh, how large will be the errors of the synthetic seismograms with respect to the surface

waves phase?

4. To what discretization rules (with respect to the desired frequency band) modelers/users have to adhere, if they model continental scale wave propagation in a realistic crustal model?

5. Is the geometry approximation as crucial as the knowledge of the velocity distribution?

6. How does the error due to simplified mesh generation or due to a lack of knowledge in the model depend on the frequency band of the seismic signal. Where is the limit of acceptance with respect to a separate investigation of envelope and phase errors?

The chapter is structured as follows. In section 2 we describe the setting up of the tests scenario, in section 3 we briefly summarize the technique adopted to quantify the misfit, in Section 4 and 5 we describe the results followed by a discussion section.

4.2 Test Scenarios in 2D

In this study, we take into considerations realistic 2D sections of a crustal model of the European region, since they are usually implemented in numerical method for seismic wave propagation. For simplicity, crustal models usually have a layered vertical parametrization (Bassin et al., 2000; Tesauro et al., 2008; Molinari and Morelli, 2011) with the seismological parameters variable along the horizontal directions and constant in each layer along the vertical. In order to make realistic simulations we need a complete model of the Earth with all the seismic parameters specified. For this reason, as reference geometries, we consider cross sections of the European crustal model from Molinari and Morelli (2011) shown in the bottom of Fig 4.1, along the great circle path shown in the top of Fig. 4.1.

In the set-up of the problem we proceed as follow. From the 5000 km long section in Figure 4.1, we create a reference mesh (referred as *'REF'*) in which the average edge lengths of the triangles are less than the distance of data points in the crustal velocity model. We put 101 receivers along the surface with a regular distance of 50 km (Figure 4.1). The source is a single force located in the crust at Longitude 29.07E and latitude 45.4155N (corresponding to $x = 2500$ km from the beginning of the section) and 30.0 km depth and has a peak frequency of 0.1 Hz. The simulations are of 1200 s length.

In the *REF* mesh (Figure 4.2) , we respect all the discontinuities present in our 2D model (i.e. sediment basement, bottom of upper crust and Moho). The elements size grows from the top to the bottom of each layer; the v_S minimum and maximum values in the 2D model and relative required mesh spacing is shown in Table 4.2. The material properties are assigned to the barycentre of each triangle and are representative for the entire area covered by the corresponding element. The general rule to ensure the accuracy of the numerical scheme is to mesh the media

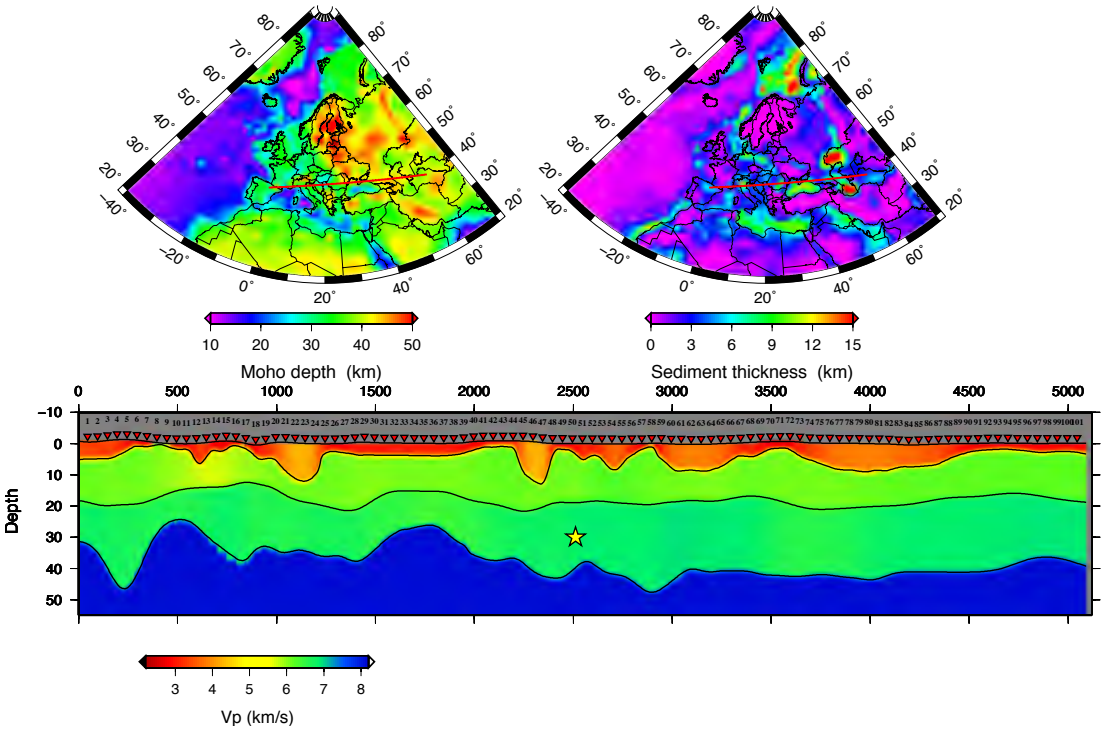

Figure 4.1: Top: Moho depth (left) and sediment thickness (right) in EPcrust Molinari and Morelli (2011). Bottom: about 5000 km cross section of EPcrust used in the simulations along the red line displayed in the maps, with receivers and source. The colors show the v_P velocity in each crustal layer.

with, at least, two elements per wavelength (using the 4th order scheme). Selecting a minimum period, $T = 5$ s, we are able to calculate the corresponding minimum mesh spacing needed in our case (Table 4.1) for each layer.

For the simulations we use the Discontinuous Galerkin Finite Element Method –ADER-DG– (Kaeser and Dumbser, 2006; Dumbser et al., 2007) providing high-order accuracy in space and time (we use order 4) on unstructured meshes. With this approach strong and undulating discontinuities can be considered by the element interfaces and modifications of the geometrical properties can be carried out rapidly due to an external mesh generation process. For two dimensional problems, this method is implemented in the well tested code SeisSol2D, and for 3D domains in SeisSol3D. More information about the code and about ADER-DG method can be found in Appendix B and at *www.geophysik.uni-muenchen.de/∼kaeser/SeisSol/*.

We tests different representations and different assumption of knowledge of the structure of the 2D crustal model. We simulate the same source in different meshes of the same section but with perturbed characteristics: meshes in which we do not respect some discontinuities in the crust such as the sediment and upper crust interface or only the sediment layer when it became thinner than 2 km. Moreover, we perturb the sediment and Moho interfaces depth of constant quantities comparable with the error on crustal parameters in the available models and the crustal velocity

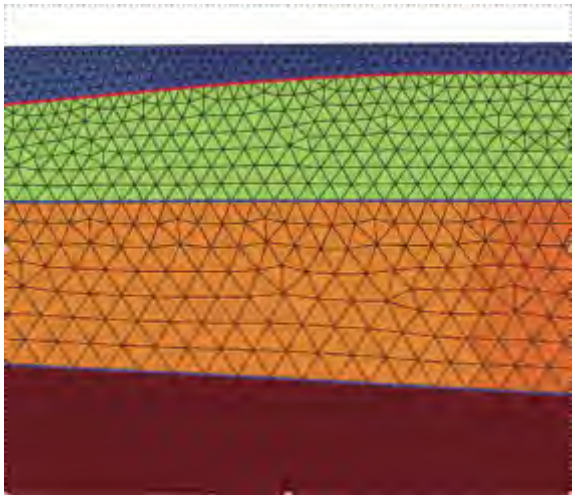

Figure 4.2: A zoom of the reference mesh. Alle the discontinuities are honoured by mesh alignment.

Table 4.1: Seismic properties of the EPcrust section used in this work. v_S is expressed in m/s and the associated right minimum mesh spacing (h) in meters for wave with minimum period of T = 5 seconds. (Two elements mesh for each wavelength)

Layer	v_S^{min}	v_S^{av}	v_S^{max}	h_{min}	h_{av}	h_{max}
Sediment	920	1630	2330	2300	4075	5825
Upper Crust	3390	3530	3670	8475	8825	9175
Lower Crust	3720	3840	3960	9300	9600	9900

structure of the whole 2D section with a random function. The characteristics of these meshes are listed in Table 4.2. In each test, we apply the same set-up used for the reference mesh (source, receivers configuration) and we recorder the seismogram at the same points (101 receivers) in all the tests in order to compare the results.

Is it important to point out that the Earth's curvature is taken into account in our 2D meshes: in Figure 4.3 we show a snapshot of the simulation in the reference mesh. It is possible to see the 2D wave field propagating through the 2D slice; zooming on the crust (Figure 4.3-b) and comparing it with the structure (Figure 4.3-c) it is possible to have an idea of the wave amplification in these thin layers.

To test the effects of different representation of the crust, we compare the synthetic seismograms obtained in each simulation with the reference seismograms (from the *REF* mesh). We compare only the surface wave phase of the signals, since it is the most sensitive to the shallower structure (see Chapter 1).

The data processing procedure and the misfit criteria chosen to compare the seismograms are briefly described in the next section.

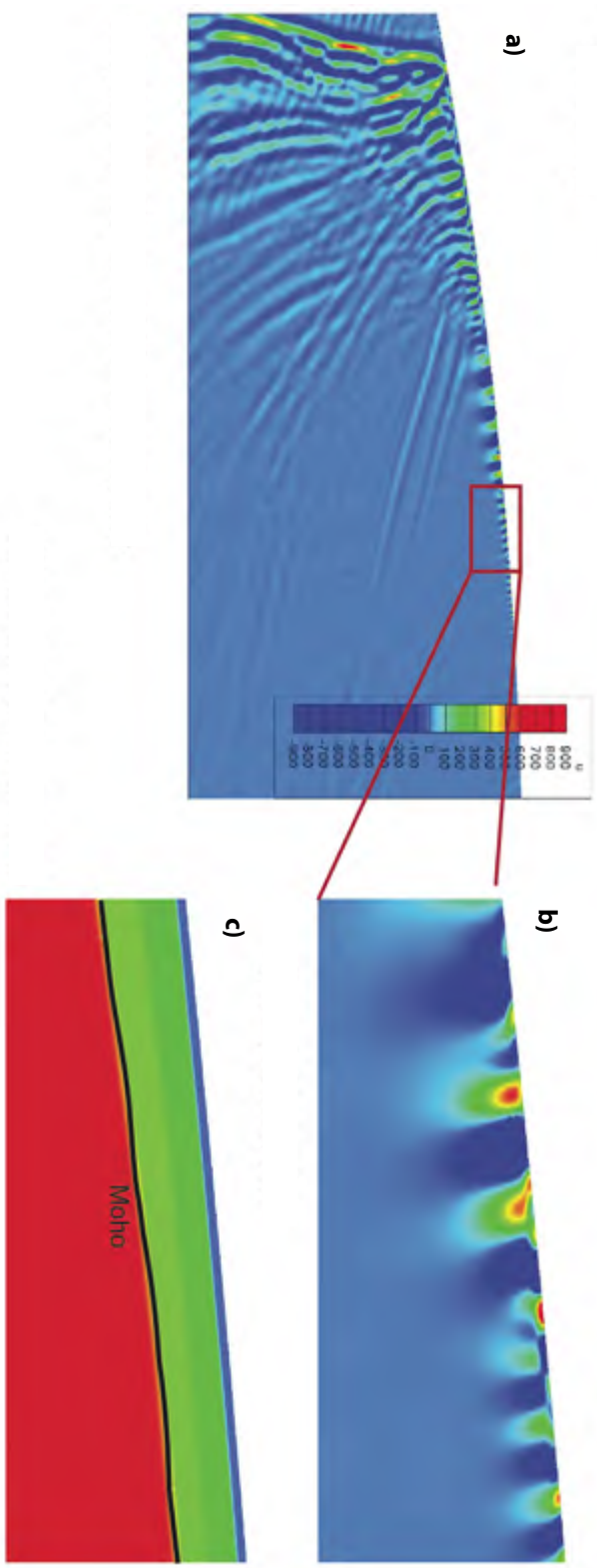

Figure 4.3: a) Snapshot at 400 seconds after the earthquake. Only a part of the mesh is shown here. b) Zoom on crustal propagation. c) Crustal structure as in b).

4.3 Accuracy analysis of synthetic seismograms

In order to detect any changes in the recorded signals due to the different meshes, we need a measure to quantify differences between seismograms. A simple visual comparison, in some case, could help but it is not quantitatively informative. The simplest misfit is the difference in time between a reference ($Sr(t)$) and the tested ($S(t)$) signal and a widely used misfit is the root mean square error ($RMS = \sqrt{|S(t) - Sr(t)|^2/|Sr(t)|^2}$) to get a single value misfit. However both of them are not always well suitable for a quantitatively seismograms comparison and they are not able to characterize the nature of the detected difference tend to overestimate the error with respect to a separate phase and envelope misfit error. Recently, Kristekova et al. (2006, 2009) developed misfit criteria based on a time-frequency representation of signals using the continuous wavelet transform, able to obtain separate information on the phase and envelope errors. A time-frequency approach is also followed by Fichtner et al. (2009) in the definition of the misfit function for full waveform inversion tomography. In this work we widely apply the TF misfit criteria by Kristekova et al. (2009) to quantify the differences between reference and test seismograms from the different meshes. A description of these criteria is given in Appendix D.

In all test cases, for each set of seismograms we proceeded as follow. We apply a lowpass filter at each signal with a corner frequency of 0.2 Hz in order to cut the higher frequencies avoiding any numerical dispersion effects. Then, we select the surface wave phase in the seismogram using an automatic selection criteria based on surface wave speed and source-receiver distance. The selected phase is then tapered in order to correctly apply the TF misfit criteria (Kristekova et al., 2009). Each set of seismograms is compared with the reference set (from *REF* mesh) and single value globally normalized phase (PM) and envelope (EM) misfits were calculated (see Appendix D) for each station and for different frequency ranges ($0.1 - 0.15$ Hz, $0.08 - 0.1$ Hz, $0.06 - 0.08$ Hz, $0.05 - 0.06$ Hz, $0.041 - 0.05$ Hz). We analyse EM and PM as a function of station position and frequency rage. These kind of plots give us an idea on the distribution of the error as a function of the structure of the model and of the mesh approximations.

In order to have a single measure for the error in each test, we calculate a cumulative phase (CPM) and envelope misfit (CEM) for each test and for each frequency range:

$$CPM = \frac{\sum_i (PM(u_i) + PM(v_i))}{2n} \tag{4.1}$$

$$CEM = \frac{\sum_i (EM(u_i) + EM(v_i))}{2n} \tag{4.2}$$

where n is the number of receivers, u_i and v_i are the horizontal and vertical component of the $i - th$ receiver respectively. An example of CEM and CPM results is shown in the last section of this chapter. The cumulative misfit will give a measure of the goodness of the approximations considered in each test and is useful to un-

derstand which approximation has a stronger impact on the synthetics. All the test cases and the results are analysed in the next sections.

4.4 Shallow crustal layer structure

We perform synthetics seismograms using different representation of the shallower layer of the considered 2D crustal section (sediment and Conrad interface). We divided these of tests in four sub-groups. The first involves the representation of the interface using sharpness representation of the basement and upper-lower crust interface while the second regards the uncertainty on the knowledge of the sediment depth. The third and last groups are about a perturbed knowledge of the Moho depth and the velocity structure respectively. The main motivation for this kind of tests is to understand for which frequency range we can neglect the imperfect representation and knowledge of the sediment and Conrad depth. The characteristics of these meshes are listed in Table 4.2. We describe in details the results from these test cases in the following sections.

Table 4.2: Name and characteristics of the meshes used. We list the discretization length used in the creation of the mesh for each interface.

Meshes	Topography	Sediment	UC	LC	Mantle
REF	800	1100	2000	3000	40000
REF Coarse	1500	2500	3000	5000	40000
Sharp	800	-	-	3000	40000
Sharp Coarse	1500	-	-	5000	40000
Cutoff 2km sedi	800	1100	2000	3000	40000
Sedi +200 m	800	1100	2000	3000	40000
Sedi +400 m	800	1100	2000	3000	40000
Moho ±2 km	800	1100	2000	3000	40000
Moho ±5 km	800	1100	2000	3000	40000
Velocity ±5%	800	1100	2000	3000	40000
Velocity ±10%	800	1100	2000	3000	40000

4.4.1 Sharpness of discontinuities

In order to test how the honouring or non-honouring of the discontinuities would affects the propagations, we create the *"Sharp"* mesh, with about the same number of element as the *REF* but with sharp discontinuities. A zoom of this mesh is shown in Figure 4.4a; to the elements crossing the discontinuities, we assign seismic parameters looking at the position of its barycentre. We perform the simulation of

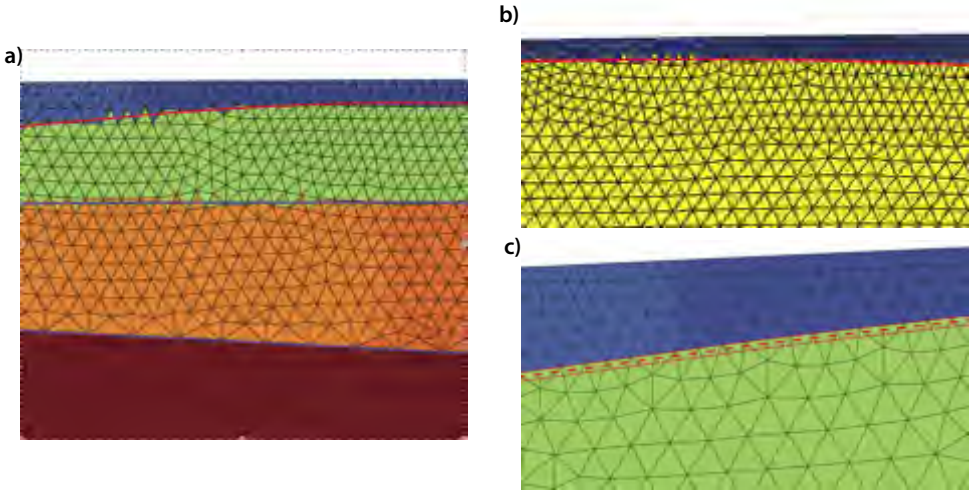

Figure 4.4: (a) Zoom of the *Sharp* mesh, (b) zoom of the *Cutoff 2km sedi* mesh and (c) zoom of the *sedi200* and *sedi400* mesh: the red lines are the shifted location of the sediment interface.

the same source in both *REF* and *Sharp* mesh and we recorded the signal at the same point. From a visual comparison of the low passed signals (Figure 4.5) — using a corner frequency of $0.2, 0.1, 0.08, 0.066, 0.05$ Hz— it is clear that, for surface wave phase, the higher frequencies are the most influenced by meshing approach. Calculating the phase and the envelope misfit and plotting them at receivers and for each frequency range ($0.1 - 0.15$ Hz, $0.08 - 0.1$ Hz, $0.06 - 0.08$ Hz, $0.05 - 0.06$ Hz, $0.041 - 0.05$ Hz) as described in the previous section, we clearly see that both misfits decrease as a function of frequency and they reach low value (less than 0.1) when frequency is less than 0.08 Hz (12 s). For frequency higher than 0.08 we can recognize a correlation of the misfit with the sediment depth, in particular for the horizontal component (U) where the misfit is higher in the regions with a lower the sediment thickness. This is probably due to the fact that in these regions the sediments have low velocities and the material contrast between sediment and upper crust is higher, leading to an increase of misfit as suggest by Pelties et al. (2010).

Moreover, we tested two more meshes of our 2D model: *REF Coarse*, analogous to the *REF* mesh but with larger elements (about one 3 times bigger) and the *Sharp Coarse* with about the same number of element as the *REF Coarse* but with sharp discontinuities. We compare seismograms from both representations with the references. We find that the differences between the two reference meshes are negligible compared to the previous one and the misfit between *REF Coarse* and *Sharp Coarse* shows the same behaviour and values of the *REF-Sharp* comparison. The PM and EM plot for these test cases are not shown here.

We also test a *"Cutoff 2km sedi"* mesh with the same characteristics of the "REF" mesh, but where we do not honour the sediment discontinuities when they

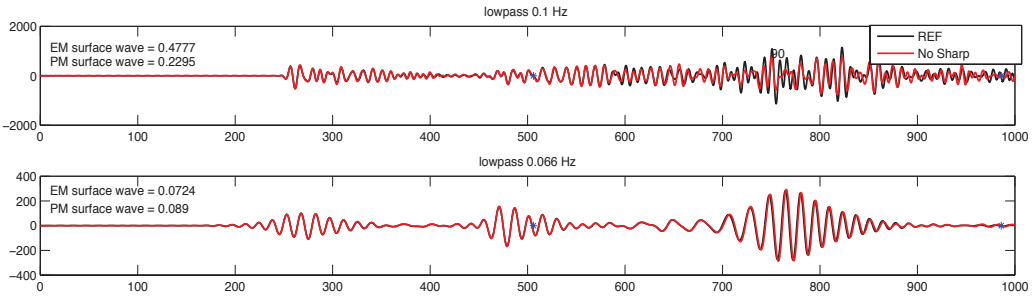

Figure 4.5: Comparison beetwen seismograms (horizontal component) on the "REFERENCE" mesh (black lines) and the "Sharp" mesh (red lines) at receiver 90. The signal are low-pass filtered with corner frequency of 0.1, 0.0666 Hz.

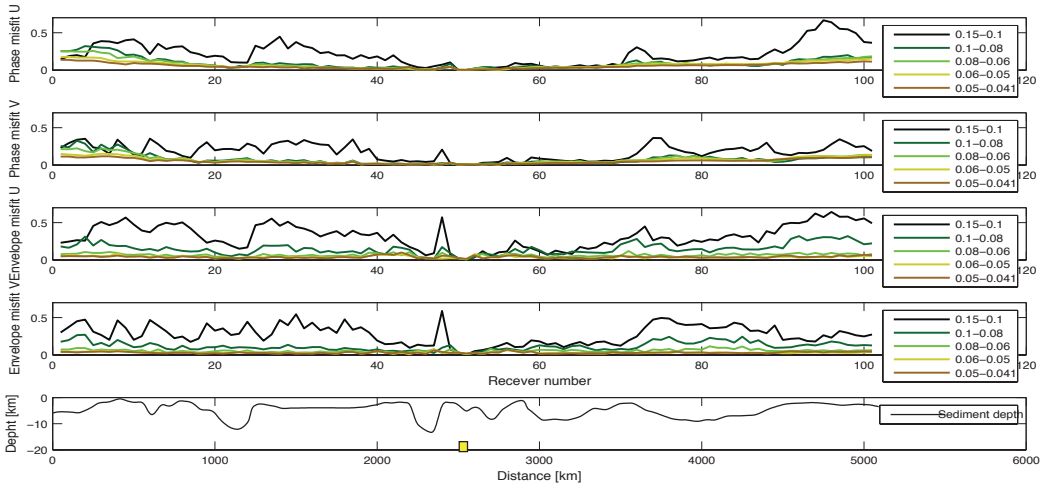

Figure 4.6: Envelope and phase misfit, for the horizontal and vertical component of the surface wave phase, for the "Sharp" mesh with respect to the reference signals calculated in 5 frequency bands: 0.1 - 0.15 Hz, 0.08-0,1 Hz, 0.06-0.08 Hz, 0.05-0.06 Hz, 0.045-0.05 Hz (Kristekova et al., 2009).

are thinner than 2 km (Figure 4.4b). This test was performed in order to have some feeling about the approximation done, for example in SPECFEM3D-Globe, where the sediment layers with a thickness less than 2 km is neglected in the mesh. The PM and EM results (as function of receiver and frequency) show a slight increase of the PM for frequency higher than 0.08 Hz only at the receivers over the sediment region not honoured in the mesh alignment meaning that this moderate approximation is still seen by the waves, but not in our frequency range of interest.

4.4.2 Sediment and Moho depth

Assuming we are able to honour all the discontinuities within the crust, we have to account for a possible perturbed location of the sediment interface and the Moho depth.

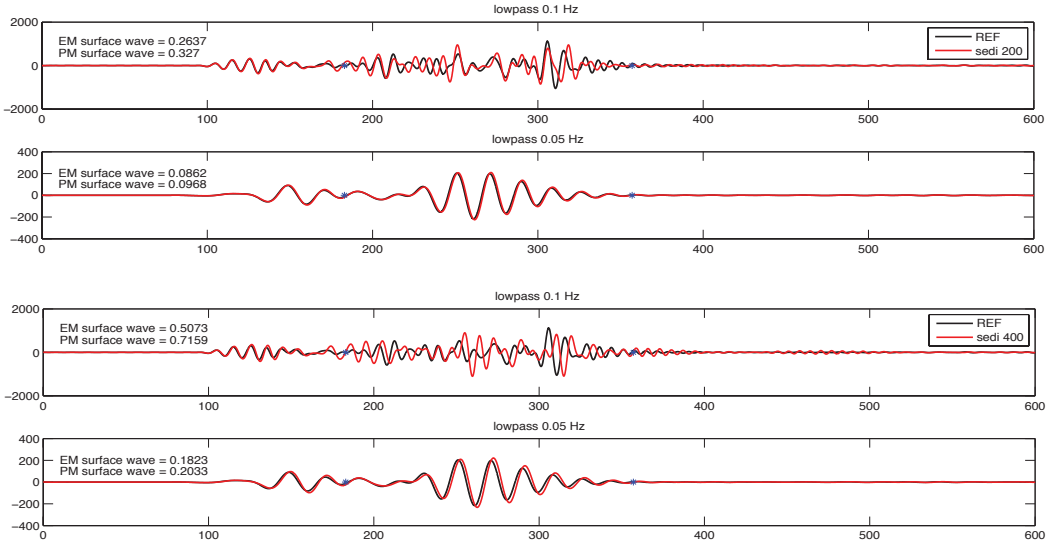

Figure 4.7: Comparison between seismograms (horizontal component) on the "REFERENCE" mesh (black lines) on the "sedi 200" mesh (red lines) (top) and on the "sedi 400" mesh (red lines) (bottom) at receiver 38. The signals are low-pass filtered with corner frequency of 0.1, 0.05 Hz.

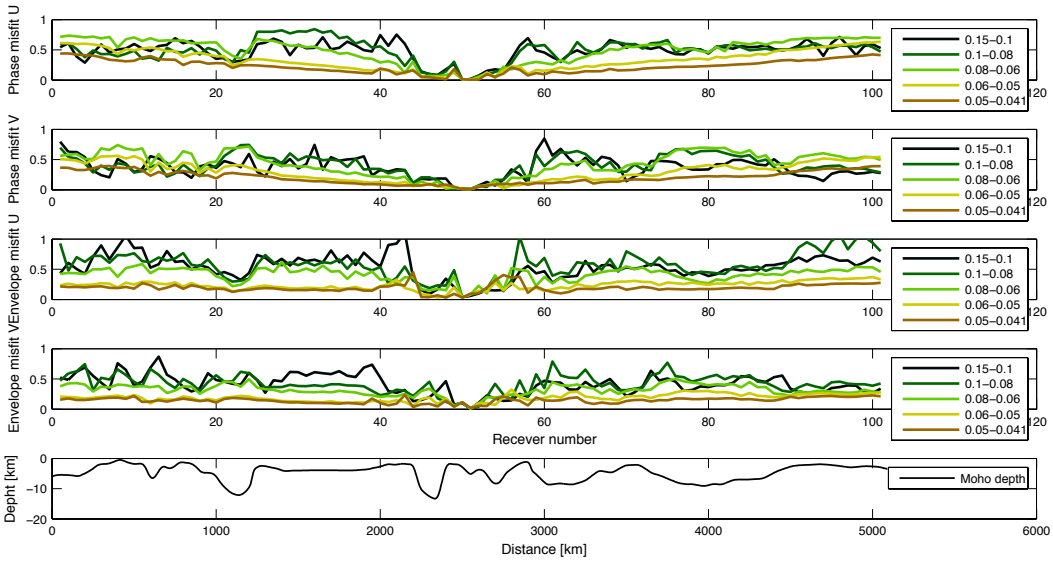

Figure 4.8: Envelope and phase misfit, for the horizontal and vertical component of the surface wave phase, for the "sedi 400" with respect to the reference signals calculated in 5 frequency bands: 0.1 - 0.15 Hz, 0.08-0,1 Hz, 0.06-0.08 Hz, 0.05-0.06 Hz, 0.045-0.05 Hz.

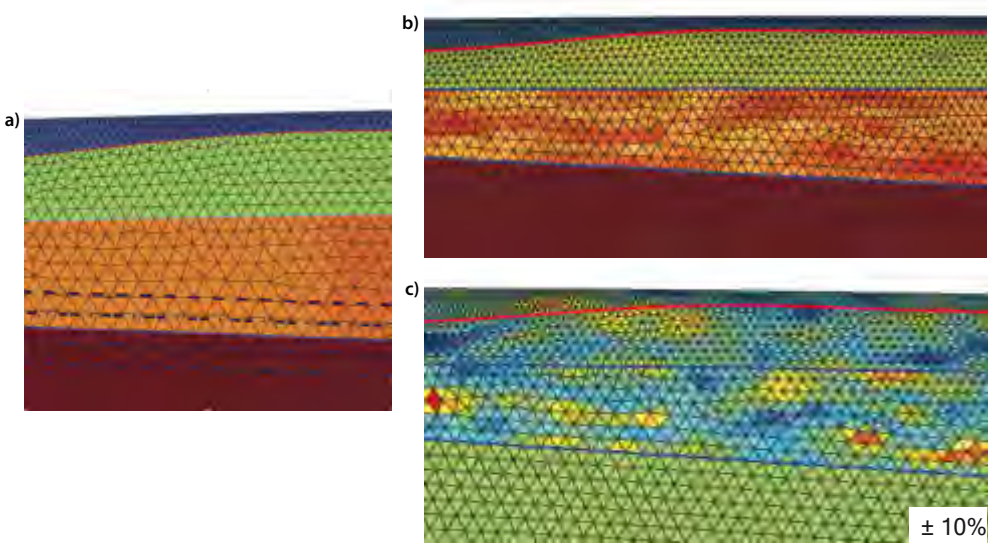

Figure 4.9: Meshes: shallow crustal layer representation

Crustal models are not error-free, and in the best cases, the depth uncertainties are about 5%-10% (but also more). In order to have a feeling of these uncertainties on synthetic seismograms, we consider two test cases in which we shift down the sediment interface by 200 and 400 meters honouring it in the meshes, *sedi200* and *sedi400* meshes (Table 4.2 and Figure 4.4-c). The other interfaces (Moho, Conrad and topography) are fixed as in the *REF* case. In Figure 4.7 we show the horizontal component of the signal at receiver 38, low passed with corner frequency of 0.1 and 0.05 Hz, in *sedi200* (top) and *sedi400* (bottom) test, compared with the reference. Shifting the sediment interface has a much stronger effect than not considering any sediment interface by the mesh. The effect becomes even stronger for a 400 m shift. For high frequency, remarkable envelope and phase differences are noted. Plotting the PM and EM as function of frequency range and receivers (Figure 4.8, for *sedi400* test), we are able to quantify these differences. The PM has an interesting behaviour with distance from the source and frequency: up to 0.08 Hz PM is higher near the source and decrease with distance keeping high values. For frequency lower than 0.08 Hz the misfit clearly increases with the source-receiver distance due to an accumulation of phase delay and the most influenced period are within 12-15 seconds. The EM is remarkable high: the sediment layer is not negligible in wave propagation.

Then we investigate the effect of a perturbed knowledge in the location of one of the most crucial parameter in the description of a crustal model: the Moho depth.

The Moho depth is often know in the models with uncertainties: realistic estimates are within ±5 km or even more (Grad et al., 2009). We create four test cases in which we shift the Moho depth up and down of ±2 km and ±5 km (Table 4.2) in a similar way as for the sediment. A visual inspection of seismograms shows a strong effect of the shift, that becomes stronger in the 5km cases, in particular on

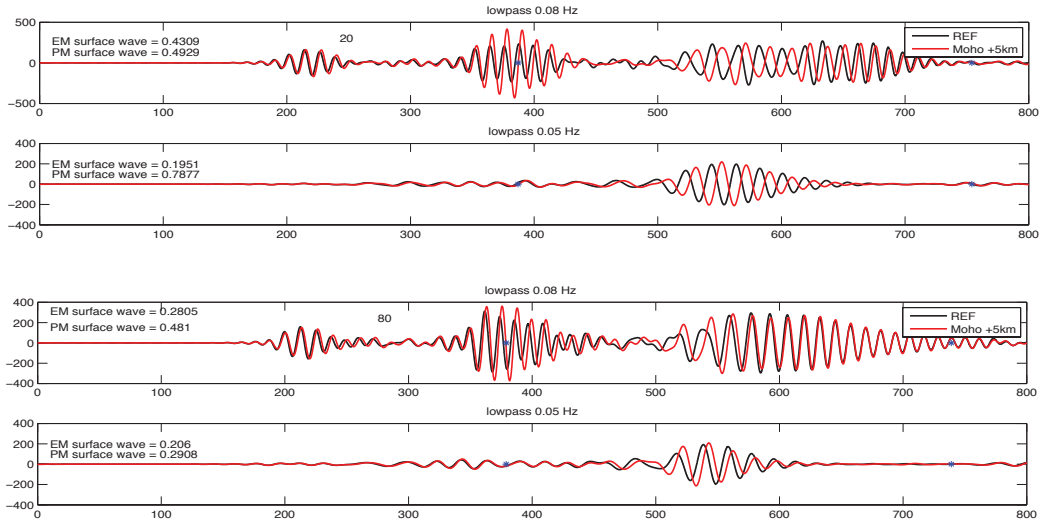

Figure 4.10: Comparison beetwen seismograms (horizontal component) on the "REFERENCE" mesh (black lines) on the "+5km" mesh (red lines) at receiver 20 (top) and 80 (bottom). The signals are low-pass filtered with corner frequency of 0.08, 0.05 Hz.

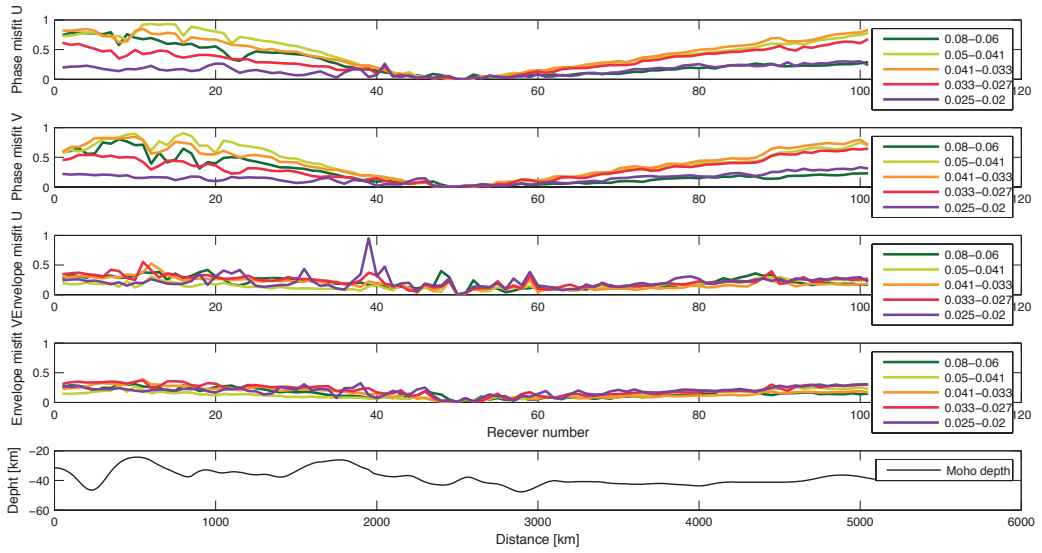

Figure 4.11: Envelope and phase misfit, for the horizontal and vertical component of the surface wave phase, for the +5km with respect to the reference signals calculated in 5 frequency bands: 0.06-0.08 Hz, 0.05-0.041 Hz, 0.041-0.033 Hz, 0.033-0.027 Hz, 0.025-0.02 Hz.

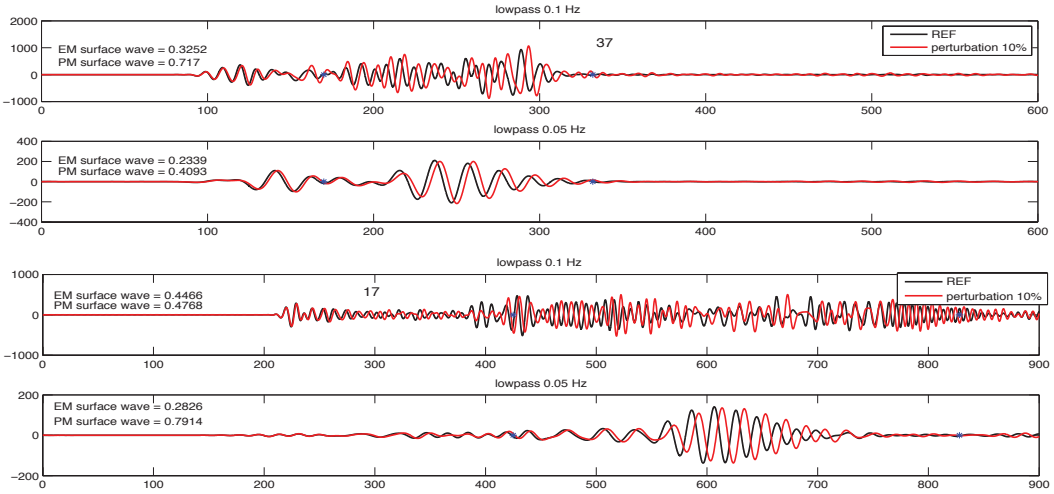

Figure 4.12: Comparison between seismograms (horizontal component) on the "REFERENCE" mesh (black lines) on the "Velocity +10 %" mesh (red lines) at receiver 37 (top) and 17 (bottom). The signasl are low-pass filtered with corner frequency of 0.08, 0.05 Hz.

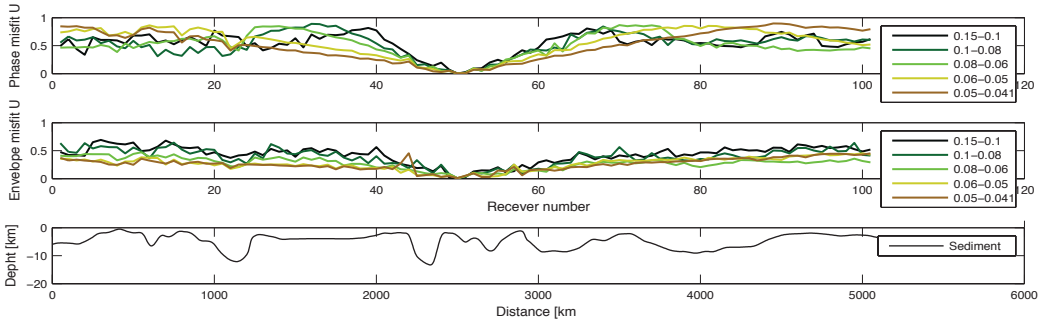

Figure 4.13: Envelope and phase misfit, for the horizontal and vertical component of the surface wave phase, for the "Velocity +10 %" perturbed mesh with respect to the reference signals calculated in 5 frequency bands: 0.06-0.08 Hz, 0.05-0.041 Hz, 0.041-0.033 Hz, 0.033-0.027 Hz, 0.025-0.02 Hz.

the surface wave phase for frequency up to 40 s (Figure 4.10): in some comparisons the phase shift can reach an almost perfect "anti-phase". The effects seem to be negligible for the body wave, at least for the phase misfit. We explore a wider range of frequencies with respect to the other cases (0.1 - 0.15 Hz, 0.08-0,1 Hz, 0.06-0.08 Hz, 0.05-0.06 Hz, 0.05-0.041 Hz, 0.041-0.033 Hz, 0.033-0.027 Hz, 0.025-0.02 Hz) in order to detect differences up to periods of 50 seconds. PM plots for the *Moho5km* case (Figure 4.11) show an interesting frequency dependent behaviour: lowest frequency bands produce the largest errors, and with increasing frequency the errors get smaller. We think that this behaviour is mainly due to the surface waves sensitivity kernels as function of period and depth: for example, 20 s period surface wave are mainly sensitive to structure at 20-30 km depth and 30 s period to 30-40 km depth and so on (see Chapter 1 for the surface wave 1D sensitivity kernels). Looking at Figure 4.11, we see that PM in each frequency band grow as source receiver distance. Moreover the left part of the mesh that has a average Moho depth around 25-35 km has a maximum misfit for frequency around 0.04-0.05 Hz (20-25 s) while the right side, with a Moho depth of about 40-45 km the misfit is maximum in 0.041-0.033 Hz (25-30) range, supporting our explanation. Nevertheless, a part of this effects might be caused by the growing phase shift, until one reaches an almost perfect "anti-phase". For such large phase errors (where the single phases are already too far apart, i.e. be half a cycle or more) the time-frequency misfit criterion could not work properly. The EM is less affected by shifting (lower misfit values) and it does not shows any frequency dependence. This frequency dependence is even clear in the CPM graphic (Section 4.5 and Figure 4.15).

4.4.3 Velocity structure

In order to estimate the severity of the influence of the knowledge of the velocity distribution, we also run 2D test cases with the *REF* model but with slightly perturbed velocity distributions, perturbing the velocity crustal model with a random function with a correlation length of 10 km and amplitude within 5% and 10%. This analysis shows us what errors a wrong velocity distribution will create. A zoom of the perturbed model is show in Figure 4.9-b and the 10% perturbation field is show in Figure 4.9-c. Analysing the PM and EM for the *vel10%* mesh (Figure 4.13) we note that, as in other cases, it increase with the source-receiver distance, but within range of 1000 km from the source the PM increase with the frequency while, out of that limit, show an opposite behaviour: the higher misfit are reach for lower frequency.
The seismograms recorded at receivers in these two different parts of the model are shown in Figure 4.12. The EM, indeed, has the expected behaviour, increasing with the distance from the source and with the frequency. However, for the perturbation of 10%, the misfit values are higher than the *vel5%* case, not shown here.

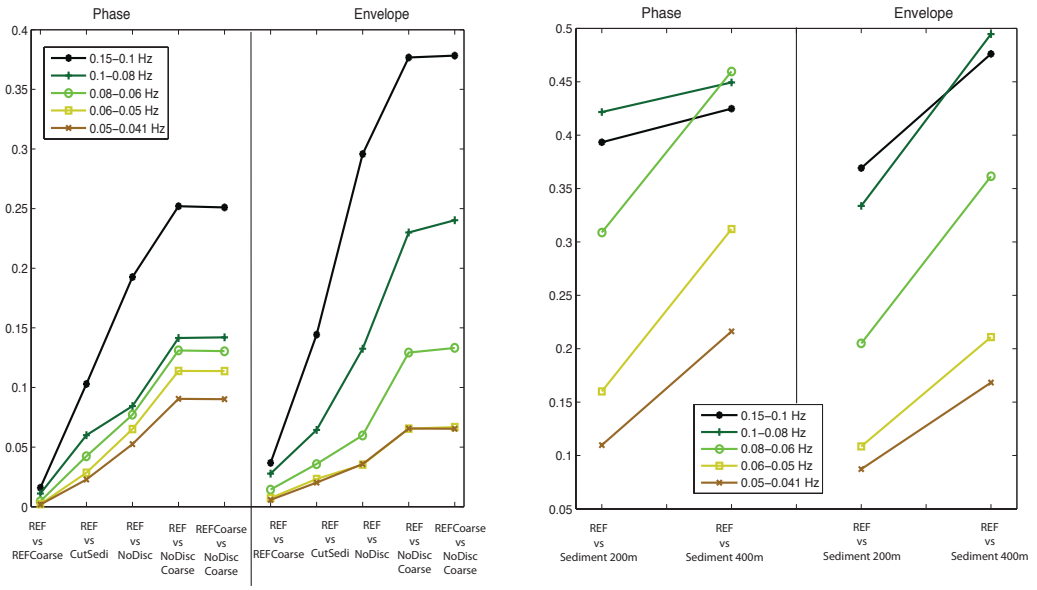

Figure 4.14: Cumulative misfit for the horizontal and vertical component for the sharp tests (left) and for the sediment interface deepening (right). Sum of the Envelope and Phase misfit of surface waves normalized by the number of the receiver times number of component (202). The colour lines are relative to different frequency range in which the misfit is calculated.

4.5 Cumulative Misfit

In order to get a summary of the test cases, we calculate the cumulative phase and envelope misfit for each comparison and for each analysed frequency range, as described in Section 4.3. This would be a summary, telling us how strong is the approximation applied to the reference model. We are now able to define acceptable limits for the misfits. After a careful visual inspection of the seismogram we decide to set the limit for both envelope and phase misfit to 0.25. Looking at the signal, for example in Figure 4.7-bottom, we note a PM of 0.203 that seem still acceptable, while in Figure 4.11 it is around 0.3 that is too much (looking at the seismograms). Similar considerations were done for the EM.

These limits able us to infer which are the most important parameter in defining and representing a crustal model. The sharpness of the discontinuities seem to have a negligible effect with respect to other tested cases. Looking at Figure 4.15-left, it is clear that an uncertainties of ±2 km on the Moho depth is still acceptable for all the frequency ranges, while an error of ±5 km is stronger for the periods shorter than 40 seconds. However the envelope seem to be less affected by the Moho shifting. Of course, to have a Moho shift of 5 km in the whole section is an unlikely case, and in real case the misfit could be less then our results.

Similar conclusions can be find out for the sediment shifting (Figure 4.14-right): for period shorter than 20 seconds and uncertainties of 400 meter is not acceptable.

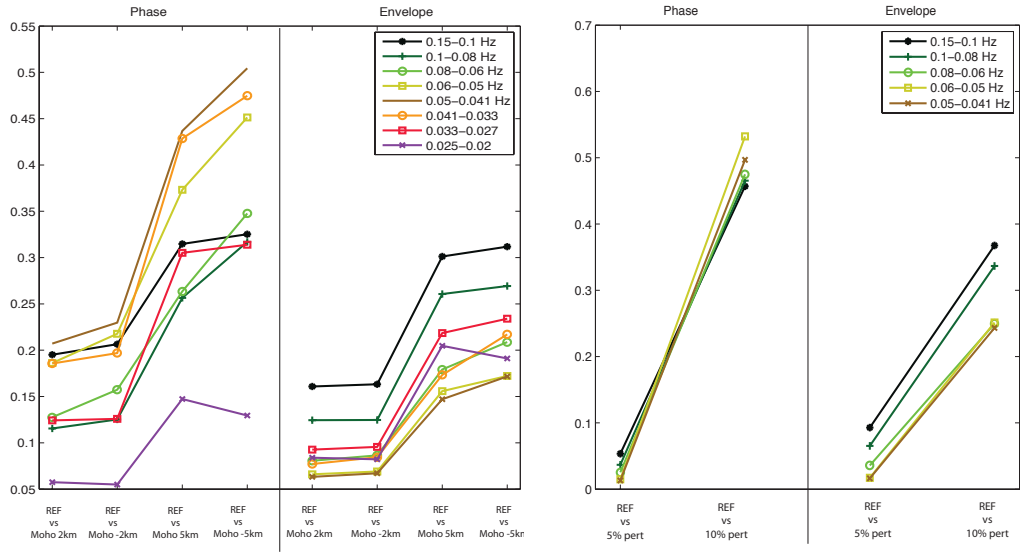

Figure 4.15: Cumulative misfit for the horizontal and vertical component for the Moho shift tests (left) and for the velocity perturbation cases (right). Sum of the Envelope and Phase misfit of surface waves normalized by the number of the receiver times number of component (202). The colour lines are relative to different frequency range in which the misfit is calculated.

Unfortunately, the actual knowledge of the sediment layer is still poor and the error can be of the order of magnitude of kilometers. This means that for also for continental wave propagation studies, in order to reach periods of 20 second the sediment layer has to be know with enough accuracy.

With regard to the velocity test cases (Figure 4.15-right), we can affirm that uncertainties of 5% in the velocity structure is still acceptable and can be neglected, while it is not the same for an error of 10%: the velocity structure has to be known within a 10% uncertainty.

4.6 Conclusion

Knowledge and representation of crustal structure are a crucial point in accurate simulation of seismic wave propagation at continental distance and in this Chapter we quantitatively analysed different representations and different assumptions of knowledge of the structure of a 2D section of EPcrust crustal model. We focused our attention on differences between seismograms from different test cases using the time-frequency misfit criteria by Kristekova et al. (2009). From misfit analysis, we can affirm that current uncertainty in the knowledge of crustal structure (velocity distribution, depth of discontinuities) is more important than geometrical approximations used for numerical simulations at continental distance. As consequence, if our mesh discretization respect the accuracy rules of each numerical method, we

have not to respect the discontinuities in the crust by mesh alignment and in this case most of the errors (mostly phase delay) will be at periods up to 12 second. For longer periods, the shallows discontinuities has not to be honoured. Current uncertainties in the knowledge of crustal structure (velocity distribution, depth of discontinuities) are more important than geometrical approximations used for numerical simulations. Looking at frequency dependence, to use a crustal model with uncertainties on the Moho depth and on the velocity distribution of about ± 5 km and $\pm 10\%$ will affect the wave propagation also at relatively low frequency, for periods up to 40 seconds.

References

Bassin, C., Laske, G., Masters, G., 2000. The current limits of resolution for surface wave tomography in North America. Eos Trans. AGU 81, 48.

Dumbser, M., Kaeser, M., 2006. An arbitrary high-order discontinuous galerkin method for elastic waves on unstructured meshes II. the three-dimensional isotropic case. Geophysical Journal International 167(1), 319–336.

Dumbser, M., Kaeser, M., Puente, J.D.L., 2007. Arbitrary high-order finite volume schemes for seismic wave propagation on unstructured meshes in 2D and 3D. Geophysical Journal International 171(2), 665–694.

Fichtner, A., Kennett, B.L.N., Igel, H., Bunge, H., 2009. Full seismic waveform tomography for upper-mantle structure in the australasian region using adjoint methods. Geophysical Journal International 179(3), 1703–1725.

Grad, M., Tiira, T., Group, E.W., 2009. The moho depth map of the European Plate. Geophys. J. Int. 176(1), 279–292. doi:10.1111/j.1365-246X.2008.03919.x.

Igel, H., Weber, M., 1996. P-sv wave propagation in the whole mantle using high-order finite differences:application to lowermost mantle structure. Geophys. Res. Lett. 23, 415Ð418.

Kaeser, M., Dumbser, M., 2006. An arbitrary high-order discontinuous galerkin method for elastic waves on unstructured meshes i. the two-dimensional isotropic case with external source terms. Geophysical Journal International 166(2), 855–877.

Komatitsch, D., Tromp, J., 2002. Spectral-element simulations of global seismic wave propagation: I. validation. Geophysical Journal International 149(2), 390–412.

Kristekova, M., Kristek, J., Moczo, P., 2009. Time-frequency misfit and goodness-of-fit criteria for quantitative comparison of time signals. Geophys. J. Int. 178(2), 813–825. doi:10.1111/j.1365-246X.2009.04177.x.

Kristekova, M., Kristek, J., Moczo, P., Day, S.M., 2006. Misfit criteria for quantitative comparison of seismograms. Bull. Seis. Soc. Am. 96(5), 1836–1850. doi:10.1785/0120060012.

Molinari, I., Morelli, A., 2011. EPcrust: A reference crustal model for the european plate. Geophys. J. Int. under review.

Pelties, C., Kaeser, M., Hermann, V., Castro, C.E., 2010. Regular versus irregular meshing for complicated models and their effect on synthetic seismograms. Geophysical Journal International 183(2), 1031–1051.

Tesauro, M., Kaban, M.K., Cloetingh, S.A.P.L., 2008. EuCRUST-07: a new reference model for the European crust. Geophys. Res. Lett. 35, L05313. doi:10.1029/2007GL032244.

Chapter 5

Validation of EPmodel: preliminary results

Contents

5.1 Introduction

Itis well known that regional scale wave propagation is strongly affected by shallow structures and the global models do not capture the complex structure of the earth well enough when working at continental or local scale. For the European region, many crust and mantle models are available, the latter mainly from tomography studies using a crustal structure as correction. From a seismologic point of view, an interesting step after developing plausible Earth models, will be to validate the models checking the agreement between real and synthetic seismograms by looking at phase and amplitude differences on the signals. One of the first quantitative comparison of 3-D mantle models at global scale has been done by(Qin et al., 2009) who looked at long period (T $>$ 100 s) surface wave predictions for few earthquakes. Bozdag and Trampert (2010) investigated the agreement between data and long wave- length synthetics obtained by mantle models covering the whole Earth such as S20RTS (Ritsema et al., 1999), PREM, CRUST2.0+PREM, models from Trampert and Spetzler (2006). They investigated both phase and envelope misfit of surface and body waves finding that while a 3D global model is better that a 1D one (looking at the phase), the response of the 3D models are comparable and persist a bias probably due to imperfect crustal correction.

It is important to point out that for regional and continental scale, a crustal model (as well as a mantle model alone) cannot improve the fit itself: it need its coherent mantle (crustal) model beneath (above) it. Once a mantle model is obtained

In collaboration with: Dr. Peter Danececk, INGV Bologna.

using any crustal correction, the two models (crust + mantle) to be considered together. The best way would be to invert data for both crust and mantle structure, but this is still difficult issue due to the high non-linearity dependence of the data on crustal structure and to the measurement problem at high frequency. For these reasons, models of the crust are often assembled using a variety of a priori information — such as we did to create EPcrust – and then used as constraints during seismological inversion for mantle structure. However, we have little direct evidence of the ability of such crustal models to reproduce features on seismograms.

Our purpose here is to go to a validation process of the crustal model we obtained in Chapter 2 in order to understand if EPcrust –that contains more information than the previous models– is able to give a better fit of the real data registered in Europe then previous models. As coherent mantle model, we used the 3D shear-wave velocity model (EPmantle) of the European mantle from surface wave tomography (Schivardi and Morelli, 2011), obtained using EPcrust as constrain to the shallower layers. We computed full synthetic seismograms using a spectral element method, as implemented in SPECFEM3D-Globe (Komatitsch and Tromp, 2002) for two earthquake occouring in the European region. We compare the results with the one obtained using CRUST2.0 (Bassin et al., 2000) and S20RTS (Ritsema et al., 1999). The difference between real data and synthetics at intermediate-long period, are computed in terms of phase and envelope misfit using the criteria proposed by (Kristekova et al., 2009) also applied in Chapter 4.

5.2 Models and implementation in SPECFEM3D-Globe

We implemented two recent seismic velocity models of the European Plate into the seismic wave simulation code SPECFEM3D, in order to calculate and evaluate their response to well recorded earthquakes. We choose *EPmodel* and CRUST2.0 + S20RTS as implemented in SPECFEM3D (Figure 5.1). EPcrust (Molinari and Morelli, 2011) is a crustal a-priori model, a compilation and extension of smaller scale crustal models (derived in Chapter 2). EPmantle (Schivardi and Morelli, 2011) is a radial anisotropic S speed model of the upper mantle obtained from surface wave dispersion curve inversion for a period range of 35 to 200 seconds. It uses EPcrust as a-priori model for the upper most layers and S20RTS mantle model as background model. CRUST2.0 is a global crustal model described in Chapter 1 and 2 while S20RTS is a global shear wave velocity mantle model that incorporates surface wave phase velocities, body wave travel times, and free-oscillation splitting measurements. The CRUST2.0+S20RTS has lower resolution that EPmodel and the latter one highlight more details of the uppermost part of the European region and is expected to give a better fit of real seismograms.

The synthetic seismograms are calculated with SPECFEM3D-Globe (Komatitsch and Tromp, 2002) using a regional configuration with a $90° \times 90°$ model domain, which coincides laterally exactly which the domain of EPmantle (one chunk of a cubed sphere). At the surface, we used elements of approximatively 26 km $\times$ 26 km

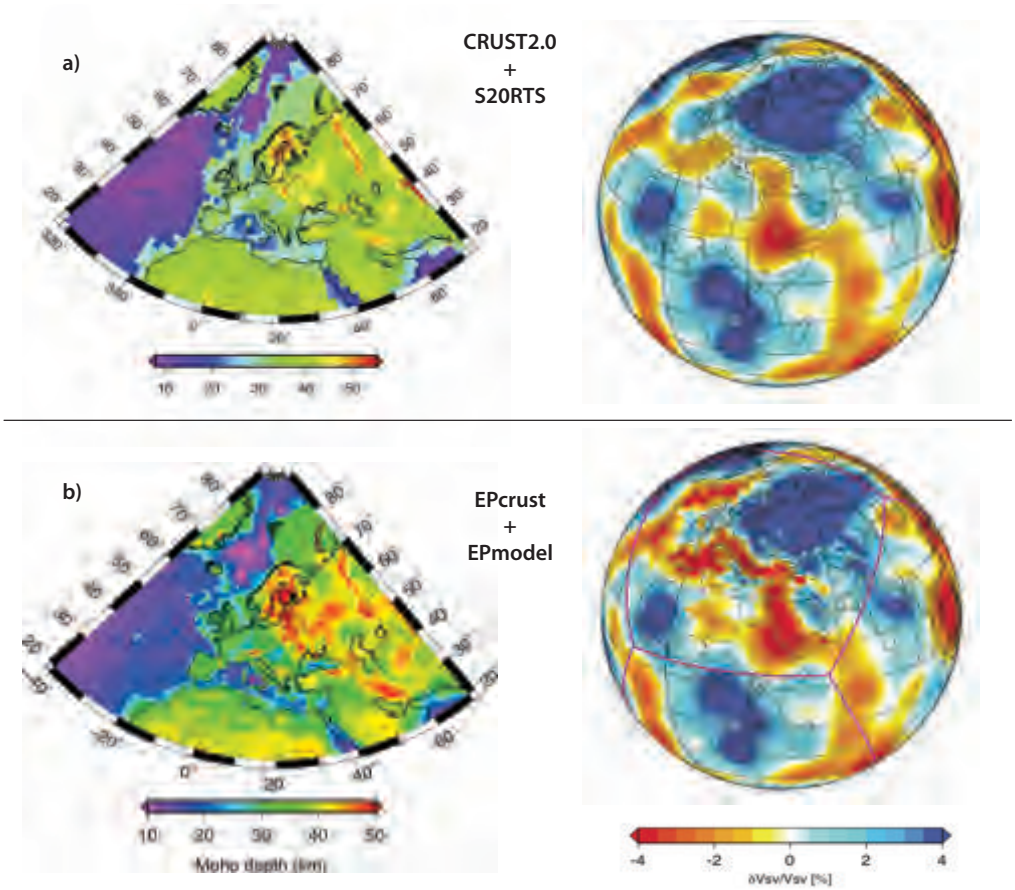

Figure 5.1: Upper panel: CRUST2.0 crustal model Moho depth and (right) S20RTS percent variation of isotropic Voigt average Vs with respect to PREM at 100 km depth. Lower panel: (left) EPcrust Moho depth (Molinari and Morelli, 2011) and (rigth) EPmantle percent variation of isotropic Voigt average Vs with respect to PREM at 100 km depth (Schivardi and Morelli, 2011)

laterally and 10 km in depth; this configuration should provide accurate synthetics to at least 15 s. This is a compromise between computational cost of the simulation and a reasonable shorter period on which are expected to see the improvement due to the new model. The parametrization of EPmodels and EPcrust's detailed topography are implemented in order obtain accurate representation in SPECFEM3D. EPmodel has been implemented modifying the routine *crustal_ model.f90* and *mantle_ model.f90*. We verify the correctness of our implementation plotting the model: in Figure 5.2 it is showed the v_P velocity at 0 km (left) that should give an image of the velocity structure of the sediment and at 20 km (right) depth where we should have an image of the upper-lower crust velocity structure (compare with Fig in Chapter 2). In order to avoid discontinuities in the mesh that could lead to undesired reflections phases, in the areas where EPmodel is not defined, we extend the external region of the model as constant structure to cover the whole mesh (Figure

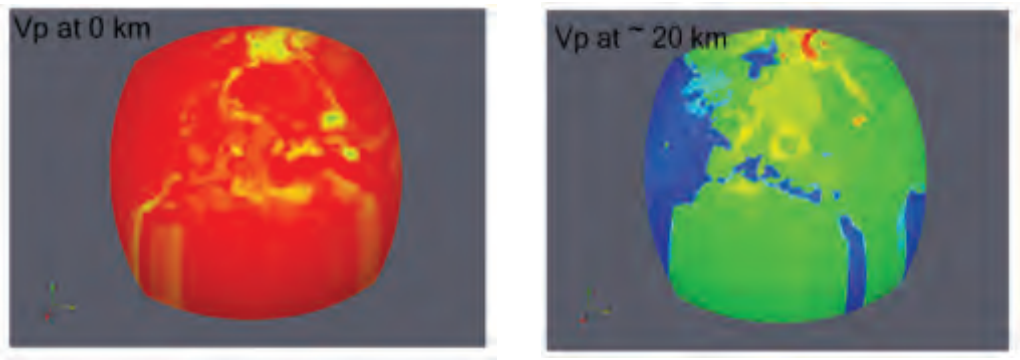

Figure 5.2: Image of v_P at 0 (left) and 20km depth (right) assigned in the element mesh.

5.2). The Moho discontinuities is not honoured in the mesh as well as the inner crustal discontinuities: it is a limit in the resolution of our structure and the reasons for which we are able to analyse only intermediate-long period but still it is a good compromise between resolution and computational cost of the simulations.

Regarding to the earthquake-stations configuration, as first test, we choose two well recorded earthquake: the "Aquila" earthquake occurred in Italy on April 6th 2008 with a magnitude of $M_W = 6.3$ and the "Albania" earthquake occurred on September 6th 2009 with $M_W = 5.4$. The data at the recording stations are taken from the ORFEUS data centre (*http://www.orfeus-eu.org/*). Both stations and earthquake are plotted in Figure 5.3.

5.3 Data analysis and misfit calculations

The two earthquakes were recorded by more that 250 stations in Europe but not all of them presents acceptable signals. We proceed visually inspect and select the records throwing away the ones presenting wrong instrument responses, jumps of the signals, gaps in the record, low signal-to-noise ratio.. We discard 10 % of the originals seismograms.

Then we analyse the long broadband signal selecting limited time-frequency windows to calculate the misfit. We concentrate the attention on direct surface wave arrivals and phase match, as these information were used for the inversion of EPmantle and should be matched well. During the data processing, we first remove the mean and trend, then we taper the signals and low pass filter to both data and synthetics with corner frequency of 0.07 Hz to eliminate the high frequency effects; we select the surface wave phase by an automatic detection based on surface wave velocity (between 2.3 and 4.8 km/s) and the source-station distance. This procedure was applied to both real data and synthetics.

Than we proceed in the misfit calculation. As misfit criteria, we find appropriate the time-frequency criteria presented by Kristekova et al. (2009) that use a wavelet analysis to calculate the energy content of the seismograms as function of time

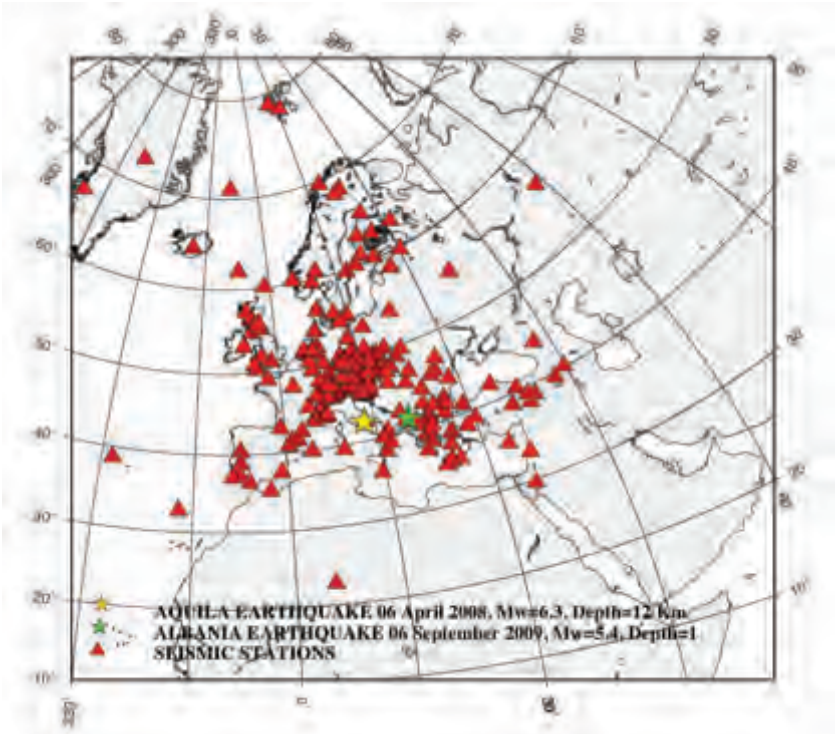

Figure 5.3: The map shows the station from ORFEUS network and the Aquila and Albania earthquakes selected for this study.

and frequency; signal differences are evaluated in this time-frequency space. More information about this criteria can be found in Chapter 4 and in Appendix D. We apply the TF misfit criteria only at surface wave phase and for different period: 15-25 s, 25-40 s, 40-70 s and 70-110 s. The firsts two ranges should be able to detect the crustal structure while the last two are mostly sensitive to the upper mantle structure. In Figure 5.4 an example is shown of the time-frequency analysis of the misfit between the data recorded at OBN station after Aquila earthquake and the synthetic obtained with EPmodel. The power of this criteria lie in the clear representation of the misfit as function of both time and frequency. Moreover the time-frequency misfit can be compress in a single number giving us the possibility to infer on the mismatch between models and data in hundred of stations. Figure 5.4 shows the time-frequency phase misfit (TFPM) while the number in the plot is the phase misfit (PM). When (for a fixed frequency and at fixed time) the reference signal (real, green line) is in advance of phase respect to the other, the colour will be yellow to red otherwise it will be blue. The same is shown for the envelope in the bottom of Figure 5.4, with the difference that yellow to red colours means that the real data has smaller amplitude than the synthetic (for a chosen time-frequency point).

We calculate the PM and EM for any stations (for both earthquake) between the recorded data and the synthetics obtained with EPmodel and CRUST2.0+S20RTS.

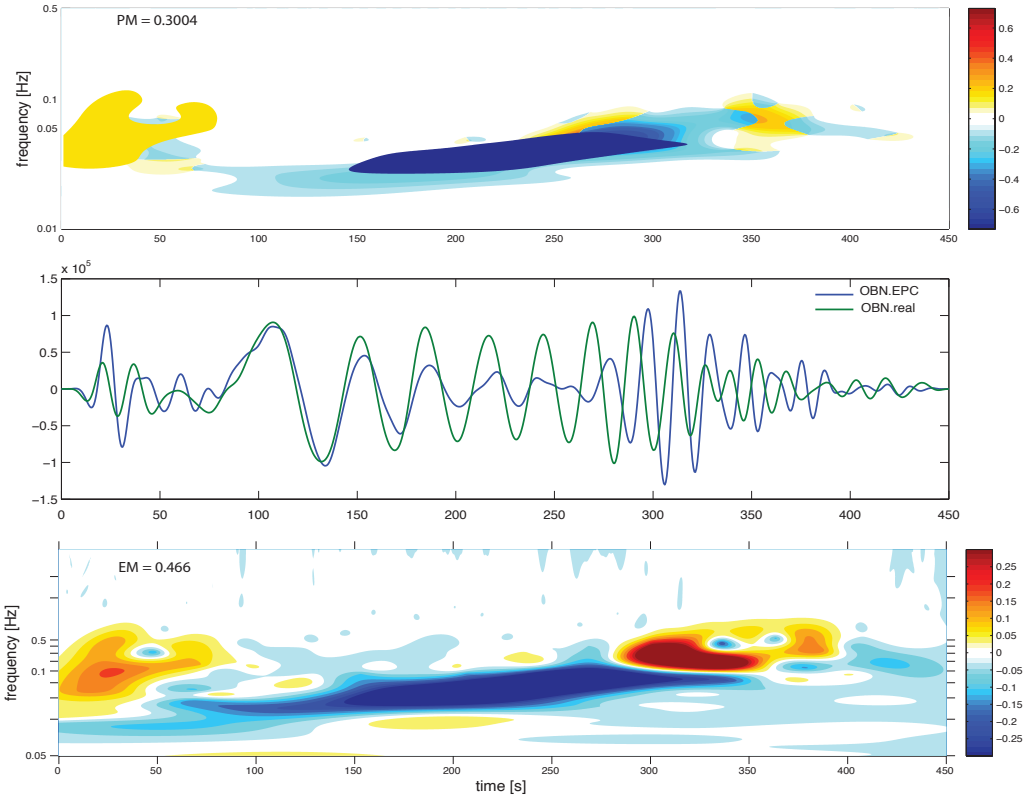

Figure 5.4: Time frequency representation of the phase misfit (top) and envelope misfit (bottom) between seismogram recorded at OBN station and the synthetic signal in EPmodel for the Aquila earthquake.

In the following we will analyse only the PM for simplicity and because the EM has a more difficult interpretation and it will be kept for future analysis.

5.4 Preliminary results and discussion

In order to gauge the quality of the model (better fit of the data), we can first proceed with a visual comparison the seismograms. In Figure 5.5, 5.6, 5.9 we show some of the compared signal. For both earthquake, we note, in most of the stations, a sensible improvement of the fit to full seismograms using EPmantle. With regard to the phase misfit, we notice that, for some station, the two model predict the same phase, not coherent with the real data but in many station EPmodel is more "in phase" then CRUST2.0+S20RTS. In general the synthetics seem to be faster that the real signals. Moreover, most of the difference between real data and both synthetic datasets were found in the T component, in which the energy content is mostly from Love waves, more sensitive to crustal structure. A possible explanation could be found in insufficiently precise knowledge of the crust but also in a bad

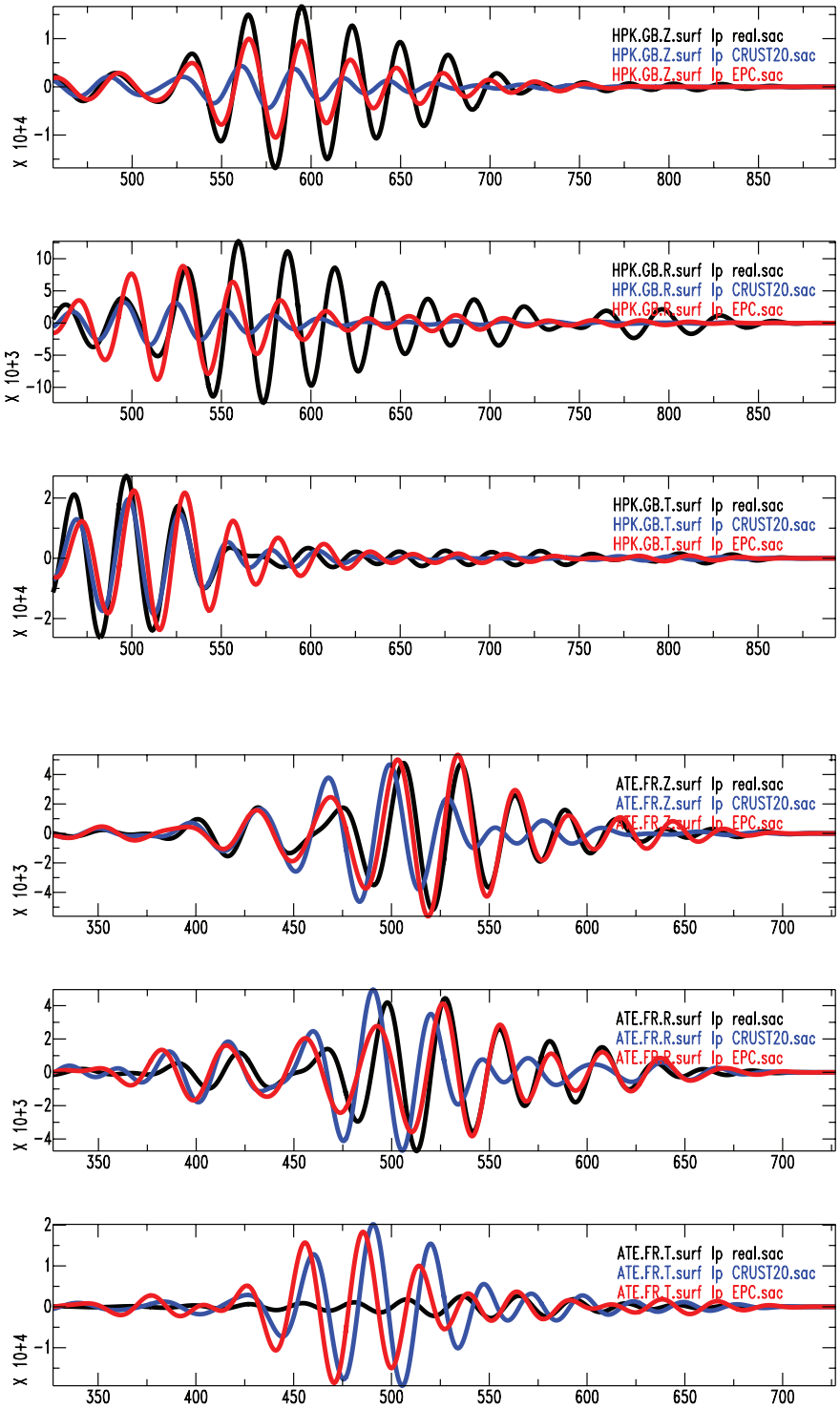

Figure 5.5: Comparison between seismograms —Z, R, T component respectively— recoded at HPK (top) and ATE (bottom) stations during Albania earthquake. Black is the real signal, the blue one is the synthetic obtained using CRUST2.0+S20RTS and the red is the seismogram predicted by EPmodel.

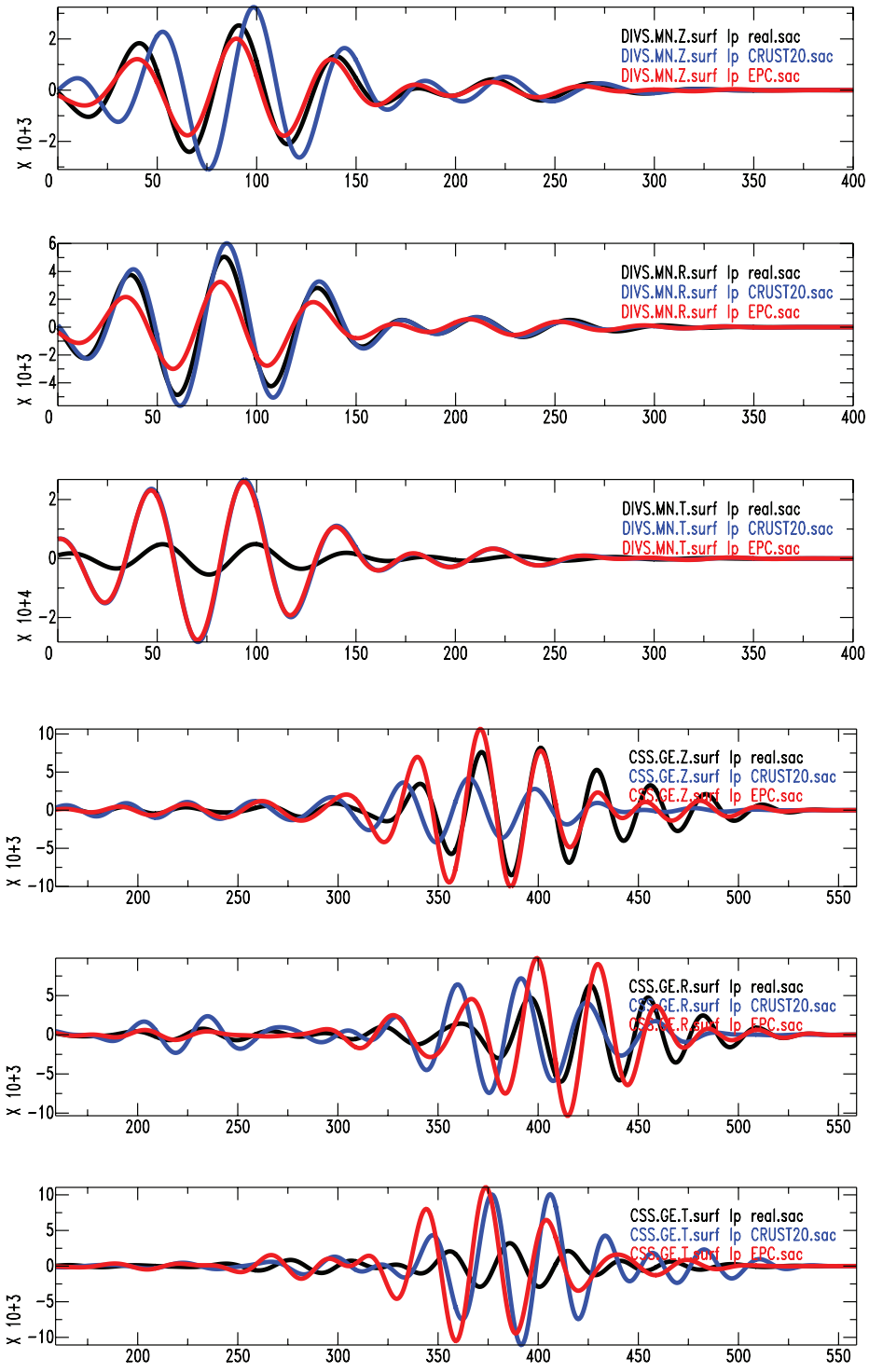

Figure 5.6: Comparison between seismograms —Z, R, T component respectively— recoded at DIVS (top) and CSS (bottom) stations during Albania earthquake. Black is the real signal, the blue one is the synthetic obtained using CRUST2.0+S20RTS and the red is the seismogram predicted by EPmodel.

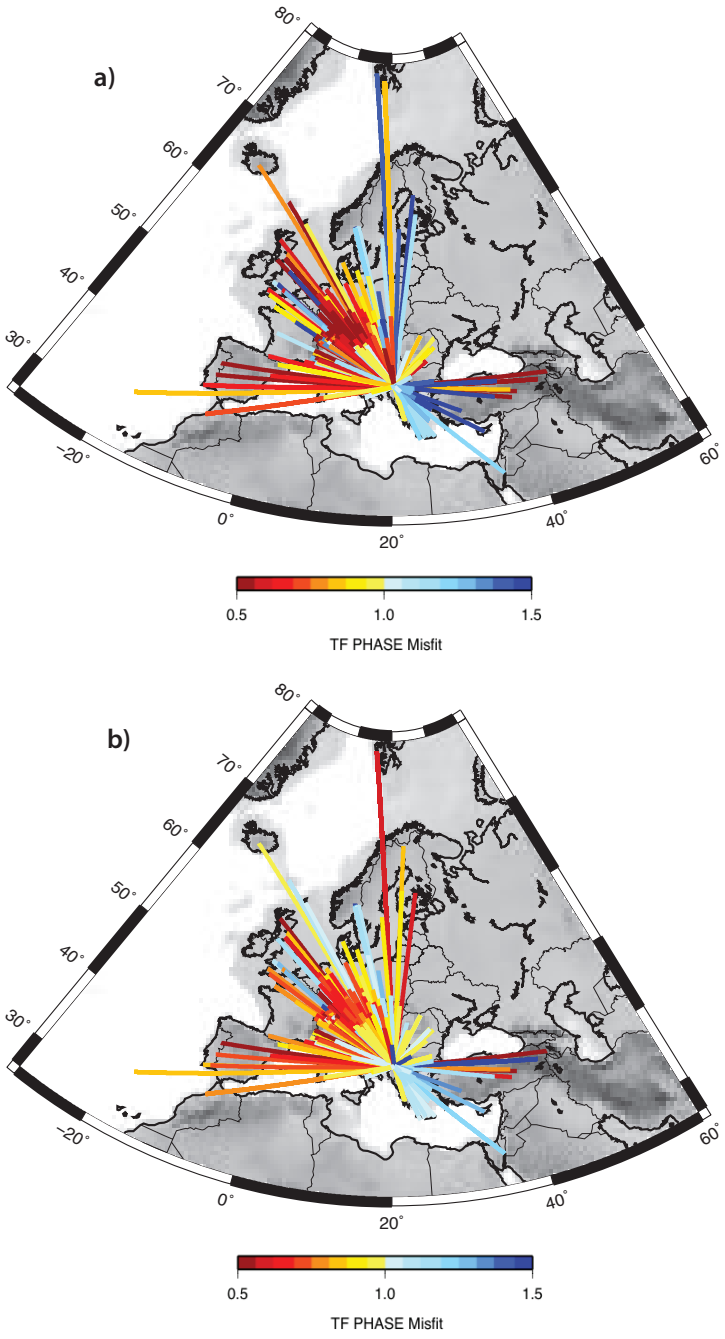

Figure 5.7: a) Ratio between EPmodel PM and CRUST2.0+S20RTS PM on the vertical component: period range 25-40 s. Ratio between EPmodel PM and CRUST2.0+S20RTS PM on the vertical component: period range 40-70 s.

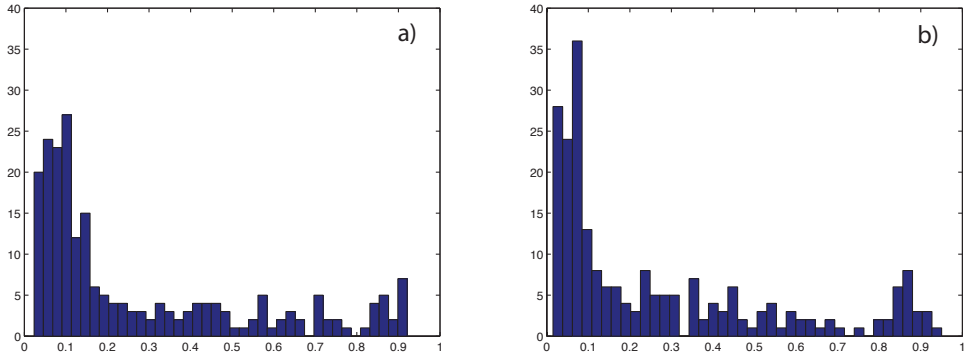

Figure 5.8: Distribution of PM valuse calculated for a period range of 40-70 s for CRUST2.0+S20RTS (left) and EPmodel (right).

description of the structure itself. In some case the amplitude of the synthetics is not fitting well the real data. This is probably due to scattering and a an improper attenuation model in the simulation.

In order to achieve a quantitative analysis on the goodness of the models, we compare the misfit values obtained for the two models. For each source-receiver path we calculate the ratio:

$$q_P = \frac{PM_{EPmodel}}{PM_{CRUST2.0+S20RTS}} \tag{5.1}$$

When q_P is less than 1, EPmodel has a lower PM than CRUST2.0+S20RTS and it fits the data better, the other way round if q_P exceed 1. To retain a geographical distribution of the misfit, we colour each source-receiver path according to the value of q_P. These kind of plots allow us to perform spatial analysis of the improvement of our model respect to CRUST2.0+S20RTS. These "firework" plots for the two earthquakes are shown in Figure 5.7 and 5.10. Moreover, calculating q_P for different frequency range, as we did, we are able to look at the goodness of the model at different depth since higher frequency of the surface wave are more sensitive to the shallower part (and the other way round). From Figure 5.7, for periods between 25 and 40 s (mostly sampling the crust) and 40 and 70 s (sampling the upper mantle) we can affirm that, for the Albania earthquake, the Central and Easter Europe have a structure that is able to fit the data better than S20RTS. This is not the case for the Aquila earthquake where, for short path, EPmodel presents some problems. Is it important to consider that also the choice of source parameters (location, CMT) can impact on result as described in Ferreira and Woodhouse (2007) and probably, this could be the case.

In order to detect the general behaviour of the two models tested, we plot in a histogram the distribution of the PM values over all the path for a period range of 40-70 s for the Albania earthquake. EPmodel (Figure 5.8-right) shows a narrower distribution near zero with respect to CRUST2.0+S20RTS. These first results

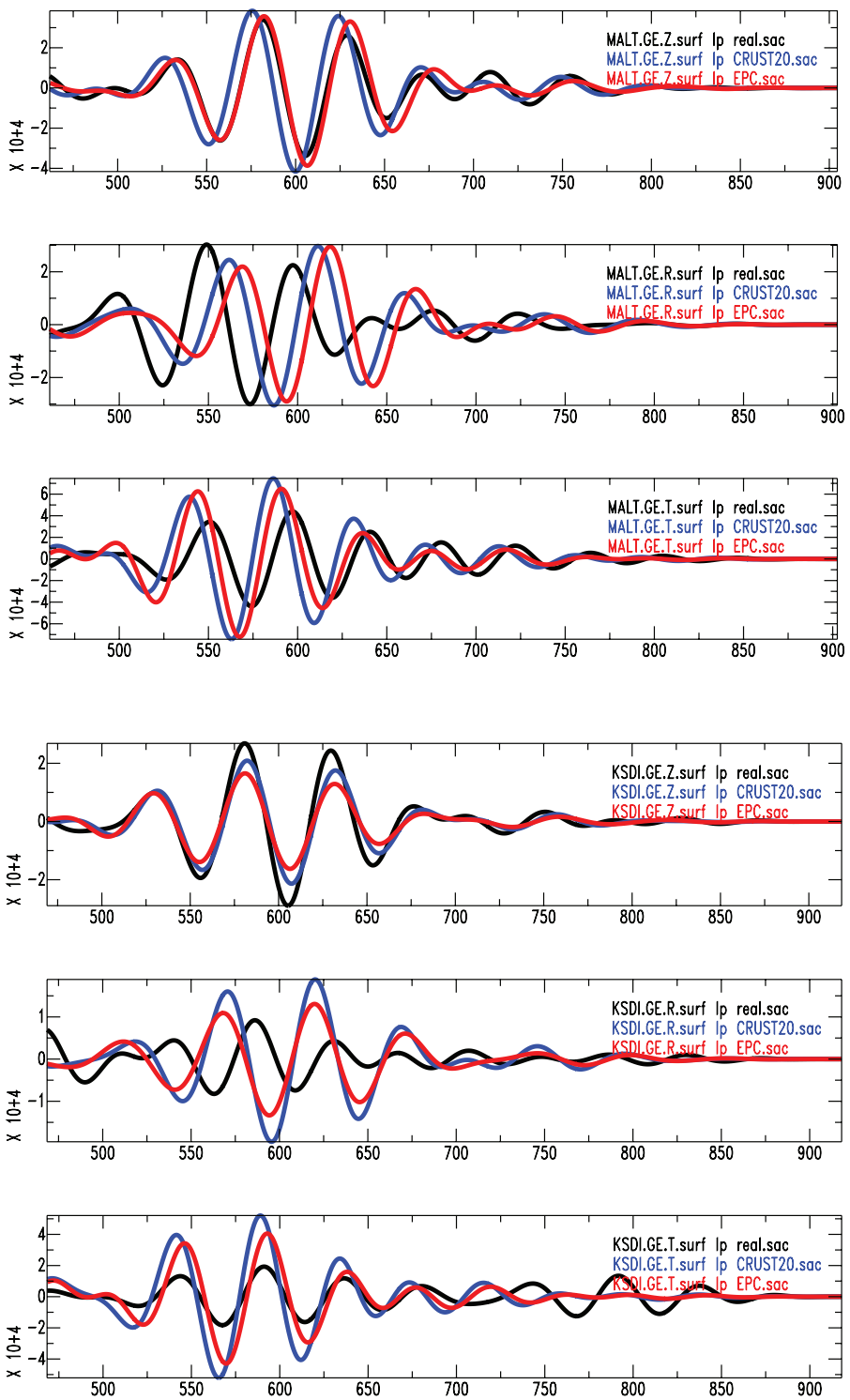

Figure 5.9: Comparison between seismograms —Z, R, T component respectively— recoded at MALT (top) and KSDI (bottom) stations during Aquila earthquake. Black is the real signal, the blue one is the synthetic obtained using CRUST2.0+S20RTS and the red is the seismogram predicted by EPmodel.

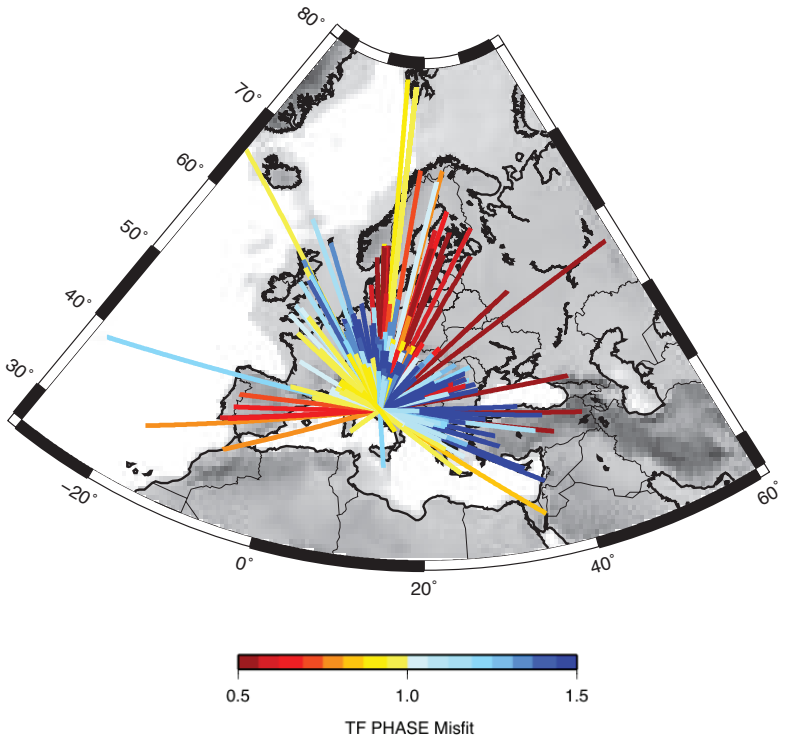

Figure 5.10: Ratio between EPmodel PM and CRUST2.0+S20RTS PM on the vertical component: frequency range 40-70 s.

suggest us that EPmodel is a better candidate in the description of the European structure.

Of course, a more detailed analysis overall the frequency ranges and the simulation of many more earthquakes are required in order to get more robust results.

5.5 Conclusions and future work

In this chapter we lay the foundation for a systematic quantitative assessment of EPmodel (EPcrust + EPmantle) with respect the real data. The analysis of the behaviour of different models is done on different frequency ranges separating the effects on the phase and the envelope. Moreover, looking of the misfit along the ray path, we are able to retain geographical information letting us to identify critical regions of the models.

From this preliminary results we can affirm that EPmodel improves the fit to full seismograms but not to all seismograms. Despite the preliminary results are promising, we found some limitations and few consideration should be done. As pointed out in previous chapters, the representation of the shallowest part of the structure plays an important role on simulated waveforms; also the smoothing technique is

important in the resulting synthetic seismograms. A more accurate implementation of the crust in SEM meshes should be achieved. Important improvement are now available in the new version of the SPECFEM3D-Globe code: most of the Moho interface is now honoured in the mesh, representing the crustal structure in a more appropriate way.

Moreover, it is very difficult to find a simple measure of quality of models. The measure of differences between large portion of seismograms is getting an important issue, together with the improvement of the 3D full waveform inversion technique (Fichtner et al., 2009; Tape et al., 2010). Difference over time, root mean square, cross correlation, multi-taper measurement are all possible measures. Here we applied the TF misfit proposed by Kristekova et al. (2009) and we select the surface wave phase in a very simple manner but other misfit criteria and windows selection are available such as FLEXWIN (Maggi et al., 2009). Moreover, many choices are possible to compress an elaborate measure (phase, envelope vs. frequency) into a single number and it can influence the results. Will be important to check when the possible misfit criteria do not coincide with intuitive judgement of good fit.

Other different elements concur to complicate the picture: data quality of real seismograms can bias the assessment, the choice of source parameters (location, CMT) can impact on results at pointed out in Ferreira and Woodhouse (2007) and the earthquakes should be correctly re-localized in the current model.

References

Bassin, C., Laske, G., Masters, G., 2000. The current limits of resolution for surface wave tomography in North America. Eos Trans. AGU 81, 48.

Bozdag, E., Trampert, J., 2010. Assessment of tomographic mantle models using spectral element seismograms. Geophys. J. Int. 180(3), 1187–1199. doi:10.1111/j.1365-246X.2009.04468.x.

Ferreira, A., Woodhouse, J., 2007. Source, path, and receiver effects on seismic surface waves. Geophys. J. Int. 168, 109Ð132.

Fichtner, A., Kennett, B.L.N., Igel, H., Bunge, H., 2009. Full seismic waveform tomography for upper-mantle structure in the australasian region using adjoint methods. Geophysical Journal International 179(3), 1703–1725.

Komatitsch, D., Tromp, J., 2002. Spectral-element simulations of global seismic wave propagation: I. validation. Geophysical Journal International 149(2), 390–412.

Kristekova, M., Kristek, J., Moczo, P., 2009. Time-frequency misfit and goodness-of-fit criteria for quantitative comparison of time signals. Geophys. J. Int. 178(2), 813–825. doi:10.1111/j.1365-246X.2009.04177.x.

Maggi, A., Tape, C., Chen, M., Chao, D., Tromp, J., 2009. An automated time-window selection algorithm for seismic tomography. Geophysical Journal International 178(1), 257–281.

Molinari, I., Morelli, A., 2011. EPcrust: A reference crustal model for the european plate. Geophys. J. Int. under review.

Qin, Y., Capdeville, Y., Montagner, J.P., Boschi, L., Becker, T.W., 2009. Reliability of mantle tomography models assessed by spectral element simulation. Geophys. J. Int. 177, 125Ð144. doi:10.1111/j.1365-246X.2008.04032.x.

Ritsema, J., Van Heijst, H., Woodhouse, J.H., 1999. Constraints on the correlation of p- and s-wave velocity heterogeneity in the mantle from p, PP, PPP and PKPab traveltimes. Science 286, 1925 – 1928.

Schivardi, R., Morelli, A., 2011. EPmantle: a three-dimensional transversely isotropic model of the upper mantle under the European Plate. In press Geophys. J. Int. .

Tape, C., Liu, Q., Maggi, A., Tromp, J., 2010. Seismic tomography of the southern california crust based on spectral-element and adjoint methods. Geophysical Journal International 180(1), 433–462.

Trampert, J., Spetzler, J., 2006. Surface wave tomography: finite-frequency effects lost in the null space. Geophys. J. Int. 164, 394Ð400.

Conclusions

This study addresses the structure of the European crust with the main purpose of modelling seismic wave propagation. An accurate account for the true composition and constitution of the Earth's crust is indeed a crucial point in many geophysical applications such as simulation of the propagation seismic waves, tomography of the mantle, geodynamics calculations, gravity studies. Given the limitations of current large-scale models, and their approximate account often made, a detailed study focused on improving the definition of the crust in the European domain — and addressing effects of approximations — appeared well motivated.

We started analysing the influence of crustal structure on surface wave dispersion and 1D sensitivity kernels. As a preliminary test, we took into consideration the most widely used global crustal model (CRUST2.0) and by applying surface wave dispersion curve matching, we calculated models with uniform, constant-thickness layers that reproduce the seismological behaviour of CRUST2.0, at the same time allowing a substantial decrease in complexity in the description of the model. We tested the performance of the equivalents models using the SPECFEM3D-Gobe code (Komatitsch and Tromp, 2002) without find a significant degradation in the synthetic seismograms. This experiment gave us confidence that, indeed, a rather simple set of parameters may suffice to describe crustal structure well enough to model long and intermediate-period seismograms.

Focusing on a continental scale, in particular on Europe, with the purpose of running realistic 3D earthquake simulations, it became clear that current crustal models are not fully adequate for modeling regional datasets with the desired detail. We noted a remarkable lack of detail in knowledge of crustal structure even at regional scale. Although surface waves are very sensitive to crustal structure, they are not able to discriminate well between crust and the uppermost part of the mantle. This makes them impractical to be used for large-scale tomographic imaging of the continental crust. More recent studies on noise tomography show an improved capability to detect shallow structure but they are still limited to local results. We overcome this gap developing a new crustal model of the European plate (EPcrust). It is based on critical assemblage of information and previous models of European crustal structure. It includes recent studies and has some important advantages with respect to previous models: it covers the whole European plate; it is a complete and internally-consistent model; with all the seismic parameters provided; it incorporates most of the recent result concerning the European crust; it is easy to update by adding new contribution; it is reproducible, and it is available in an exchange digital format.

At more local scale, in the Easter Alpine region, we created a regional crustal model from 37 2D seismic profiles taken from the literature Along these lines we set up geo-referenced datasets of the main crustal parameters (thickness of sediments, depths to Conrad and Moho interfaces, P-/ S-wave speed and density profiles). We

incorporated all these data into a complete and continuous crustal model of the Eastern Alpine crust applying a geostatistical kriging algorithm. Due to its parameterization, its inclusion in continental models, such as EPcrust was straightforward, and this could be seen as an instance of the possibility of include more detailed local information in the European-scale compilation.

EPcrust, the Eastern Alpine EA1.0 model, the Moho map and the collected seismic lines are all available at *www.bo.ingv.it/eurorem/EPcrust/*. All our results can therefore be easily inspected and reproduced.

Both models — EPcrust and EA_01 — are well suited for use at the European scale for a variety of research topics, including: wave propagation modeling at continental scale, crustal correction in tomography, gravity studies, dynamic topography inferences and so on. EPcrust has been used, in other works, as crustal correction in mantle surface wave tomography –EPmantle (Schivardi and Morelli, 2011)– and in gravity studies for mantle structure showing a better behaviour than to previous models.

Since our initial purpose was to simulate realistic seismic wave propagation with numerical methods (such as ADER-DG and SEM) in the European region, we then studied the behaviour of synthetic seismic wave-fields as a function of representations of the shallower structure with varying accuracies. The creation of a mesh (at continental scale) able to honour all the discontinuities in the crust is possible, but is problematic because of the high computational costs of the simulations. Recents works point out the importance of the representation of crustal structure: a completely neglectfulness of the crust in the mesh, or designing coarse meshes that do not honour the crust model discontinuity interfaces, will lead to a lack in the solution accuracy (Capdeville and Marigo, 2008). Following this kind of approach, we performed simulation cases in a 2D slice of EPcrust, testing different representation of the crustal structure. We used the ADER-DG method as implemented in the SeisSol code (Kaeser and Dumbser, 2006). We investigated also cases in which we perturbed the most important parameters of a crustal model such as sediment and Moho interface depth and velocity structure. We found that, respecting the accuracy rules of numerical methods, the current uncertainties in the knowledge of the model are more important than approximations commonly made in representation in the mesh. Such limitations mostly affect high frequency surface waves. The actual uncertainties on which available crustal models are given, can influence the solution for periods as short as 30-40 seconds. These tests should help us to construct a more efficient 3D mesh to represent Europe. We note that using the very accurate ADER-DG method at continental scale is still too expensive.

To validate the new EPcrust model we need to check the agreement between real and synthetic seismograms. We found the best compromise between accuracy and computational costs in the SEM method — as implemented in the SPECFEM3D-Globe code (Komatitsch and Tromp, 2002). We conducted a systematic quantitative assessment of EPmodel (EPcrust + EPmantle) with respect the real data using a time frequency misfit criterion. From the results we achieved, we can affirm that EPmodel improves the fit to full seismograms. We plan to continue these analy-

sis, improving the representation of the shallower part of the model in the meshes, simulating more earthquakes in order to get wider datasets, and applying different misfit criteria and phases windows selection. We are confident in getting more robust results and thus completely validate EPmodel in a wave propagation point of view.

In this work I highlighted the importance of the knowledge and representation of the crustal structure from a seismological point of view. Plausible models and their representation are fundamental for realistic wave propagation simulations and as a starting point in 3D waveform inversions. We think that EPcrust represents an advancement over previous knowledge, but the issue is still open. The model could be improved as new high-quality descriptions of the European crust become available — including new,higher resolution models resulting from, e.g., seismic noise studies, new refraction-reflection seismic experiments or receiver function results.

Accurate knowledge of the structure, however, needs to be paired with an accurate representation in a computational meshes, and an appropriate numerical method. While we can conclude that spectral-element codes — that are efficient but smooth thin-layer discontinuities within shallow computational elements — can conveniently employed when working at a scale of thousands of km, more accurate — but increasingly computer-intensive — meshes, such as tetrahedral ones implemented in DG codes, may be needed to increase the seismic frequence as, for instance, needed to analyze the response of local structures for seismic hazard studies.

More realistic earthquakes simulations could be obtained using our 3D models as crustal structure. I plan to perform realistic wave propagations at more regional and local scales. A systematics studies on the 3D representation of the crust in numerical methods could improve the understanding on 3D crustal structure and wave propagation.

References

Capdeville, Y., Marigo, J., 2008. Shallow layer correction for Spectral Element like methods. Geophys. J. Int. 172(3), 1135–1150. doi:10.1111/j.1365-246X.2007.03703.x.

Kaeser, M., Dumbser, M., 2006. An arbitrary high-order discontinuous galerkin method for elastic waves on unstructured meshes i. the two-dimensional isotropic case with external source terms. Geophysical Journal International 166(2), 855–877.

Komatitsch, D., Tromp, J., 2002. Spectral-element simulations of global seismic wave propagation: I. validation. Geophysical Journal International 149(2), 390–412.

Schivardi, R., Morelli, A., 2011. EPmantle: a three-dimensional transversely isotropic model of the upper mantle under the European Plate. In press Geophys. J. Int. .

Appendix A

Geostatistic methods

A.1 Introduction

In this appendix we illustrate the main concepts behind the kriging method and the geostatistical theory applied in Chapter 3. The specific kriging application is to make regular grid from not regular sampled point of a spatial variable such as depth of interfaces, density, porosity etc.. Kriging produces maps that have statistically optimal properties and it is an exact interpolator since the value estimated by kriging is exactly the same as the observation at the same locations.
The main references for this appendix are Davis (2002), Remy et al. (2009), Olea (2009) and Yamamoto (2000).
In our geostatistical applications, we use the Stanford Geostatistical Modeling Software, SGeMS, (Remy et al., 2009) that is the state-of-the-art for the geostatistical software package. The software code available at from "http://sgems.sourceforge.net". The code is in C++ and runs interactively under Windows.

A.2 Geostatistic

Geostatistics is a branch of applied statistic originally developed by Georges Matheron (Fontainebleau, France). "It's an abstract theory of statistical behavior" and it is applicable in different areas of geology and natural science.

The key concept is the "regionalized variable" (that have properties between truly random and completely deterministic variable). A regionalized variable has geographic distribution, is spatially continue but it can not be describe by any tractable deterministic function. We know its value only at sample points, $Z(\mathbf{x})$ (Davis, 2002). Geostatistics involves estimating the form of a regionalized variable. For the characterization of variable's spatial attributes, geostatistics uses probabilistic models (which are used for spatial data in a manner similar to the way in which time-series analysis characterizes temporal data), or pattern recognition techniques (Olea, 2009).

A basic statistical measure of geostatistics is the *'semivariance'*, which is used to express the rate of change of a regionalized variable along a specific orientaton. Semivariance is the measure of the degree of spatial dependence between observations along a specific direction. If the observations (n) are uniformly spaced align a straight line, the semivariance (γ_h) can be estimate as (Davis, 2002):

$$\gamma_h = \frac{\sum_i^{n-h}(x_1 - x_{i+h})^2}{2n} \tag{A.1}$$

where h is the number of intervals (e.g. two intervals away from i-location), x_i is a measurement of regionalized variable at location i and x_{i+h} is a measurement of regionalized variable at location $i+h$. For example, for $h = 2$, every point is compared to a point two spaces away, and so forth.

If the semivariance for different values of h is calculated, it is possible to plot the result in the form of a "semivariogram" (analogous to a correlogram). This data-based semivariogram is called *'experimental semivariogram'* (an example is shown in Figure A.2), to distinguish it from the *'theoretical semivariogram'* that characterize the underline population and usually it is a smooth function represented by a model equation. When Δh is small, the distance between the points to be compared tend to be very similar and γ_h will be small. When Δh increase, the point being compared are less and less related to each other and their difference became large, resulting in large γ_h. At some distance, the point being compared are independent to each other and the semivariance is equal (in magnitude) to the variance around the average value: the semivariogram is flat in this region (sill). The region of the semivariogram in which the semivariance approach the variance is called *range* of the regionalized variable. The *range* define a neighborhood: in this region all locations are related to one another. If the regionalized variable is stationary (same average value everywhere), any locations outside the neighborhood region are completely independent from the central point. Within the neighborhood, the regionalized variable at any locations is related to the regionalized variable in the central point. From a number of observations made within the neighborhood, we can estimate the regionalized variable in the central point using the semivariogram. The semivariance can also be defined as (Davis, 2002):

$$\gamma_h = \frac{\sum_i^{n-h}[(x_1 - x_{i+h})^2 - \sum_i^{n-h}(\frac{x_i - x_{i+h}}{n})]}{2n} \tag{A.2}$$

Under the hypothesis of stationary (same average value everywhere), the second term at numerator is zero, but, if the regionalized variable is not stationary (the mean of the sequence change with h), $\frac{\sum(x_i - x_{i+h})}{n}$ has some value. We can not compute the semivariogram anymore. Actually, a general (not stationary) regionalized variable is composed of two parts: the residual and the *drift*. The *drift* is the expected value of the regionalized variable at one point i (or a weighted average of all the points in the neighborhood around the point i). If the drift is subtracted from the regionalized variable, the residual, $R_i = x_i - X_i$, became a regionalized variable itself, with local mean equal to zero. The residual will be stationary and it will be possible to compute the semivariogram. If the regional variable is not stationary, we are in a loop (to estimate the drift we need to know the neighborhood size and the weight to assign at points, to know the weight we need the seimvariance). It is needed to relax the definition and follow a trial and error procedure. From now, neighborhood is a confident interval in which all location are related to the other. In the neighborhood, the drift can be approximated as (Davis, 2002):

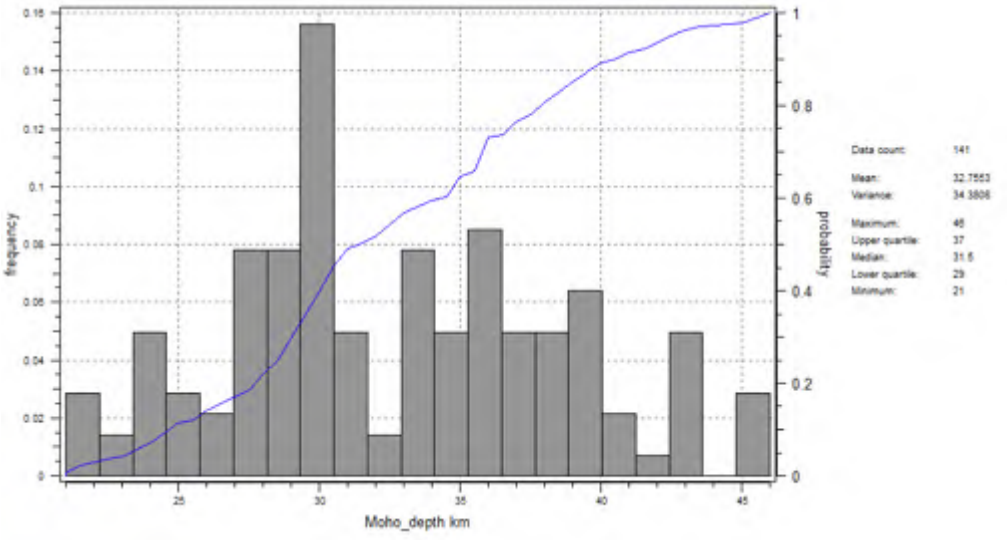

Figure A.1: Histogram for the Moho depth for the dataset used in Chapter 3

$$\begin{aligned} X_0 &= \sum(b_1 x_i) \qquad\quad linear\ drift \\ X_0 &= \sum(b_1 x_i + b_2 x_1^2) \quad quadratic\ drift \end{aligned} \tag{A.3}$$

There is an inter-relation between neighborhood size, drift, and semivariogram for the residual. We have to guess the neighborhood size. If the neighborhood is large –> smooth and gentle drift –> variable residual –> complex semivariogram; if the neighborhood is small –> more variable drift estimate –> smaller residual –> simpler semivariogram. To determine the b coefficients of the drift, it is require to solve a set of simultaneous equations, where the variables are the semivariance corresponding to different distance between the the points in the neighborhood region. After this experimantal estimation of the drift, the drift is subtracted to the regionalized variables to get the residual from which a seimavariogram is calculated. This semivariogram is compared with the that one was first assumed. If the assumptions are appropriate they will coincide, if not we have to try again. The process of attempting to simultaneous find a satisfactory representation of the semivariogram and drift expression is a major part of "structural analysis" and it require patience and experience.

Sometimes we can estimate the semivariogram in presence of drift without this trial and error procedure. It's possible to calculate the semivariogram along different direction. The semivariogram can be calculated in a direction that is drift-free. If we assume the regionalized variable is isotropic and if the drift were not present, this directional semivariogram can be used as an estimate of the drift-free semivariogram.

At this point, under the assumpiton of stationarity or not, we have found the experimental semivariogram. In principle it can be used to provide value for estimation procedure but it is discrete and we need semivariance for any distance. For

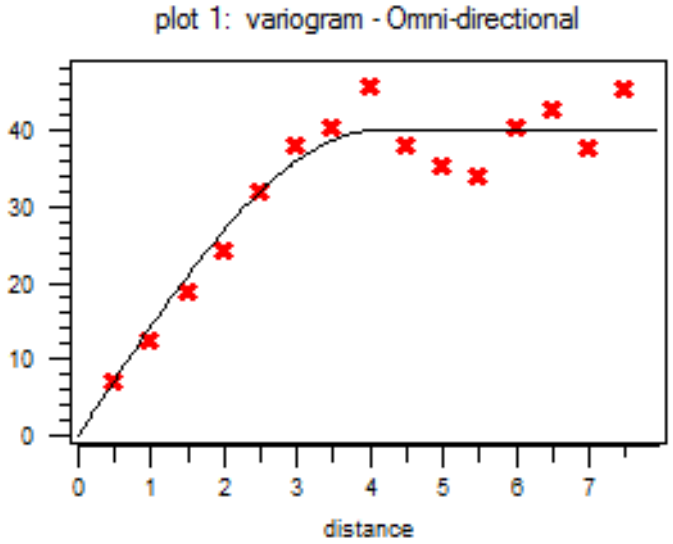

Figure A.2: Experimental semivariogram (red stars) and the modelled one (black line) for the Moho depth dataset as in Chapter 3. The distance is in geographycal degree.

this reason the experimental semivariogram should be modelled by a function. This fit step is trial-error procedure, usually done by eyes. Ideally the function choose to represent the experimental semivariogram should begin at zero, rise smoothly to an upper limit and then continue at a constant level. Usually the possible function with this properties are: spherical, exponential, gaussian, linear (two line). In some circumstance the semivariogram does not go trough zero but seem to have a some value at $h = 0$ (in theory should be zero). This is called "nugget effect". In theory this is due to the fact that regionalized variable is subject to sampling errors or is so erratic over a vary short distance.
The modelled semivariogram is the main ingredient to apply the kriging estimation procedure, as described in the next section.
In Chapter 3 we apply geostatistics to obtain reliable maps of the main properties of the crust in East Alps region. As an example we report here (Figure A.1) the distribution (Gaussian) relative to the observed Moho depth (at the observation points), the experimental semivariogram and the modelled one for the same variable. In figure A.2 is possible to identify the neighborhood region (where the semivariogram increase) and the sill region (flat part).

A.3 Kirging

Kriging is a form of generalized linear regression for the formulation of an optimal spatial estimator in a minimum mean-square-error sense (Olea, 2009) and in contrast to linear regression, it takes into account observation volume and dependence among

data. There are many form of kriging: *simple kriging, ordinary kriging, universal kriging, block kriging, indicator kriging, disjunctive kriging, multigaussian kriging, cokriging and so on.*. In Chapter 3 we decide to apply the *ordinary kriging* because of its simplicity and its reliable estimation.
In the ordinary kriging, the main assumptions are (Davis, 2002): the observations $Z(\mathbf{x}_i)$ (where i are the different locations of the sampling) are a partial realization of a random function $Z(\mathbf{x})$ for which the mean, the spatial covariance and the semivariance do not depend upon x; the mean is constant in the neighborhood but unknown (in the simple kriging the mean is zero).
If $Z(\mathbf{x}_0)$ are the locations where the regionalized variable has to be estimated, the definition of the ordinary kiging is written:

$$Z(\mathbf{x}_0) = m\Big(1 - \sum_{1=1}^{k} \lambda_i\Big) + \sum_{1=1}^{k} \lambda_i Z(\mathbf{x}_i) \tag{A.4}$$

where k is the number of the observations, m is the mean, λ_i are real weight.
The trick at the base of this procedure is to force the $\sum_{1=1}^{k} \lambda_i$ to be 1. In this way the first term of the equation became zero, leading the estimator to be independent by the mean m. The ordinary kriging estimator is (Olea, 2009):

$$Z(\mathbf{x}_0) = \begin{cases} \sum_{1=1}^{k} \lambda_i Z(\mathbf{x}_i) \\ \\ \sum_{1=1}^{k} \lambda_i = 1 \end{cases} \tag{A.5}$$

Using the Lagrange method of multipliers, it is possible to incorporate into the problem of minimizing the error variance the constrain that the sum of λ_i must be 1. This involve the introduction of a Lagrange multiplier μ into the set of equations to solve (Davis, 2002):

$$Z(\mathbf{x}_0) = \mathbf{Y}'\mathbf{\Lambda} \tag{A.6}$$

where $\mathbf{\Lambda} = \mathbf{W}^{-1}\mathbf{B}$ is the vector of the unknown weights ($\mathbf{\Lambda}' = [\lambda_1 \quad \lambda_2 \quad \dots \quad \mu]$),

$$\mathbf{W} = \begin{pmatrix} \gamma(\mathbf{x}_1, \mathbf{x}_1) & \gamma(\mathbf{x}_1, \mathbf{x}_2) & \dots & \gamma(\mathbf{x}_1, \mathbf{x}_k) \\ \vdots & \vdots & \vdots & \vdots \\ \gamma(\mathbf{x}_k, \mathbf{x}_1) & \gamma(\mathbf{x}_k, \mathbf{x}_2) & \dots & \gamma(\mathbf{x}_k, \mathbf{x}_k) \end{pmatrix} \tag{A.7}$$

and $\mathbf{B} = [\gamma(\mathbf{x}_0, \mathbf{x}_1) \quad \gamma(\mathbf{x}_0, \mathbf{x}_2) \quad \dots \quad \gamma(\mathbf{x}_0, \mathbf{x}_k)]$. $\mathbf{B}$ and $\mathbf{W}$ are derived from the semivariogram model.

A important point is that kriging provide the error variance of kriging estimation, σ_k^2, as a measure of precision, available in each point where kriging estimation is made. It is defined as:

$$\sigma^2(\mathbf{x}_0) = \mathbf{B}'\mathbf{\Lambda} \tag{A.8}$$

However this measure relies on the correctness of the modelled semivariogram (i.e. is only variogram dependent and no data-value dependent) and it is not a usual

expression of uncertainties (Yamamoto, 2000).
For the dataset used in the Chapter 3, and in particular for the Moho depth, we plot σ^2 resulted from the kriking estimation in Figure 3.4, where is possible to see that the estimation is more reliable near the observation points and degrade moving away.

References

Davis, J., 2002. Statistics and Data Analysis in Geology. John Wiley & Sons. third edition.

Olea, R.A., 2009. A practical primer on geostatistics. U.S. Geological Survey Open-File Report 2009-1103 p. 346.

Remy, N., Bouchera, A., Wu, J., 2009. Applied Geostatistics with SGeMS: A User's Guide. Cambridge University Press.

Yamamoto, J.K., 2000. An alternative measure of the reliability of ordinary kriging estimates. Math. Geology. 32, 489–509.

Appendix B

ADER-DG method for elastic waves propagation

B.1 Introduction

In this appendix we summarize the main concept and equations of the ADER-DG scheme, implemented the SeisSol code used for the simulations in Chapter 4; first, we delineate the main features of the code and than, we briefly explain the numerical scheme (more informations on *www.geophysik.uni-muenchen.de/∼kaeser/SeisSol/*).

B.2 The SeisSol simulation software

In the analysis of numerical representation of the crustal structure (Chapter 4), we propagate seismic waves in realistic 2D crustal sections with complicated geometry. The simulation of a complete 3D seismic wavefield with realistic assumptions about the material properties of the medium requires the implementation of the solution of a system of partial differential equations. For our test cases, we choose the SeisSol-2D code (Kaeser and Dumbser, 2006). The SeisSol code, developed by Dr. Martin Kaeser and his research group at LMU in Munich, is able to propagate wave produced by a various source trough complex material and domain. The code is based on the Discontinuous Galerkin scheme (DG) in combination with the Arbitrary high order DERivative (ADER) approach (Section B.3), to solve the elastic wave equation with high accuracy. This approach has some advantages with respect to other methods (such as the Spectral Element Method or the Finite Difference method): it reaches the same high accuracy in both space and time, while other methods often implement, for the time integration, at most a fourth-order-Runge-Kutta schemes. It can use unstructured meshes (both triangular/tetraedral for 2D and rectangolar/exaedral for 3D), very important issue when the computational domain presents a complicated geometrical structure.
The main remarkable characteristics of the SeisSol simulation software are:

- use of tetrahedral and hexahedral meshes to approximate complex 3D model geometries
- use of acoustic, elastic, viscoelastic, poroelastic, and anisotropic material to approximate realistic geological subsurface properties.

- use of arbitrarily high approximation order in time and space to produce reliable and sufficiently accurate synthetic seismograms or other seismological data set.

- use of explicit local time step algorithm, such that each element is running its own optimal time step length to reduce computation time.

Depending on the desired frequency range of the simulated waves and the material properties the spatial wavelengths vary a lot: high-frequency wave propagation in low-velocity material can reduce the wavelengths dramatically and the necessary resolution of the numerical mesh to discretize the physical model can lead to an enormous amount of mesh elements. Therefore, for large-scale applications the code is dependent on high-performance computing (HPC) infrastructure. Our analysed test cases (Chapter 4), can be considered a large scale 2D applications, thus we needed to perform all the simulation at LRZ (Leibniz-Rechenzentrum) computer centre in Munich and a usual simulation was 8 hours long on 510 processors.
As already mentioned, the code can run using structured and unstructured meshes. Creating a mesh is a very important point to get a realistic and likely simulation. Once the geometry of the computational domain is ready (lines in 2D and surfaces in 3D coordinates), these can be imported in one of the available mesh generator software and then the triangular mesh will be created. At this point a considerable importance has the right definition of the elements size (that should be in accordance with the characteristic of the physical domain and of the wave propagator code used) and the definition of the boundary conditions (define which is the free surface and the absorbing ones). There are many software that can be used, but we used the GAMBIT package (*www.fluent.com/software/gambit/index.htm*) or the ICEM CFD package (*www.ansys.com/products/icemcfd.asp*).
Once the mesh in $*.neu$ format is ready, it should be partitioned into n parts, where n is the number of processor used in the simulation. SeisSol code uses a free external partition software: METIS (*www.cs.umn.edu/ metis*) assisted by MATLAB scripts to obtain the right format of the resulting files. To run, SeisSol require a parameter file (**.par*) –structured in a total of 12 blocks, each of them including a different number of parameter lines depending on the type of simulation chosen– in which the characteristics of the simulation are listed: equation to solve (elastic, advection, poroelastic, anelastic, anisotropy), material file (physical properties of each triangle of the mesh), initial condition, boundary condition, source terms (point source, single force, double couple, ecc...), characteristic of the simulation (order of accuracy, fine output), output (snapshot, receivers informations).
Because of its advantages on meshing and on space and time accuracy, we choose this scheme to perform our tests concerning the representation of crustal structure in numerical methods.

B.3 Wave equation and numerical scheme

Here it is briefly describe the numerical scheme in two dimensions.
The aim is to solve the 2D wave equation in the velocity-stress formulation. In the isotropic and elastic case we have (Kaeser and Dumbser, 2006):

$$\frac{\partial u_p}{\partial t} + A_{pq}\frac{\partial u_q}{\partial x} + B_{pq}\frac{\partial u_q}{\partial y} = S_p \tag{B.1}$$

where $\mathbf{u} = (\sigma_{xx}, \sigma_{yy}, \sigma_{xy}, v, w)$ is the vector of unknown variables that are space and time dependent and $S_p = S(\mathbf{x}, t)$ is the source vector representing different physical phenomena such as forces, moment tensors, viscoelastics effects... . The matrix $A_{pq} = A_{pq}(\mathbf{x})$ and $B_{pq} = B_{pq}(\mathbf{x})$ are the Jacobian matrices that contain the media elastic properties (space dependent) that are density and Lame constants, $\lambda(\mathbf{x})$ and $\mu(\mathbf{x})$.
From a computational point of view, the domain in which eq.(B.1) will be solved, is divided into conforming triangular elements $T^{(i)}$ and the matrices A and B are suppose to be constant inside an element.
In each element, the solution of eq.(B.1) is numerically approximate by a u_h with a linear combination of a time-independent polynomial basis functions of degree N, $\Phi_l(\xi, \eta)$, defined in local (in $T^{(i)}$) coordinate system (ξ, η), and a time dependent degree of freedom $u_{pl}^{(i)}(t)$. To get a more efficient implementation of the final formula for $u_p(\mathbf{x}, t)$ (derived in the following in the xy reference system) each triangle $T^{(i)}$ is transformed in a reference triangle $T_E^{(i)}$. The physical and the local (reference) coordinate system are connected by a mapping function $(x, y) = (x(\xi, \eta), y(\xi, \eta))$. The approximate solution in each element is:

$$u_p(\mathbf{x}, t) = u_{pl}^{(i)}(t)\Phi_l(\xi, \eta) = \sum_{l=0}^{N-1} u_{pl}^{(i)}(t)\Phi_l(\xi, \eta) \tag{B.2}$$

where N is the number of the degree of freedom in each element given by the highest polynomial degree of the basis functions d via $N = (d+1)(d+2)/2$. The choice of the basis functions depends on the type of elements: triangular or quadrilateral. The numerical scheme is constructed by integrating in space and time the eq.(B.1) over elements $T^{(i)}$ using the approximations of unknown given in eq.(B.2).
Multiplying eq.(B.2) for an orthogonal basis function (of the same type used in eq.(B.2)) Φ_k and integrating over an element $T^{(i)}$, it is possible to get:

$$\int_{T^{(i)}} \Phi_k \frac{\partial u_p}{\partial t} dV + \int_{T^{(i)}} \Phi_k (A_{pq}\frac{\partial u_q}{\partial x} + B_{pq}\frac{\partial u_p}{\partial y}) dV = \int_{T^{(i)}} \Phi_k S_p dV \tag{B.3}$$

An Integration by parts leads to:

$$\int_{T^{(i)}} \Phi_k \frac{\partial u_p}{\partial t} dV + \int_{\partial T^{(i)}} \Phi_k F_p^h dS - \int_{T^{(i)}} (\frac{\partial \Phi_k}{\partial x} A_{pq} u_q + \frac{\partial \Phi_k}{\partial y} B_{pq} u_q) dV = \int_{T^{(i)}} \Phi_k S_p dV \tag{B.4}$$

where is introduced a numerical flux F_p^k in the surface integral since the solution can be discontinuous at an element boundary. Because it is supposed an isotropic case, the flux can be derived for a coordinate system aligned with the upward normal vector of an element boundary. These operation require a rotation from xy system to a vector u_q^n in a local norm edge-aligned coordinate system,

$$u_p = T_{pq} u_p^n \tag{B.5}$$

where T_{pq} is the transformation matrix.
F_p^h is is evaluated along the edge of the element and is computed from the solution di the Reimann problem considering velocity and stress data (the matrix A_{qp} with the material properties) inside the element and its neighbour. In the cartesian xy coordinates the flux across the edge with one of the neighbour is defined as follow:

$$F_p^h = \frac{1}{2}(A_{pq}^{(m)} + |A_{pq}^{(m)}|)(T_{rs})^{-1} u_{sl}^{(m)} \Phi_l^{(m)} + \frac{1}{2}(A_{pq}^{(m)} - |A_{pq}^{(m)}|)(T_{rs})^{-1} u_{sl}^{(mj)} \Phi_l^{(mj)} \tag{B.6}$$

where $u_{sl}^{(m)} \Phi_l^{(m)}$ and $u_{sl}^{(mj)} \Phi_l^{(mj)}$ are the boundary extrapolated values of the numerical solution from $T^{(m)}$ and the jth side neighbour $T^{(mj)}$: boundary values of both elements adjacent to an interface contribute to the numerical flux. Due to the rotation it is sufficient to evaluate $A_{qr}^{(m)}$ only in x-direction with the material properties given in $T^{(m)}$.
Inserting the equation (B.2) and (B.6) in (B.4) an dsplitting the boundary integral into the contribution of each edge j of the triangle, is possible to get:

$$\begin{aligned}
&\tfrac{\partial}{\partial t} u_{pl}^{(m)} \textstyle\int_{T^{(m)}} \Phi_k \Phi_l dV \\
&+ \textstyle\sum_{j=1}^{3} T_{pq}^j \tfrac{1}{2} (A_{qr}^{(m)} + |A_{qr}^{(m)}|)(T_{rs}^j)^{-1} u_{sl}^{(m)} \textstyle\int_{(\partial T^{(m)})_j} \Phi_k^{(m)} \Phi_l^{(m)} ds + \\
&+ \textstyle\sum_{j=1}^{3} T_{pq}^j \tfrac{1}{2} (A_{qr}^{(m)} - |A_{qr}^{(m)}|)(T_{rs}^j)^{-1} u_{sl}^{(m)} \textstyle\int_{(\partial T^{(m)})_j} \Phi_k^{(m)} \Phi_l^{(m)} ds + \\
&- A_{pq} u_{ql}^{(m)} \textstyle\int_{T^{(m)}} \tfrac{\partial \Phi_k}{\partial x} \Phi_l dV - B_{pq} u_{ql}^{(m)} \textstyle\int_{T^{(m)}} \tfrac{\partial \Phi_k}{\partial y} \Phi_l dV = \textstyle\int_{T^(m)} \Phi_k S_p dV
\end{aligned} \tag{B.7}$$

To obtain the main advantage of this method, a coordinate trasformation should be done: from xy , to a $\xi\eta$ reference system, to a physical triangle $T^{(m)}$ to a canonical triangle T^E. In the new coordinate system the method can be implemented more efficently since many integral can be pre-computed in advance (and not during the run).
The coordinate trasformation is define as:

$$\begin{aligned}
x &= x_1 + (x_2 - x_1)\xi + (x_3 - x_1)\eta \\
y &= y_1 + (y_2 - y_1)\xi + (y_3 - y_1)\eta.
\end{aligned} \tag{B.8}$$

In the reference system, the equation B.7 became:

$$
\begin{aligned}
&\tfrac{\partial}{\partial t} u_{pl}^{(m)} |J| \int_{T^E} \Phi_k \Phi_l d\xi d\eta \\
&+ \textstyle\sum_{j=1}^{3} T_{pq}^{j} \tfrac{1}{2} (A_{qr}^{(m)} + |A_{qr}^{(m)}|)(T_{rs}^{j})^{-1} u_{sl}^{(m)} |S_j| \int_0^1 \Phi_k^{(m)}(\chi_j) \Phi_l^{(m)}(\chi_j) d\chi_j + \\
&+ \textstyle\sum_{j=1}^{3} T_{pq}^{j} \tfrac{1}{2} (A_{qr}^{(m)} - |A_{qr}^{(m)}|)(T_{rs}^{j})^{-1} u_{sl}^{(mj)} |S_j| \int_0^1 \Phi_k^{(m)}(\chi_j) \Phi_l^{(mj)}(\chi_j) d\chi_j + \\
&- A *_{pq} u_{ql}^{(m)} |J| \int_{T^E} \tfrac{\partial \Phi_k}{\partial \xi} \Phi_l d\xi d\eta - B *_{pq} u_{ql}^{(m)} |J| \int_{T^E} \tfrac{\partial \Phi_k}{\partial \eta} \Phi_l d\xi d\eta = \\
&= |J| \int_{T^E} \Phi_k S_p d\xi d\eta
\end{aligned}
\tag{B.9}
$$

where $|J|$ is the determinant of the Jacobian matrix of the coordinate trasformation in (B.8). The variable $0 <= \chi <= 1$ is introduced to parametrize the j-th edge of the reference triangle and $|S_j|$ is the length of the edge of the physical reference system. All the integral in the left side of the equation (B.9) can be computed in advance by a computer algebra system like Maple. Equation (B.9) is called the semi-discrete DG formulationand it is not needed of global mass matrix, flux matrix and stifness matrix. The method is completely local, well suited for parallelization.

The DG semi-discrete formula has to be integrated in time using the ADER approach. The main ingredient for the ADER integration are Taylor expansion in time, solution of Reimann problem to approximate the space derivatives at interfaces, the Cauchy-Kovalewski procedure to replace time derivatives by space derivatives. The ADER time integration approach provide for the time the same accuracy as the space integration (provided by the degree of approximating polynomial). The extrapolation of the solution to a future time uses a Taylor expansion where higher order time derivative are replaced by space derivatives by a recursive use of the velocity-stress wave equation. The main ingredient for the ADER integration are Taylor expansion in time, solution of Reimann problem to approximate the space derivatives at interfaces, the Cauchy-Kovalewski procedure to replace time derivatives by space derivatives.

For a complete treatise see Kaeser and Dumbser (2006), Dumbser et al. (2007a), Kaeser et al. (2007), Puente et al. (2007), Dumbser et al. (2007b)

References

Dumbser, M., Kaeser, M., Puente, J.D.L., 2007a. Arbitrary high-order finite volume schemes for seismic wave propagation on unstructured meshes in 2D and 3D. Geophysical Journal International 171(2), 665–694.

Dumbser, M., Kaeser, M., Toro, E.F., 2007b. An arbitrary high-order discontinuous galerkin method for elastic waves on unstructured meshes, v. local time stepping and p-adaptivity. Geophysical Journal International 171(2), 695–717.

Kaeser, M., Dumbser, M., 2006. An arbitrary high-order discontinuous galerkin method for elastic waves on unstructured meshes i. the two-dimensional isotropic case with external source terms. Geophysical Journal International 166(2), 855–877.

Kaeser, M., Dumbser, M., Puente, J.D.L., Igel, H., 2007. An arbitrary high-order discontinuous galerkin method for elastic waves on unstructured meshes III. viscoelastic attenuation. Geophysical Journal International 168(1), 224–242.

Puente, J.D.L., Kaeser, M., Dumbser, M., Igel, H., 2007. An arbitrary high-order discontinuous galerkin method for elastic waves on unstructured meshesâ IV. anisotropy. Geophysical Journal International 169(3), 1210–1228.

Appendix C

Spectral Element Methods

C.1 Introduction

To propagate waves in a complex 3D structure, we need to solve the wave equation with numerical methods since there is no analytical solutions available. There are many numerical methods able to do this: finite difference methods, FD, (e.g. Igel and Weber, 1996), the ADER-DG method (Kaeser and Dumbser, 2006) -described in Appendix B-, the Psedo-Spectral Element (PSE), the Spectral Element Method, SEM, (Komatitsch and Tromp, 2002; Fichtner et al., 2009). All these methods work well in simple case but they present some linitations: ADER-DG method is very accurate but not yet ready for propagation at continental scale due to the high computational costs; FD implements the strong formulation of the wave equation that could be problematic for applying boundary conditions accurately in complex structures and are inaccurate for surface waves due to numerical dispersion; in PSE the wavefield is expanded into global polynomial basis functions and it have similar problems to FD (due to the strong formulation) so a global 3D propagation is complicated. SEM seem to be a good choice in terms of accuracy and computational cost when continental-scale seismic propagations are required. We use this method, implemented in the SPECFEM3D-Globe (Komatitsch and Tromp, 2002) to simulate seismic waves in our crustal models. This appendix gives a brief overview of the spectral element method (for more details see Komatitsch and Tromp (1999)) and, of the main characteristics of SPECFEM3D-Globe (Komatitsch and Tromp, 2002), modified for our purpose during in the validation of crustal models in the Chapter 1 and Chapter 5 .

C.2 Equation of elastodynamics and Spectral Elements Method

The aim is to solve, in a given domain Ω, the equation of elastodynamics, written here in its differential formulation:

$$\rho \partial_t^2 \mathbf{s} = \nabla \cdot \mathbf{T} + \mathbf{f} \tag{C.1}$$

where $\mathbf{s}(\mathbf{x}, t)$ is the displacement which occurs at position $\mathbf{x}$ and time t, $\rho(x)$ denotes the density distribution, $\mathbf{f}$(x,t) is the seismic source and $\mathbf{T}$ is the stress tensor, related to the displacement gradient by the Hookes law: $\mathbf{T} = \mathbf{c} : \nabla s$. $\mathbf{c}$ is the fourth-order elastic tensor which describe the elastic properties of the media

and, in the general linear case, it has 21 independent parameters, while in the isotropic case only two, the Lame parameters λ e μ (and in this case $\mathbf{c}$ became $c_{ijpq} = \lambda\delta_{ij}\delta_{pq} + \mu(\delta_{ip}\delta_{jp} + \delta_{iq}\delta_{jp})$). Associated to this equation we need to satisfy the boundary and initial condition ($\mathbf{s}(\mathbf{x}, t = 0) = 0$ and $\partial_t \mathbf{s}(\mathbf{x}, t = 0) = 0$). The boundary condition are that the traction must vanish ($\mathbf{T}\cdot\hat{\mathbf{n}} = 0$) at the free surfaces, must be continuous at internal boundaries together with displacement.

The spectral element method is based on the integral or *weak* formulation that is valid for a completely general anelastic, anisotropic model, instead of the strong one described above. The weak formulation is obtained taking the product of both side of the equation C.1 with an arbitrary vector $\mathbf{w}$ and integrating by parts over a volume Σ and imposing the boundary conditions. This his:

$$\int_\Omega \rho \mathbf{w} \partial_t^2 \mathbf{s} d^3\mathbf{r} = -\int_\Omega \nabla\mathbf{w} : \mathbf{T} d^3\mathbf{r} + \mathbf{M} : \nabla\mathbf{w}(\mathbf{r_s}) S(t) \tag{C.2}$$

since $\mathbf{f} = -\mathbf{M}\cdot\nabla\delta(\mathbf{r}-\mathbf{r_s})S(t)$, with $\mathbf{M}$ the moment tensor, $\mathbf{r_s}$ the location of the point source and $S(t)$ the source time function. The free surface condition is automatically satisfied since we integrate over a volume Ω. If a fluid-solid boundary is present, the normal component of the velocity and the traction should be continuous and the solution of equation C.2 is found separately in the two media and then coupled together by the right boundary conditions. For the crust and the mantle, equation C.2 is (Komatitsch and Tromp, 2002):

$$\int_M \rho \mathbf{w} \partial_t^2 \mathbf{s} d^3\mathbf{r} = -\int_M \nabla\mathbf{w} : \mathbf{T} d^3\mathbf{r} + \mathbf{M} : \nabla\mathbf{w}(\mathbf{r_s}) S(t) - \int_{CMB} \mathbf{w}\cdot\mathbf{T}\cdot\hat{\mathbf{n}} d^2\mathbf{r} \tag{C.3}$$

M is the mantle (and crust) and CMB is the core mantle boundary and $\hat{\mathbf{n}}$ is the outward normal vector on CMB. For To impose the continuity of the traction, $\mathbf{T}\cdot\hat{\mathbf{n}}$ should be replaced by the traction in the fluid $-p\hat{\mathbf{n}}$. In the outer core (OC) the equation to solve is:

$$\int_{OC} k^{-1} w \partial_t^2 \chi d^3\mathbf{r} = -\int_{OC} \rho^{-1} \nabla w \cdot \nabla\chi d^3\mathbf{r} + \int_{CMB} w\hat{\mathbf{n}}\cdot\mathbf{v} d^2\mathbf{r} - \int_{ICB} w\hat{\mathbf{n}}\cdot\mathbf{v} d^2\mathbf{r} \tag{C.4}$$

where k is the adiabatic bulk modulus in the fluid, $\mathbf{v}$ is the velocity, χ the scalar potential and w a scalar test function. Equation C.3, C.4 correctly represent the solid-fluid interface (Komatitsch and Tromp, 2002). In the inner core the weak formulation is:

$$\int_{IC} \rho \mathbf{w} \partial_t^2 \mathbf{s} d^3\mathbf{r} = -\int_{IC} \nabla\mathbf{w} : \mathbf{T} d^3\mathbf{r} - \int_{IMB} \mathbf{w}\cdot\mathbf{T}\cdot\hat{\mathbf{n}} d^2\mathbf{r} \tag{C.5}$$

The discretization of equations C.3, C.4 and C.5 point out the main advantages of this technique. First of all, the domain has to be discretized in several parts forming a mesh. In SEM method the mesh is composed by hexahedral non overlapping element (conforming mesh) honouring the free surface and, in the best case,

the geological discontinuities. The element dimensions should be designed on the base of the velocity structure of the medium and on the resolution of the synthetic seismograms (minimum period simulated with accuracy). In general, smaller are the element, shorter is the accurate period simulated.
Once the mesh is generated, the next step is to represent the displacement in each element. High degree Lagrange polynomials (from 4 to 10 degree) are used to represents functions inside an element that are evaluated at $n+1$ Gauss-Lobatto-Legendre control points. this choice will make the mass matrix diagonal with an improvement of computational efficiency in the solver. Because of the hesahedral are isomorphous to the cube, is possible to map the Cartesian coordinates of an element in a reference cube by a mapping function from $\mathbf{x}$ to ξ (the Jacobian of the transformation should not became zero).
The discretization of the weak formulation can be obtained expand the displacement $\mathbf{s}$ and the test function $\mathbf{w}$ in terms of Lagrange polynomials. Once the integration over an element is obtained, the the solution in each element should be integrated over all elements (assembling the system). The fact that the mass matrix is diagonal for construction, means that no costly linear system has to be solved to march the system in time. The integration over the time domain is achieved applying a fourth-order Runge-Kutta scheme.

It is well known that the accuracy of a numerical method strongly depend on the mesh and on the capability to well discretize the domain. The quantities that reflects the quality of the mesh are the number of grid point per wavelength (resolution), $N = \tau_0(v/\Delta h)_{min}$, and the stability condition, $C = \Delta t(v/\Delta h)_{max}$. τ_0 is the shorter period of the source, v is the wave speed and Δh is the grid spacing. The stability condition is important to know how large the time step of the time integration can be while a stable simulation is maintaining.

C.3 SPECFEM3D-Globe software

The SPECFEM3D-Globe is a free Fortran95 based software available at *www.geodynamics.org/cig/software/specfem3d-globe*. It use parallel programming based on MPI and runs on PC clusters. More informations regarding the technical details about running the code can be find in the available user manual. This code take into account at global or regional scale for relaistic crustal structure, anisotropic mantle model, ellipticity, topography, oceans, gravity, rotation and attenuation. SPECFEM3D-Globe has a internal mesher to discretize the whole Earth or chunks of it, or can read external mesh obtained with external mesher (such as CUBIT). This code is also able to perform adjoint simulation and to compute the sensitivity kernels (finite-frequency kernels) useful in full waveform inversions. The simulation can be done in the whole Earth or in chunks of it (regional simulation). It implements two 3D crustal models (CRUST2.0 and EuCRUST-07), some 3D velocity models (such as S20RTS, S362ANI, ...) and the 1D models such as PREM, ak135, iasp91. IIt is possible to implement our own crustal, mantle and attenua-

tion model modifying the routine *crustal_ model.f90, mantle_ model.f90* and *attenuation_ model.f90*. One should be careful to adapt some MPI variable to the new ones. The mesh is doubled in size at some discontinuities such as the crust, the 670 km, above the inner-core boundary. In this way, it's possible to reduce the total number of elements and thereby the computational costs, maintaining the desired accuracy.
All the parameters and the output of the simulation are controlled by a parameter file that should be edited before running the simulations. Once the mesh is done, the solver can run. A domain as large as 1/6 of the Earth with an accuracy on period of 12 seconds on the simulated seismograms takes 2 hours on 256 processors. In global simulations, the source is represented by a point source and it is described by the Harvard Centroid Moment Tensor (CMT).
Some tools for outputs visualization and post processing are distributed with the code. The users is able to visualize the mesh and the snapshot of the simulations using different visualization software (Paraview, opendx, GMT, Gnuplot, Google Earth), rotate and compare seismograms, make profiles of the models and so on.

References

Fichtner, A., Kennett, B.L.N., Igel, H., Bunge, H., 2009. Full seismic waveform tomography for upper-mantle structure in the australasian region using adjoint methods. Geophysical Journal International 179(3), 1703–1725.

Igel, H., Weber, M., 1996. P-sv wave propagation in the whole mantle using high-order finite differences:application to lowermost mantle structure. Geophys. Res. Lett. 23, 415Ð418.

Kaeser, M., Dumbser, M., 2006. An arbitrary high-order discontinuous galerkin method for elastic waves on unstructured meshes i. the two-dimensional isotropic case with external source terms. Geophysical Journal International 166(2), 855–877.

Komatitsch, D., Tromp, J., 1999. Introduction to the spectral-element method for 3-d seismic wave propagation. Geophys. J. Int. 139, 806– 822.

Komatitsch, D., Tromp, J., 2002. Spectral-element simulations of global seismic wave propagation: I. validation. Geophysical Journal International 149(2), 390–412.

Appendix D

Time-Frequency misfit criteria

D.1 Introduction

This appendix will briefly describe the time-frequency misfit criteria proposed by Kristekova et al. (2009) widely used in this thesis. In literature there are many possible choice as for example RMS (root mean square) or difference between two seismograms but non of them are able to characterize the nature of the difference. This criteria properly characterize the differences and improve the quantitative comparison of two signals and were already applied by Moczo et al. (2010), Pelties et al. (2010), Castro et al. (2010) and others. The Fortran package TF_MISFIT_GOF_CRITERIA is available at *http://www.nuquake.ue/Computer_Codes/*

The description reported in this appendix is mainly taken from Kristekova et al. (2006) and Kristekova et al. (2009).

D.2 TF misfit criteria

First of all, each signal has to be reported in a time frequency representation. Taking the continuous wavelet transform of a signal:

$$W(t,f) = \sqrt{\frac{2\pi|f|}{\omega_0}} \int s(t)\psi^*(s\pi f \frac{\tau - t}{\omega_0}). \tag{D.1}$$

$W(f,t)^2$ is the energy distribution in TF plane, $A(t,f) = |W(t,f)|$ is the envelope of the signal while $\Phi(t,f) = Arg[W(t,f)]$ is the phase. In this way is possible to analyse a instantaneous spectral content of a signal or a the time evolution at any frequency.

Since we are interested in misfit measurements, if we consider two signals $s(t)$ and $s_r(t)$ (r is the reference), the envelope and the phase difference between the two signal will be $\Delta A = |W(t,f)| - |W_r(t,f)|$ and $\Delta\Phi(t,f) = Arg[\frac{W(t,f)}{W_r(t,f)}]$ respectively. The phase difference is always in a range of $[-\pi, +\pi]$.

A misfit measurement is needed in different cases such as investigating smaller part of a signal, parts with different amplitude, the whole signal... The definition of this time-misfit criteria starts from the definition of a "local" criterion that would depend only on the characteristics of the envelope and the phase at a chosen point: the envelope difference will be normalize by the envelope of the reference signal at that (t,f) point while the phase has not to be normalized but, in order to get a range of [-1,1], will be normalized for π. The envelope local TF misfit criteria look like

$$TFEM_{LOC}(t,f) = \frac{\Delta A(t,f)}{A_r(t,f)} \tag{D.2}$$

and for the phase is :

$$TFPM_{LOC}(t,f) = \frac{\Delta \phi(t,f)}{\pi} \tag{D.3}$$

It is also important to have a misfit criteria that will be related to those part of the reference in which the envelope reach the largest value and require that the envelope is equal to the maximum $|\Delta A(t,f)|$ only at the point in which the reference signal has the maximum value; at the other points the misfit could be proportional to the ratio $\frac{A_R(t,f)}{max_{t,f}\{A_r(t,f)\}}$. Is it possible to define the global TF misfit as:

$$TFEM_{GLOB}(t,f) = \frac{\Delta A(t,f)}{max_{t,f}\{A_r(t,f)\}} \tag{D.4}$$

$$TFPM_{GLOB}(t,f) = \frac{A_r(t,f)}{max_{t,f}\{A_r(t,f)\}} \frac{\Delta \phi(t,f)}{\pi} \tag{D.5}$$

The globally normalized misfit will be applied when one is not interested in the misfit anatomy of that part of the signals that have a smaller amplitude compared to the maximum envelope. That's useful to quantify an overall of agreement between two signals. We applied this global FT misfit criteria in Chapter **??** and **??**. A picture of the TF representation of the global TF misfit is showed in 5.4, Chapter **??** The locally normalized should be used when little part of the signal are compared and where a detailed anatomy of the disagreement between the signals is needed.

For three component signals ($s_i(t)$ and $sr_i(t), i = 1,2,3$ number of component) it is still possible to define an analogous measure of misfit. In order to consider all the three components and the relative amplitude into account the only choice for the global misfit is to normalize with the maximum of the TF envelope from the three components. For the globally normalized envelope and phase TF misfit we have,

$$TFEM_{GLOB_i}(t,f) = \frac{\Delta A(t,f)}{max_{i;t,f}\{Ar_i(t,f)\}} \tag{D.6}$$

$$TFPM_{GLOB_i}(t,f) = \frac{A_R(t,f)}{max_{i;t,f}\{Ar_i(t,f)\}} \frac{\Delta \phi(t,f)}{\pi} \tag{D.7}$$

It is also possible to evaluate the time-dependencies of the phase and envelope misfit taking the sum over frequencies.

$$TEM_{GLOB_i}(t) = \frac{\sum_t \Delta A(t,f)}{max_{i;t}(\sum_t Ar_i(t,f))} \tag{D.8}$$

$$TPM_{GLOB_i}(t) = \frac{\sum_t A_R(t,f)}{max_{i;t}(\sum_t Ar_i(t,f))} \frac{\Delta \phi(t,f)}{\pi} \tag{D.9}$$

A summation over time of TFEM and TFPM ,instead, gives the frequency dependence of the misfit. Performing a summation over both frequency and time, will give a single misfit number for envelope and phase. This is very useful whenever it is needed a overall measure of agreement between two seismograms. The globally normalized single-value envelope and phase misfit is defined as:

$$EM_{GLOB_i}(t) = \sqrt{\frac{\sum_f \sum_t |\Delta A(t,f)|^2}{max_{i;t}(\sum_t \sum_f (Ar_i(t,f))^2)}} \tag{D.10}$$

$$PM_{GLOB_i}(t) = \sqrt{\frac{\sum_f \sum_t A_R(t,f)^2}{max_{i;t}(\sum_t \sum_f (Ar_i(t,f)^2)} \frac{\Delta\phi(t,f)}{\pi}} \tag{D.11}$$

PM and EM misfit were widely used in the comparison analysis in Chapter 4 and 5.

For a complete treatment see Kristekova et al. (2006) and Kristekova et al. (2009).

References

Castro, C.E., Kaeser, M., Brietzke, G.B., 2010. Seismic waves in heterogeneous material: subcell resolution of the discontinuous galerkin method. Geophysical Journal International 182(1), 250–264.

Kristekova, M., Kristek, J., Moczo, P., 2009. Time-frequency misfit and goodness-of-fit criteria for quantitative comparison of time signals. Geophys. J. Int. 178(2), 813–825. doi:10.1111/j.1365-246X.2009.04177.x.

Kristekova, M., Kristek, J., Moczo, P., Day, S.M., 2006. Misfit criteria for quantitative comparison of seismograms. Bull. Seis. Soc. Am. 96(5), 1836–1850. doi:10.1785/0120060012.

Moczo, P., Kristek, J., Galis, M., Pazak, P., 2010. On accuracy of the finite-difference and finite-element schemes with respect to p-wave to s-wave speed ratio. Geophysical Journal International 182(1), 493–510.

Pelties, C., Kaeser, M., Hermann, V., Castro, C.E., 2010. Regular versus irregular meshing for complicated models and their effect on synthetic seismograms. Geophysical Journal International 183(2), 1031–1051.